

**NPS ARCHIVE**

**1999.09**

**SALINAS, A.**



DUDLEY KNOX LIBRARY  
NAVAL POSTGRADUATE SCHOOL  
MONTEREY CA 93943-5101





# NAVAL POSTGRADUATE SCHOOL

## Monterey, California



## THESIS

SPRAY GENERATION

by

Angel G. Salinas

September 1999

Thesis Advisor:

T. Sarpkaya

Approved for public release; distribution is unlimited.



# REPORT DOCUMENTATION PAGE

Form Approved  
OMB No. 0704-0188

Public reporting burden for this collection of information is estimated to average 1 hour per response, including the time for reviewing instruction, searching existing data sources, gathering and maintaining the data needed, and completing and reviewing the collection of information. Send comments regarding this burden estimate or any other aspect of this collection of information, including suggestions for reducing this burden, to Washington headquarters Services, Directorate for Information Operations and Reports, 1215 Jefferson Davis Highway, Suite 1204, Arlington, VA 22202-4302, and to the Office of Management and Budget, Paperwork Reduction Project (0704-0188) Washington DC 20503.

1. AGENCY USE ONLY (Leave blank)		2. REPORT DATE September 1999	3. REPORT TYPE AND DATES COVERED Master's Thesis
4. TITLE AND SUBTITLE SPRAY GENERATION			5. FUNDING NUMBERS
6. AUTHOR(S) Salinas, Angel G.			
7. PERFORMING ORGANIZATION NAME(S) AND ADDRESS(ES) Naval Postgraduate School Monterey, CA 93943-5000			8. PERFORMING ORGANIZATION REPORT NUMBER
9. SPONSORING / MONITORING AGENCY NAME(S) AND ADDRESS(ES)			10. SPONSORING / MONITORING AGENCY REPORT NUMBER
11. SUPPLEMENTARY NOTES The views expressed in this thesis are those of the author and do not reflect the official policy or position of the Department of Defense or the U.S. Government.			
12a. DISTRIBUTION / AVAILABILITY STATEMENT Approved for public release; distribution is unlimited.			12b. DISTRIBUTION CODE
13. ABSTRACT (maximum 200 words)  This is an experimental investigation of the ligaments and drops generated at the free surface of liquid wall jets and liquid axisymmetric jets flowing over sand and polystyrene (beads) roughed surfaces. Experiments were conducted with freshwater and Eulerian and Lagrangian methods of description were used in the analysis. Measurements were made with three different high-speed imagers and two different pulsating laser systems and analyzed with appropriate image analysis software. The liquid jet Reynolds number ranged from $3.5 \times 10^4$ to $8.5 \times 10^4$ , the Froude number from 8 to 30, and the Weber number from 2,000 to 7,500. The vertical positions, velocities and accelerations of several ligaments from inception to drop formation as well as the characteristics of the droplets were determined from the digitized images. These are expected to lead to a better understanding of the formation and the ejection of the eddies from the turbulent jet beneath the free surface.			
14. SUBJECT TERMS Spray, Drops, Jets, Bow sheets, Liquid sheets, Turbulent Layers, ligament positions, ligament velocities, and ligament accelerations			15. NUMBER OF PAGES 100
			16. PRICE CODE
17. SECURITY CLASSIFICATION OF REPORT Unclassified	18. SECURITY CLASSIFICATION OF THIS PAGE Unclassified	19. SECURITY CLASSIFICATION OF ABSTRACT Unclassified	20. LIMITATION OF ABSTRACT UL

THIS PAGE LEFT INTENTIONALLY BLANK



Approved for public release; distribution is unlimited

## SPRAY GENERATION

Angel G. Salinas  
Lieutenant, United States Navy  
B.S., Purdue University, 1992

Submitted in partial fulfillment of the  
requirements for the degree of

MASTER OF SCIENCE IN MECHANICAL ENGINEERING

from the

NAVAL POSTGRADUATE SCHOOL  
September 1999



## ABSTRACT

This is an experimental investigation of the ligaments and drops generated at the free surface of liquid wall jets and liquid axisymmetric jets flowing over sand and polystyrene (beads) roughed surfaces. Experiments were conducted with freshwater and Eulerian and Lagrangian methods of description were used in the analysis. Measurements were made with three different high-speed imagers and two different pulsating laser systems and analyzed with appropriate image analysis software. The liquid jet Reynolds number ranged from  $3.5 \times 10^4$  to  $8.5 \times 10^4$ , the Froude number from 8 to 30, and the Weber number from 2,000 to 7,500. The vertical positions, velocities and accelerations of several ligaments from inception to drop formation as well as the characteristics of the droplets were determined from the digitized images. These are expected to lead to a better understanding of the formation and the ejection of the eddies from the turbulent jet beneath the free surface.



THIS PAGE LEFT INTENTIONALLY BLANK

## TABLE OF CONTENTS

I.	INTRODUCTION.....	1
II.	APPARATUS AND PROCEDURES.....	5
III.	DISCUSSION OF RESULTS.....	9
IV.	CONCLUSIONS.....	15
	APPENDIX. FIGURES .....	17
	LIST OF REFERENCES .....	77
	INITIAL DISTRIBUTION LIST.....	79

THIS PAGE LEFT INTENTIONALLY BLANK



## LIST OF FIGURES

1.	CAD drawing of the rectangular liquid wall jet nozzle .....	17
2.	Photograph of the rectangular liquid wall jet nozzle.....	18
3.	Equipment arrangement for the rectangular liquid wall jet experiments, with fluid flow path indicated by the arrows.....	19
4.	Photograph of the outside of the rectangular nozzle with the cylindrical gate open .....	20
5.	a. Diagram of liquid wall jet	
	b. Coordinate system used for Lagrangian method of description.....	21
6.	Photograph of the parallel railing system used for Lagrangian method of description .....	22
7.	CAD drawing of the axisymmetric nozzle.....	23
8.	Side view of the axisymmetric nozzle with test rod assembly installed .....	24
9.	Distribution of normalized filament length for bead roughness for wall jet thickness = 14 mm ( $k/h_o = 0.06$ , $Fr = 16.6$ , $We = 7367$ ) .....	25
10.	Distribution of normalized filament length for sand roughness for wall jet thickness = 14 mm ( $k/h_o = 0.06$ , $Fr = 16.6$ , $We = 7367$ ).....	25
11.	Comparison of the distributions of normalized filament length for two types of roughness, beads and sand.....	26
12.	Distribution of normalized filament diameter for bead roughness for wall jet thickness = 14 mm ( $k/h_o = 0.06$ , $Fr = 16.6$ , $We = 7367$ ).....	27
13.	Distribution of normalized filament diameter for sand roughness for wall jet thickness = 14 mm ( $k/h_o = 0.06$ , $Fr = 16.6$ , $We = 7367$ ).....	27
14.	Comparison of the distributions of normalized filament diameter for two types of roughness, beads and sand.....	28
15.	Distribution of normalized drop diameter for bead roughness for wall jet thickness = 14 mm ( $k/h_o = 0.06$ , $Fr = 16.6$ , $We = 7367$ ).....	29
16.	Distribution of normalized drop diameter for sand roughness for wall jet thickness = 14 mm ( $k/h_o = 0.06$ , $Fr = 16.6$ , $We = 7367$ ).....	29

17.	Comparison of the distributions of normalized drop diameter for two types of roughness, beads and sand .....	30
18.	Distribution of normalized filament length for the liquid wall jet with jet thickness = 14 mm ( $k/h_o = 0.06$ , $Fr = 25.8$ , $We = 7367$ ) .....	31
19.	Distribution of normalized filament length for the liquid wall jet with jet thickness = 5.8 mm ( $k/h_o = 0.06$ , $Fr = 25.8$ , $We = 3014$ ) .....	31
20.	Comparison of the distributions of normalized filament length for the liquid wall jet for two jet thickness .....	32
21.	Distribution of normalized filament diameter for the liquid wall jet with jet thickness = 14 mm ( $k/h_o = 0.06$ , $Fr = 16.6$ , $We = 7367$ ) .....	33
22.	Distribution of normalized filament diameter for the liquid wall jet with jet thickness = 5.8 mm ( $k/h_o = 0.06$ , $Fr = 25.8$ , $We = 3014$ ) .....	33
23.	Comparison of the distributions of normalized filament diameter for the liquid wall jet for two jet thickness .....	34
24.	Distribution of normalized drop diameter for the liquid wall jet with jet thickness = 14 mm ( $k/h_o = 0.06$ , $Fr = 16.6$ , $We = 7367$ ) .....	35
25.	Distribution of normalized drop diameter for the liquid wall jet with jet thickness = 5.8 mm ( $k/h_o = 0.06$ , $Fr = 25.8$ , $We = 3014$ ) .....	35
26.	Comparison of the distributions of normalized drop diameter for the liquid wall jet for two thickness .....	36
27.	Distribution of normalized filament length for the axisymmetric jet with roughness ( $k/h_o = 0.02$ ( $h_o = 7.9\text{mm}$ , $Fr = 25.8$ , $We = 3014$ ) .....	37
28.	Distribution of normalized filament length for the liquid wall jet with roughness ( $k/h_o = 0.02$ ( $h_o = 5.8\text{mm}$ , $Fr = 26.5$ , $We = 2858$ ) .....	37
29.	Comparison of the distributions of normalized filament length for the axisymmetric and wall jet for the same relative roughness, $k/h_o = 0.02$ .....	38
30.	Distribution of normalized filament diameter for the axisymmetric jet with roughness ( $k/h_o = 0.02$ ( $h_o = 7.9\text{ mm}$ , $Fr = 25.8$ , $We = 3014$ ) .....	39
31.	Distribution of normalized filament diameter for the liquid wall jet with roughness ( $k/h_o = 0.02$ ( $h_o = 5.8\text{ mm}$ , $Fr = 26.5$ , $We = 2858$ ) .....	39
32.	Comparison of the distributions of normalized filament diameter for the axisymmetric and wall jet for the same relative roughness, $k/h_o = 0.02$ .....	40

33.	Distribution of normalized drop diameter for the axisymmetric jet with roughness ( $k/h_o = 0.02$ ( $h_o = 7.9$ mm, $Fr = 25.8$ , $We = 3014$ )).....	41
34.	Distribution of normalized drop diameter for the liquid wall jet with roughness ( $k/h_o = 0.02$ ( $h_o = 5.8$ mm, $Fr = 26.5$ , $We = 2858$ )).....	41
35.	Comparison of the distributions of normalized drop diameter for the axisymmetric and wall jet for the same relative roughness, $k/h_o = 0.02$ .....	42
36.	Distribution of normalized filament length for the liquid wall jet with roughness ( $k/h_o = 0.06$ ( $h_o = 5.8$ mm, $Fr = 25.8$ , $We = 3014$ )).....	43
37.	Distribution of normalized filament length for the axisymmetric jet with roughness ( $k/h_o = 0.02$ ( $h_o = 7.9$ mm, $Fr = 25.8$ , $We = 3014$ )).....	43
38.	Comparison of the distributions of normalized filament length for the axisymmetric and wall jet for two relative roughness.....	44
39.	Distribution of normalized filament diameter for the liquid wall jet with roughness ( $k/h_o = 0.06$ ( $h_o = 5.8$ mm, $Fr = 25.8$ , $We = 3014$ )) .....	45
40.	Distribution of normalized filament diameter for the axisymmetric jet with roughness ( $k/h_o = 0.02$ ( $h_o = 7.9$ mm, $Fr = 25.8$ , $We = 3014$ )).....	45
41.	Comparison of the distributions of normalized filament diameter for the axisymmetric and wall jet for two relative roughness.....	46
42.	Distribution of normalized drop diameter for the liquid wall jet with roughness ( $k/h_o = 0.06$ ( $h_o = 5.8$ mm, $Fr = 25.8$ , $We = 3014$ )) .....	47
43.	Distribution of normalized drop diameter for the axisymmetric jet with roughness ( $k/h_o = 0.02$ ( $h_o = 7.9$ mm, $Fr = 25.8$ , $We = 3014$ )).....	47
44.	Comparison of the distributions of normalized drop diameter for the axisymmetric and wall jet for two relative roughness.....	48
45.	Distribution of normalized filament length for liquid wall jet with jet thickness = 5.8 mm ( $k/h_o = 0.06$ , $Fr = 25.8$ , $We = 3014$ )).....	49
46.	Distribution of normalized filament length for axisymmetric jet with jet thickness = 7.9 mm ( $k/h_o = 0.06$ , $Fr = 25.8$ , $We = 3014$ )).....	49
47.	Distribution of normalized filament length for liquid wall jet with jet thickness = 14 mm ( $k/h_o = 0.06$ , $Fr = 16.6$ , $We = 7367$ )).....	50
48.	Comparison of the distributions of normalized filament length for liquid jets for three jet thicknesses .....	50



49.	Distribution of normalized filament diameter for liquid wall jet with jet thickness = 5.8 mm ( $k/h_o = 0.06$ , $Fr = 25.8$ , $We = 3014$ ).....	51
50.	Distribution of normalized filament diameter for axisymmetric jet with jet thickness = 7.9 mm ( $k/h_o = 0.06$ , $Fr = 25.8$ , $We = 3014$ ).....	51
51.	Distribution of normalized filament diameter liquid wall jet with jet thickness = 14 mm ( $k/h_o = 0.06$ , $Fr = 16.6$ , $We = 7367$ ).....	52
52.	Comparison of the distributions of normalized filament diameter for liquid jets for three jet thicknesses .....	52
53.	Distribution of normalized drop diameter for liquid wall jet with jet thickness = 5.8 mm ( $k/h_o = 0.06$ , $Fr = 25.8$ , $We = 3014$ ).....	53
54.	Distribution of normalized drop diameter for axisymmetric jet with jet thickness = 7.9 mm ( $k/h_o = 0.06$ , $Fr = 25.8$ , $We = 3014$ ).....	53
55.	Distribution of normalized drop diameter liquid wall jet with jet thickness = 14 mm ( $k/h_o = 0.06$ , $Fr = 16.6$ , $We = 7367$ ).....	54
56.	Comparison of the distributions of normalized drop diameter for liquid jets for three jet thicknesses .....	54
57.	Distribution of normalized filament length for liquid wall jet with medium roughness sand and $Fr = 16.6$ ( $k/h_o = 0.06$ , $We = 7367$ ).....	55
58.	Distribution of normalized filament length for liquid wall jet with medium roughness beads and $Fr = 16.6$ ( $k/h_o = 0.06$ , $We = 7367$ ) .....	55
59.	Distribution of normalized filament length for liquid wall jet with medium roughness sand and $Fr = 25.8$ ( $k/h_o = 0.06$ , $We = 3014$ ).....	56
60.	Comparison of the distributions of normalized filament length for liquid wall jets with medium roughness for three Froude numbers .....	56
61.	Distribution of normalized filament diameter for liquid wall jet with medium roughness sand and $Fr = 16.6$ ( $k/h_o = 0.06$ , $We = 7367$ ).....	57
62.	Distribution of normalized filament diameter for liquid wall jet with medium roughness beads and $Fr = 16.6$ ( $k/h_o = 0.06$ , $We = 3014$ ).....	57
63.	Distribution of normalized filament diameter liquid wall jet with medium roughness sand and $Fr = 25.8$ ( $k/h_o = 0.06$ , $We = 3014$ ).....	58
64.	Comparison of the distributions of normalized filament diameter for liquid wall jets with medium roughness for three Froude numbers .....	58

65.	Distribution of normalized drop diameter for liquid wall jet with medium roughness sand and $Fr = 16.6$ ( $k/\rho u_0 = 0.06$ , $We = 7367$ ) .....	59
66.	Distribution of normalized drop diameter for liquid wall jet with medium roughness beads and $Fr = 16.6$ ( $k/\rho u_0 = 0.06$ , $We = 3014$ ) .....	59
67.	Distribution of normalized filament length for liquid wall jet with medium roughness sand and $Fr = 25.8$ ( $k/\rho u_0 = 0.06$ , $We = 3014$ ) .....	60
68.	Comparison of the distributions of normalized drop diameter for liquid wall jets with medium roughness for three Froude numbers .....	60
69.	Sequence of images, captured for filament analysis (Case 1), where the ligament is born directly behind another developing ligament, makes an attempt to separate into two, and is nearly normal to the free surface .....	61
70.	a. Y-component of position of the filament tip and centroid as a function of time. ....	62
	b. Normalized y-component of position of the filament tip and centroid as a function of normalized time .....	62
71.	Sequence of images, captured for filament analysis (Case 2), where the ligament is born nearly normal to the free surface, and does not undergo necking within the observation period .....	63
72.	a. Y-component of position of the filament tip and centroid as a function of time .....	64
	b. Normalized y-component of position of the filament tip and centroid as a function of normalized time .....	64
73.	Sequence of images, captured for the filament analysis (Case 3), where the ligament is born amidst a "forest" of ligaments, leans backwards, and starts to neck but not sufficiently to produce a droplet .....	65
74.	a. Y-component of position of the filament tip and centroid as a function of time .....	66
	b. Normalized y-component of position of the filament tip and centroid as a function of normalized time .....	66
75.	Sequence of images, capture for filament analysis (Case 4), where a ligament is born, immediately produces a drop, continues to grow, and starts to neck.....	67

76.	a.	Y-component of position of the filament tip and centroid as a function of time .....	68
	b.	Normalized y-component of position of the filament tip and centroid as a function of normalized time .....	68
77.		Sequence of images, captured for filament analysis (Case 5), where a ligament is born, leans forward, necks and produces a droplet.....	69
78.	a.	Y-component of position of the filament tip and centroid as a function of time .....	70
	b.	Normalized y-component of position of the filament tip and centroid as a function of normalized time .....	70
79.		Sequence of images, captured for filament analysis (Case 6), where a ligament is born, leans backward, necks, and produces a droplet.....	71
80.	a.	Y-component of position of the filament tip and centroid as a function if time .....	72
	b.	Normalized y-component of position of the filament tip and centroid as function of normalized time.....	72
81.		Sequence of images, captured for filament analysis (Case 7), where a ligament has developed, leans backwards, starts to neck at various regions, and retracts .....	73
82.	a.	Y-component of position of the filament tip and centroid as a function of time .....	74
	b.	Normalized y-component of position of the filament tip and centroid as a function of normalized time .....	74
83.		Sequence of images, captured for filament analysis (Case 8), where a ligament is born in between two other ligaments, necks and produces a droplet. ....	75
84.	a.	Y-component of position of the filament tip and centroid as a function if time .....	76
	b.	Normalized y-component of position of the filament tip and centroid as a function of normalized time .....	76



## LIST OF TABLES

1.	Plate Roughness Levels.....	5
2.	Summary of The Liquid Jet Parameters for an Eulerian Method of Description .....	6
3.	Description of Imagers .....	8
4.	Summary of Cases for Analysis for an Eulerian Method of Description.....	10

THIS PAGE LEFT INTENTIONALLY BLANK

## LIST OF SYMBOLS

$A_f$	filament area
$D_{dr}$	drop diameter
$D_f$	effective filament diameter, $A_f/L_f$
$Fr$	jet Froude number, $U/(gh_o)^{1/2}$
$g$	gravity
$h_o$	mean jet thickness at leading edge of plate
$k$	mean roughness height
$L_f$	filament length
PIV	particale image velocimetry
$Re_h$	jet Reynolds number, $U_h o/\nu$
$Re_x$	Reynolds number based on streamwise location, $U_x/\nu$ or $U_{sx}/\nu$
$u$	instantaneous streamwise velocity component
$U_o$	mean jet velocity, $C_d \sqrt{2g\ell}$
$v$	instantaneous vertical velocity component
$We$	jet Weber number, $\rho U^2 h_o/\sigma$
$x$	streamwise axis
$x_L$	streamwise distance from leading edge of the plate to observation window
$y$	vertical axis
YAG	Yttrium-aluminum-garnet laser used in the TSI DPIV system
$\nu$	kinematic viscosity of fluid
$\mu$	dynamic viscosity of fluid
$\rho$	density of fluid
$\sigma$	surface tension of fluid

THIS PAGE LEFT INTENTIONALLY BLANK

## ACKNOWLEDGEMENTS

Every time one reaches a milestone in life one has to reflect and thank the people who have provided the support and guidance along the way, but to do so would require an entire appendix.

First, it was an honor to have had the opportunity to work with Distinguished Professor Sarpkaya. I am eternally thankful for his guidance and patience in teaching me "how to fish". His devotion and commitment to research is very contagious.

My sincere thanks to the fine men of the machine shop and to the sole man in the electronics shop. Time after time and much to my surprise, they were able to work miracles with the experimental facility.

I thank my wife, Brenda, who sacrificed countless hours which otherwise would have been spent together, so that I might realize my hopes and dreams; and Jessica who helped me never forget the things that are important in life.



THIS PAGE LEFT INTENTIONALLY BLANK

## I. INTRODUCTION

The understanding of how a thin, unbounded or wall-bounded, liquid jet becomes a multi-phase flow is of great importance in many disciplines: agriculture, ink-jet printing, spillway hydraulics, chemical warfare and food processing, to name a few. However, for this study, the motivation is to gain a better understanding of the physics behind the spray created by the bow of a ship moving through the water. The bow forms bow sheets (or spray roots) along the hull that produce spray at their free surfaces, and may also detach from the hull forming thin liquid sheets which then disintegrate into spray. The consequence of this process is that much of this water spray is deposited on the superstructure of the ship, resulting in treacherous topside footing and reduced equipment operability or damage. In more severe cases, when accompanied by subfreezing temperatures, it can lead to a reduction in ship stability as the frozen spray builds up on the superstructure, raising the ship's center of gravity and, reducing its righting moment which may limit the ship's ability to successfully carry out its designated mission.

Spray is the cause of several major problems for a ship. The most important ones are the icing around the forward perimeter of the hull, reduced equipment operability or damage, and the enhancement of ship's radar cross-section. The motivation for the present investigation is to understand the physics of the spray created by the bow of a ship as it moves through and/or slams into the oncoming waves. Aside from marine applications, there are many other practical applications for understanding how a continuum becomes a multi-phase flow via a drop formation process: agriculture, spillway hydraulics, chemical warfare and food processing, just to name a few.

The drop formation in a circular liquid jet has attracted the most mathematical and experimental interest for obvious reasons. The sprays generated from spray roots and their rupture into smaller particles have been of major practical interest in the field of combustion. There are many other applications where a continuum becomes a two- or multi-phase flow through drop dynamics (agriculture, naval architecture, irrigation, decorative fountains, ship-plunging, ink-jet printing, perfumery, deuterium microspheres

and laser fusion, chemical warfare, just to name a few). The impetus for the present research comes from the need to understand the physics of spray formation at the free surface of turbulent free jets and wall jets and, subsequently, the breakup of bow sheets into fine spray.

The investigation of wall-bounded jets raises a large number of fundamental questions some of which are common to all spray phenomena: How important is the nozzle shape (two dimensional or axisymmetric) on the subsequent evolution of the jet? If turbulence is ultimately responsible for the ejection of the lumps of fluid from the jet body, then what is responsible for the turbulence in a wall-jet with free surface? How is the free-surface/turbulence interaction modified by these ejections? How does the shape of the free surface (curvature, shear) affect the mass, momentum, and vorticity flux across the free surface? What role does the condition of the wall surface play in the ejection-sweep cycle or in the relative magnitudes of the components of the stress tensor? Does roughness enhance the mass, momentum, and vorticity flux towards and out of the free surface? Clearly, this is a very complex two-phase flow problem, requiring the understanding of the internal as well as the surface flow, even for a wall-bounded and relatively well-defined jet geometry.

Partial answers to some of the foregoing questions have been provided by several investigators listed in the references. They have shown that the qualitative features of flows over spillways, plunge pools, open water waves, and axisymmetric rods are quite similar. Their observations and measurements have also suggested that turbulence generated on the wall propagates across the flow and reaches the interface and roughens the free surface. This laminar-turbulent transition at the air/water interface is followed by a region of turbulent breakup where a forest of ligaments rise above the free surface. Some, but not all, of these ligaments give rise to one or more droplets. Subsequently, the free-surface activity gradually subsides due to loss of momentum. However, the question of how turbulence selectively accelerates and ejects parcels of fluid across the liquid/air interface remains unclear. Equally unclear is the profound effect of roughness in ligament generation and of the air bubbles created within the jet by the entrainment of air carried by the ligaments and droplets falling back on the free surface. One rather obvious

reason for this is the lack of detailed velocity and turbulence measurements in free wall jets.

A critical review of the extensive literature has shown that [Merrill (1998), and the references cited therein] the breakup of jets and sheets depends strongly not only on the conditions governing their creation; but also on the conditions surrounding their subsequent evolution under the influence of several competing internal/external influences. Some of these influences include turbulence, gravity, surface tension, liquid-sheet geometry, surface shear, roughness of the contact surface(s), velocity distribution in the sheet, temperature distribution in the jet, pressure fluctuations within and outside the liquid sheet, acoustic excitation, external flows (e.g., wind), intentionally imposed disturbances, and foreign particles (e.g., air, dust). It is generally agreed that eddies accelerated by the internal motion of the fluid tear into irregular shapes and give rise to ligaments (threads) and droplets. The ligaments may initially appear as large undefined volumes of water or nearly transparent sheets. These shapes then continue to rupture into smaller particles until the surface tension forces inhibit them from further disintegration under the prevailing environmental conditions.

The investigation described herein deals with the filament and drop formation over surfaces of various roughness (flat plates and a circular rod). Additional experiments were undertaken for a detailed observation of the free surface through the use of a PIV camera and a YAG laser. However, the failure of the PIV camera half way through the experiments has postponed this part of the research to a later date. Finally, one experiment has been carried with a 10 ppm (by weight) Polyox solution because of time limitations. This is not discussed here pending a more detailed study of the effect of various other concentrations on the filament and drop formation.

No attempt has been made to develop empirical relations between particular characteristics of the flow and the Weber number, Reynolds number, Froude number, and the relative roughness.

THIS PAGE LEFT INTENTIONALLY BLANK



## II. APPARATUS AND PROCEDURES

The experimental system used in this investigation was designed in 1995 and was already in place when the current continuing work started. Here only the most salient features and additional equipment are briefly described. Additional details of the apparatus may be found in Dr. Craig Merrill's (1998) dissertation. The existing system consisted of a two-dimensional nozzle (Fig. 1), attached to a large U-shaped water tunnel (Figs. 2-4). The jet exited from the nozzle upon the removal of a cylindrical gate and flowed, after a short free flight (about 80 mm), over the horizontal test plate.

The discharge was collected in a trough and then pumped back into the *opposite tower* of the U-shaped tunnel. With this arrangement, it was easy to maintain constant jet velocities from 3.3 m/s to 6.5 m/s *indefinitely*. Suffice it to note that the use of a nearly ideal nozzle, long observation and measurement times, and reliance on high-speed video (HSV) and laser-induced fluorescence (LIF) made the entire apparatus particularly unique for the investigation under consideration. The additional advantages of the system were the relative ease with which the roughened plates can be interchanged, bodies of special interest can be mounted, and the flow can be illuminated and photographed.

The basic test plate was a 33-cm wide and 120 to 180 cm long smooth Plexiglas sheet, mounted horizontally and rigidly on adjustable supports. The upstream edge of each plate was beveled with a sharp edge at an angle of 30 degrees from the horizontal (Figs. 5a and 5b). Some plates were sand-roughened carefully to achieve the desired relative mean roughness height of  $k/h_0$  (from 0.016 to 0.12). A complete list of the parameters encountered in the course of the investigation is given in Tables 1-2.

Roughness Description	Minimum element size (mm)	Maximum element size (mm)	Mean element size (mm)
Fine	0.104	0.147	0.13
Medium	0.300	0.355	0.33
Medium	0.710	0.970	0.84
Coarse	1.40	2.00	1.70

Table 1. Plate Roughness Levels.

Case	Description of Roughness	k (mm)	h <sub>o</sub> (mm)	U <sub>o</sub> (m/s)	$\frac{k}{h_o}$	Re <sub>x</sub> × 10 <sup>-6</sup>	Re <sub>h</sub> × 10 <sup>-4</sup>	Fr	We	Wall
A	Fine (sand)	0.13	7.9	6.2	0.02	3.1	4.9	25.8	3014	Rod
B	Fine (sand)	0.13	5.8	6.2	0.02	2.3	3.4	26.5	2858	Plate
C	Medium (sand)	0.33	5.8	6.2	0.06	3.9	3.6	25.8	3014	Plate
D	Medium (beads)	0.84	14	6.2	0.06	4.3	8.5	16.6	7367	Plate
E	Medium (sand)	0.84	14	6.2	0.06	4.7	8.5	16.6	7367	Plate
F	Coarse (sand)	1.7	14	3.3	0.12	2.5	4.5	8.9	2090	Plate

Table 2. Summary of the Liquid Jet Parameters for the Eulerian Method of Description.

The roughness elements shown in Table 1 were applied to the smooth plate by coating it first with a fast-drying epoxy and then carefully sprinkling on it the sand of desired size which was already sieved a number of times. The result was an evenly coated rough surface.

The experiments were conducted using three sizes of roughness height and two types of materials (sand and polystyrene beads). The location at which the data were analyzed is measured from the leading edge of the plate. For each experiment, data were recorded in the range of 20 to 35 inches from the leading edge. This range is referred to hereafter as the “observation window”. This is primarily because of the fact that most important free-surface activities take place within this window, as shown by previous investigations by Merrill (1998) and Vaidyanathan (1999).

It became clear during the course of the data evaluation that it would be desirable to follow a given ligament. This then enabled one to obtain sharper images and to trace the evolutionary history of the filament. It is for this purpose that a parallel railing system was constructed and a camera was mounted on the carriage (Fig. 6). The carriage was accelerated to a nearly constant speed through the use of a suitable number of weights and a pulley system. When the system was ready for a new test, a switch was actuated to release the load and thereby to move the camera at desired speeds. This mechanism has provided as many as 100 frames, separated by one milli-second intervals. Thus, it was possible to obtain displacement, velocity, and acceleration information from a selected number of images, as will be discussed later.

In addition to the two-dimensional nozzle system, an axisymmetric jet facility was constructed to overcome some of the experimental and visualization limitations experienced with the rectangular jet. The nozzle (Figs. 7 and 8) is mounted in the horizontal section of the U-tunnel. The entrance region is streamlined using a half-toroidal shape that mounts against the wall of the tank and possesses an inner diameter identical to that of the nozzle exit. The overall contraction ratio is 17.6 and the discharge coefficient of the system was experimentally determined to be 0.77.

It is envisioned that a variety of shapes such as cones, rods or wedges could be placed at the outlet of the nozzle, but for this work, only a rod was used. The significance of this arrangement is that there is no stagnation point where the flow encounters the rod. Thus, no undesirable spray or other disturbances are produced; and, it provides a clearer visual presentation of the events.

The instrumentation consisted of several high-speed cameras with frame rates from 250 frm/s to 10,000 frm/s (with shutter speeds from 1/250 to 1/5000 sec). A list of these coupled capacitive discharge (CCD) imagers (also referred to as cameras) are shown in Table 3.

Imager	Speed (frames/sec)	Recording Time	Shutter Speed (sec)	Recording Media
NAC HSV-500	250 or 500	14 min	1/250 - 1/10,000	SVHS Tape
Redlake HR 2000	50 - 8,000	4 - 8 sec	1/50 - 1/40,000	Camera RAM
Kodak MegaPlus	30	30 min	-	Digital (1008x1016)

Table 3. Description of Imagers.

The recordings of the jet surface, ligaments, droplets, and the scales inscribed on the plate were made along a centrally located strip. This assured that a single ligament or a droplet could be tracked during its lifetime.

The video images were first carefully reviewed to identify a number of representative ligaments (with or without droplets) whose motion could be traced with little or no ambiguity through the use of suitable image analysis software (Optimus-MA). It is of some importance to note that the characteristic diameter of a ligament was evaluated by drawing a contour around the ligament and automatically evaluating the enclosed area above the free surface and, therefrom, the characteristic diameter and volume.

### III. DISCUSSION OF RESULTS

The presentation and discussion of results will be conducted in two parts. The first part will deal with the comparison of filament length, filament diameter and drop diameter between various cases for various values of parameter  $k/h_0$ ,  $Fr$ , and  $We$ . In doing so, the objectives will be to establish the roles played by the fundamental governing parameters on the rise and fall of the filaments in order to understand the fluid mechanical event which give rise to the free surface structures in the form of filaments, droplets and other indescribable forms. In the second part, we will take even a closer look at the characteristics of a selected number of filaments and present their positions (mass center and tip), velocities and accelerations in order to understand the ejection of the eddies that become filaments and droplets.

Returning to the discussion of the geometric characteristics of the filaments, histograms will be used to compare two or more cases at a given time for as many as six different cases as shown in Table 4.

Case No. 1: Figures 9 and 10 show respectively, the histograms of relative filament length ( $L_f/h_0$ ) for  $k/h_0 = 0.06$ ,  $Fr = 16.6$ ,  $We = 7367$ . The only difference between the two figures is that, Fig. 9, is for a surface roughness comprised of perfectly spherical polystyrene beads and Fig. 10 is for sieved sand. It is apparent that both types of roughness produce filament lengths as large as 1.3 ( $L_f/h_0 = 1.3$ ) and that the sand roughness appears to yield larger percentages of filaments at a slightly lower value of the relative filament length. All in all, the majority of the filament lengths vary from 0.8 to about 1.8 and outside that range sand roughness produces very little or no filaments. However, the beads seem to give rise to filaments as large 2.3 ( $L_f/h_0 = 2.3$ ) or so.

Figure 11 is a combined plot of Figs. 9 and 10 for the purpose of bringing into closer focus the relative differences between the beads and sand roughness.

Figure 12 and 13 present the comparison of the relative filament diameter for the case discussed in connection with Figures 9 through 11.

Once, again it is noted that there is relatively little difference between the characteristics of filaments between the two roughnesses.



No.	Analysis for comparisons on histograms	Case	Notes
1	Two types of roughness	A, D	Sand & Beads, flat plates
2	Two jet thicknesses	C, E	Flat plates, different Fr & We
3	Rod and plate same fine roughness	A, B	Same Fr & We, $k/ho = 0.02$
4	Two degrees of roughness	A, C	$(k/ho) = 0.02, 0.06$ , rod & plate
5	Three jet thickness	A, C, E	Jet thickness (mm) = 7.9 (rod) 5.8 (plate) 14.0 (plate)
6	Three Fr medium roughness	C, D, E	(one) Fr = 25.8, plate (sand) (two) Fr = 16.6, plates (sand, beads)

Table 4. Summary of the Cases for Analysis for the Eulerian Method of Description.

This indicates that the relative roughness of the surface rather than the individual shape of the roughness elements determine the interior as well as the exterior structures of the jet. This is, somewhat, anticipated on the basis of the numerous studies carried out on the effect of roughness and close conduits.

Figure 14 shows that the largest filament diameters are about 20 percent of the jet thickness but the largest occurrence of filaments of diameters are 0.13 ( $D_f/h_o = 0.13$ ).

Figures 15 and 17 show the individual as well as the combined histograms of the relative drop diameters for bead-roughened and sand roughened plates. The effect of the type of roughness is relatively small and the largest droplet diameters are 20 to 30 percent of the jet thickness. Surprisingly enough outside this range the occurrence of the droplet of any significance size reduces rapidly.

In summary, the comparison between beads and sand type of roughness is that beads give rise to longer and skinner ligaments and somewhat larger droplets relative to those generated by the sand.

Case No.2: Figures 18 through 26 show the filament length, filament diameter and drop diameter for the same conditions of relative roughness, Froude and Weber numbers, with the sole exception of the jet thickness. Evidently the jet thickness changes the Froude and Weber numbers. However, in order to minimize the change in the governing parameters the relative thickness ( $k/h_o$ ) is maintained at 0.06 ( $k/h_o = 0.06$ ).

The comparison of Figs. 20, 23, and 26 show that the larger the jet thickness, the larger the frequency of occurrence of the filaments. Likewise, filaments get much thinner. From a practical point of view, whether the object is to reduce the drop diameters, filament diameters and filament lengths it will be far more advantageous to increase the jet thickness for a given relative roughness. It should also be pointed out that for certain industrial applications it maybe desirable to have large droplets and longer filaments. For such cases, it will be necessary to use thinner jets at higher jet velocities.

Case No. 3: Figures 27 through 35 show the comparisons of the relative filament lengths. Filament diameters, and drop diameters for two different jets, one over a rod and the other over a plate of identical relative roughness. In particular, Figs. 29, 32, and 35

show that the jet over the rod yields relatively smaller filaments and droplets at a higher percentage. In particular, the drop diameters for the rod are about 20 percent smaller.

Case No 4: Figures 36 through 44 show the comparisons of the relative filament lengths, filament diameters, and drop diameters for two different jets, one over a rod, and the other over a plate, as in Case 3, but with different relative roughnesses. In particular, Figs. 38, 41, and 44 show that the jet over the rod yields relatively larger filaments and droplets at a higher percentage in spite of the fact it has a smaller relative roughness.

Case No. 5: Figures 45 through 56 show the comparisons of the relative filament lengths, filament diameters, and drop diameters for three different jet thicknesses, one over a rod and the other over two plates, all of identical relative roughness. In particular, Figs. 48, 52, 56 show, upon a cursory look, that the thicker the jet, the smaller the characteristics of the filaments and droplets. However, one must bear in mind that the thickest jet has a smaller Froude number, a fact that cannot be avoided due to the experimental circumstances. Nevertheless, the comparison of only two cases with identical Froude numbers and with nearly identical jet thicknesses shows that the Weber number does not significantly affect the filament and droplet characteristics.

Case No. 6: Figures 57 through 68 show the comparisons of the relative filament lengths, filament diameters, and drop diameters for three cases where the relative roughness is identical but one of the Froude numbers is considerably larger. In particular, Figs. 60, 64, 68 show that the characteristics of the filaments and droplets are nearly identical for the two cases where the Froude numbers is identical. On the other hand, for the case with the larger Froude number, all of the characteristics of the filaments are considerably larger than the other two. The invariable conclusion is that the Froude number governs the free surface phenomena under consideration.

In the following, we will describe the characteristics of single filaments as they are observed in a moving frame of reference. In other words, unlike the previous cases where many filaments are observed from a stationary platform, here only a single filament and its evolution are traced as a function of time, i.e., in a Lagrangian frame of reference.

Figures 69 through 84b show, through the use of eight filaments each, the pictorial view of the evolution of a filament and the vertical displacement of its tip and centroid on both dimensional and normalized forms. It appears that the form and the rate of rise depends when the observation began, under what circumstances the filament was created, the duration of the observation, and on the unusual eddy-events that may take place in the course of the filament evolution.

Figures 70a-70b, 72a-72b, 76a-76b, and 80a-80b show that there are three distinct regions in the evolution of the vertical displacement. The first part (about the first 10 ms) exhibits a slow rise with a relatively small ejection velocity. The third part (after about 15 ms) shows a steeper rise and relatively larger vertical velocity. However, the intermediate region (the second part) exhibits a gradual transition from one state to the other and thus an acceleration, unlike the other two cases.

Figures 74a-74b, 78a-74b, 82a-82b, and 84a-84b show opposite trends of rise relative to those cited above, even though they still exhibit the same three identifiable regions. In the first region, there is a steady rise, at a velocity relatively larger than those seen, for example, in Figs. 70a-70b and 82a-82b, unlike the cases discussed previously. The intermediate region shows either complex (Figs. 74a-74b) or relatively simple transitions between the two end regions.

The detailed understanding of the events described above will require the analysis of many more filaments in the Lagrangian frame of reference. Nevertheless, it now appears that there will be several distinct regions in the evolution of each filament: A short period of slow growth, a period of transition to a higher or lower velocity, and eventually an inevitable transition to a lower velocity as the filaments or droplets return to the main stream. Obviously, a large pool of data must be evaluated in order to classify various types of ejections or filament creations. A large family of such realizations will then permit one to discover a series of filament families which help to quantify the eddies by size, by velocity, and by acceleration during their inception.

THIS PAGE LEFT INTENTIONALLY BLANK



## IV. CONCLUSIONS

The following conclusions are warranted based on the observations and measurements made in this investigation:

- The characteristics of the free-surface structures (filaments and droplets) are of a statistical nature and can best be described in terms of histograms.
- The free surface provides a path for interaction between the above surface events and the internal flow dynamics. This interaction guarantees that the characteristics of the filaments and drops will depend on the dynamics of the jet and the condition of the surface on which it is flowing.
- The characteristics of the filaments and droplets (length and diameter, among others) resulting from the wall jets (half-free jets) depend primarily on the relative wall roughness and the Froude number within the range of Weber numbers encountered.
- Wall jets of smaller Froude number give rise to shorter filaments and smaller droplets in narrower ranges of the filament length and diameter, confirming the fact that the ligament formation is essentially an inertial phenomenon.
- The filaments are not created equal and are not born into identical circumstances. However, they undergo a period of slow growth, one or more periods of transition to different vertical velocities, and eventually, a period of fall to the main stream. The detailed characterization of these events and their relation to the underlying eddy motion will require a much larger pool of data.

THIS PAGE LEFT INTENTIONALLY BLANK

## APPENDIX

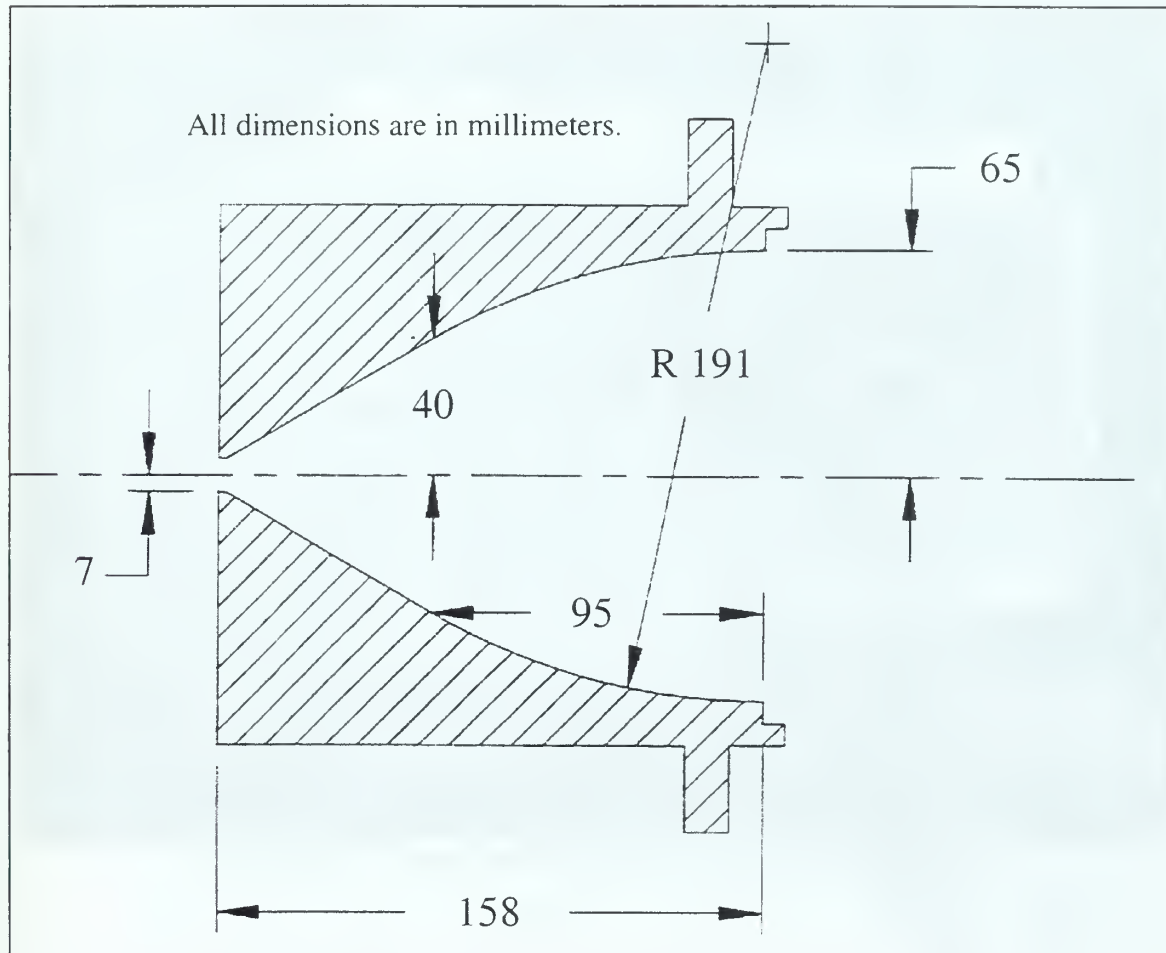


Figure 1. CAD drawing of the rectangular liquid wall jet nozzle.

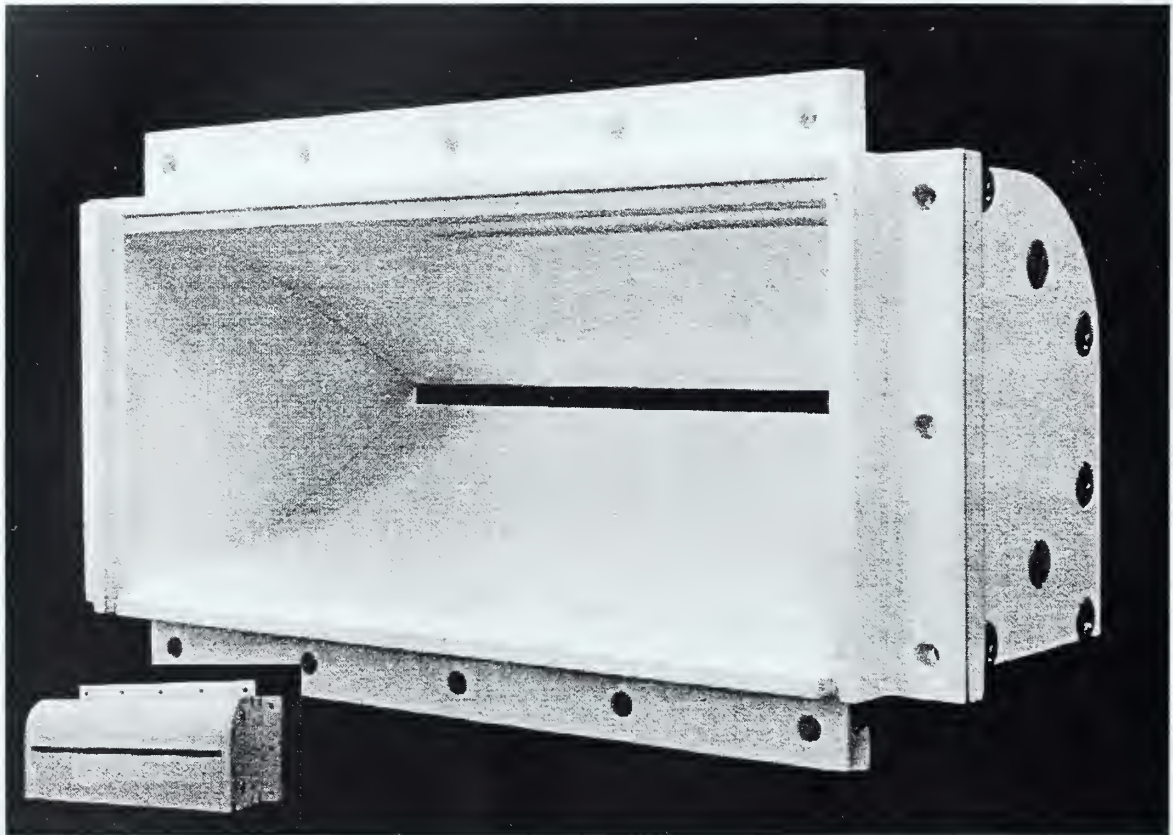


Figure 2. Photograph of the rectangular liquid wall jet nozzle.

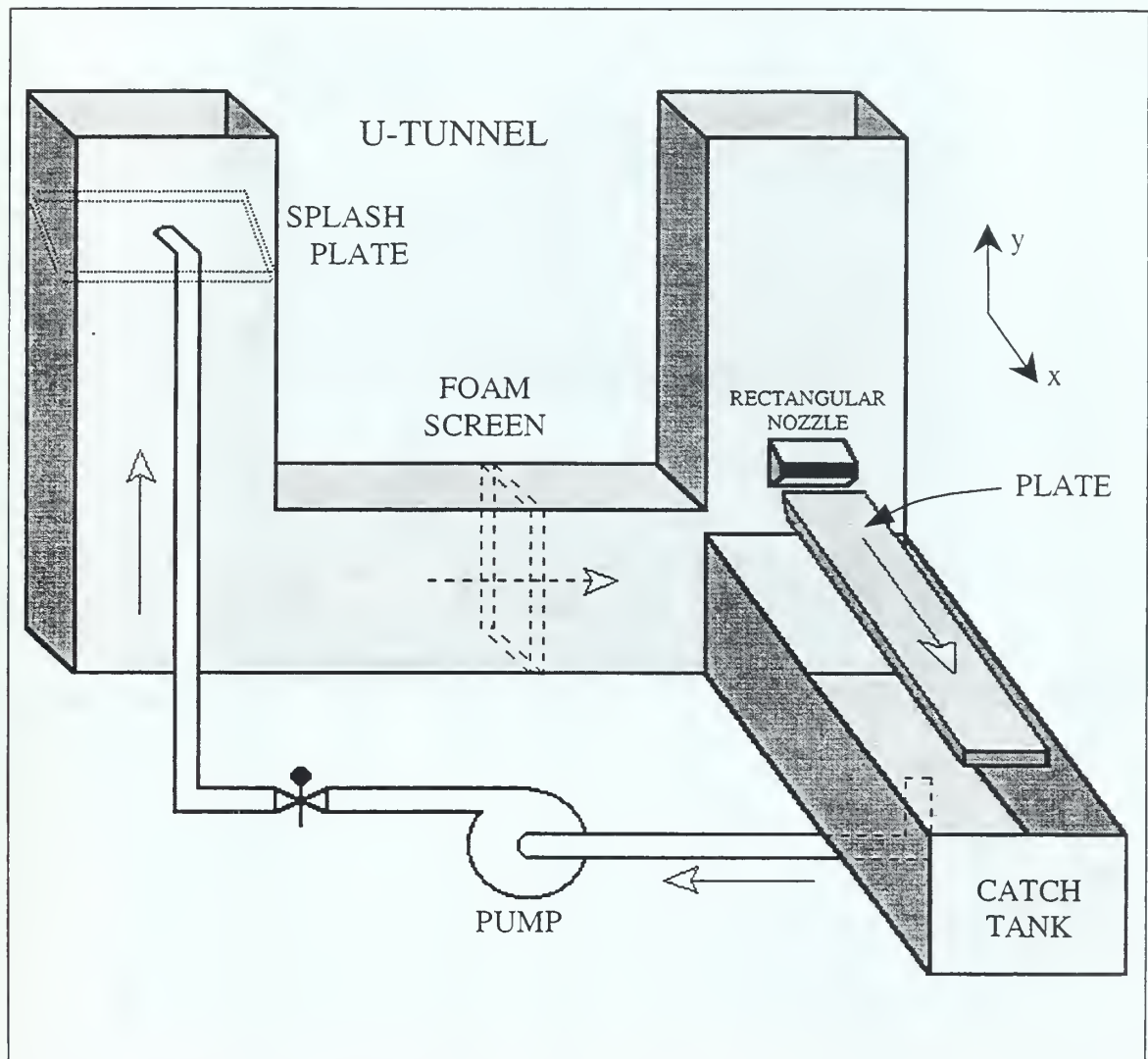


Figure 3. Equipment arrangement for the rectangular liquid wall jet experiments, with the fluid flow path indicated by the arrows.

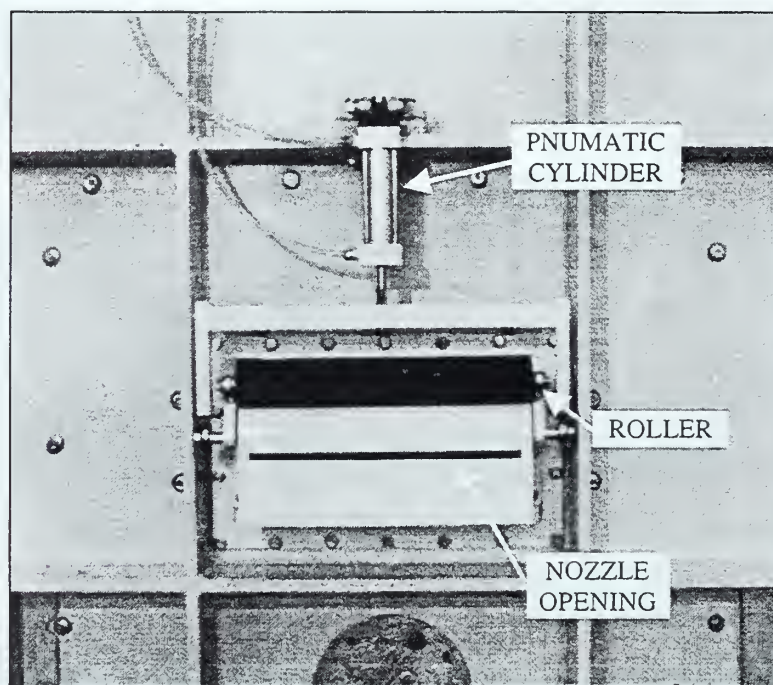


Figure 4. Photograph of the outside of rectangular nozzle with the cylindrical gate open.



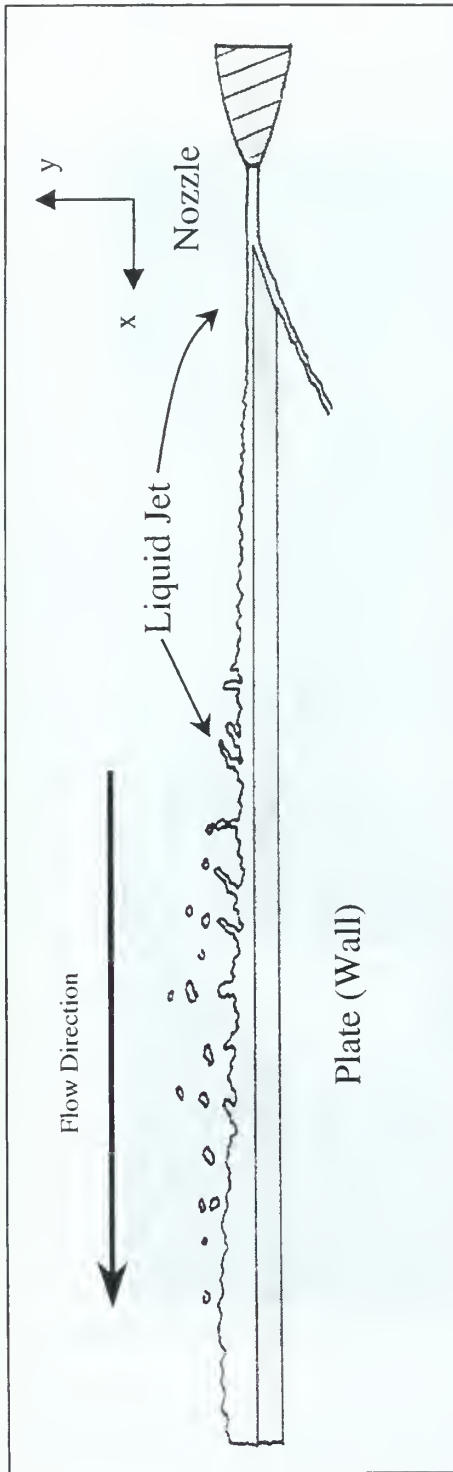


Figure 5a. Diagram of a liquid wall jet

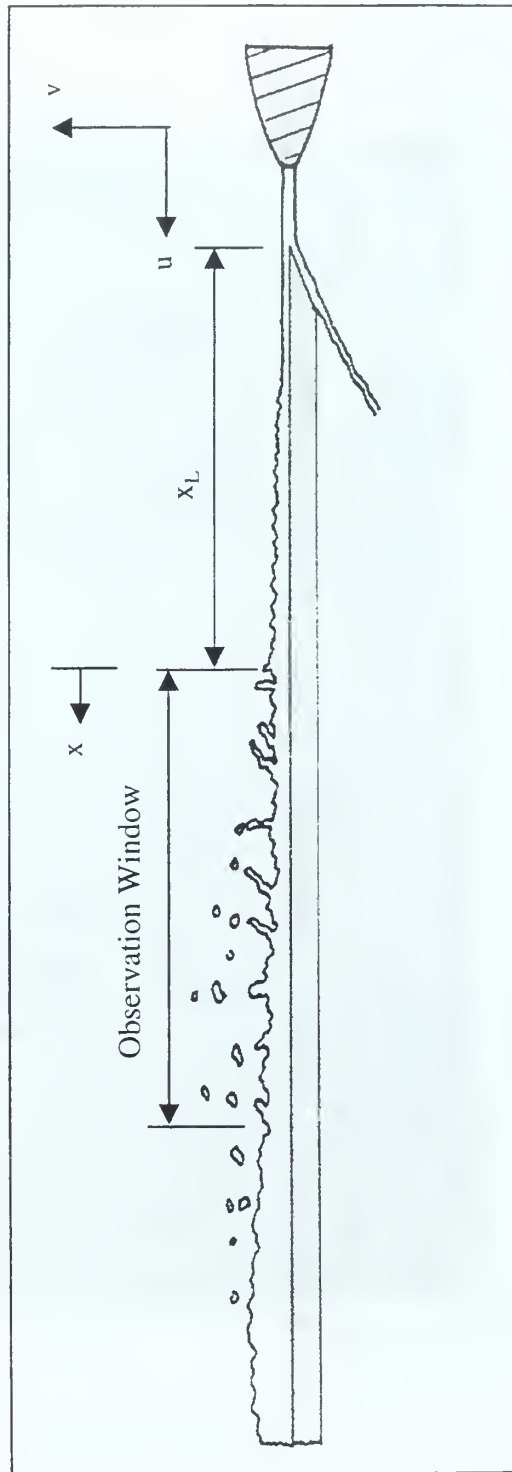


Figure 5b. Coordinate system used for Lagrangian method of description

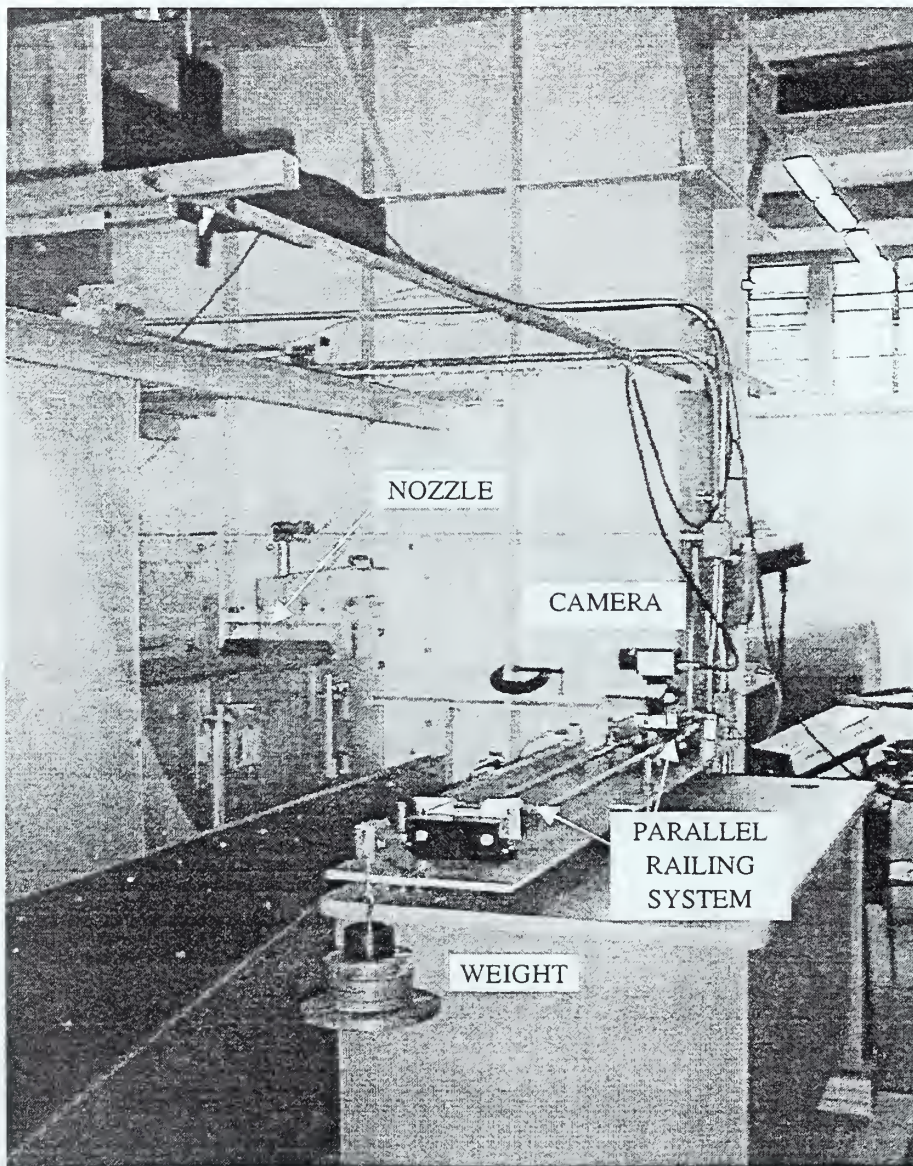


Figure 6. Photograph of the parallel railing system used for Lagrangian method of description.

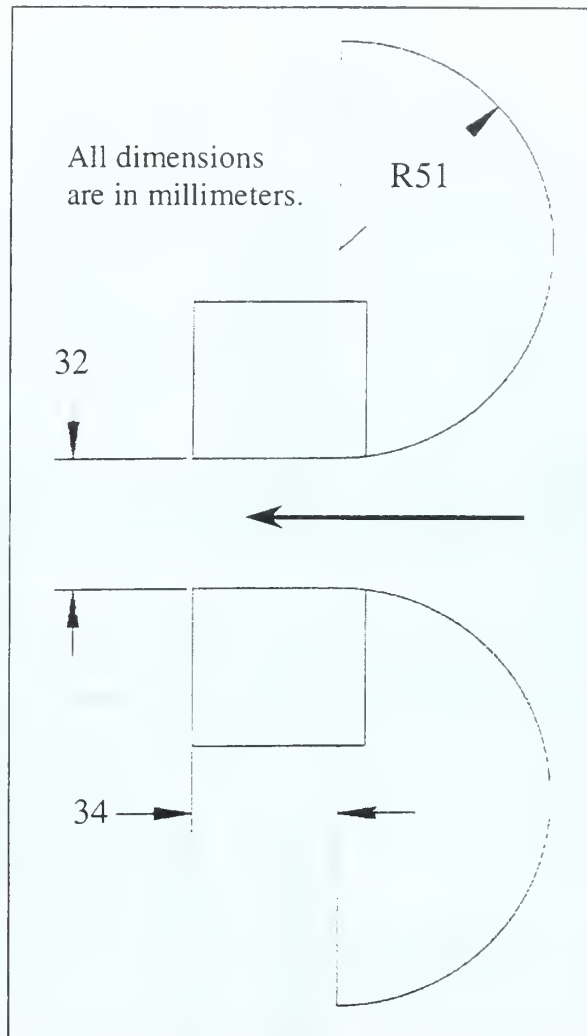


Figure 7. CAD drawing of the axisymmetric nozzle.

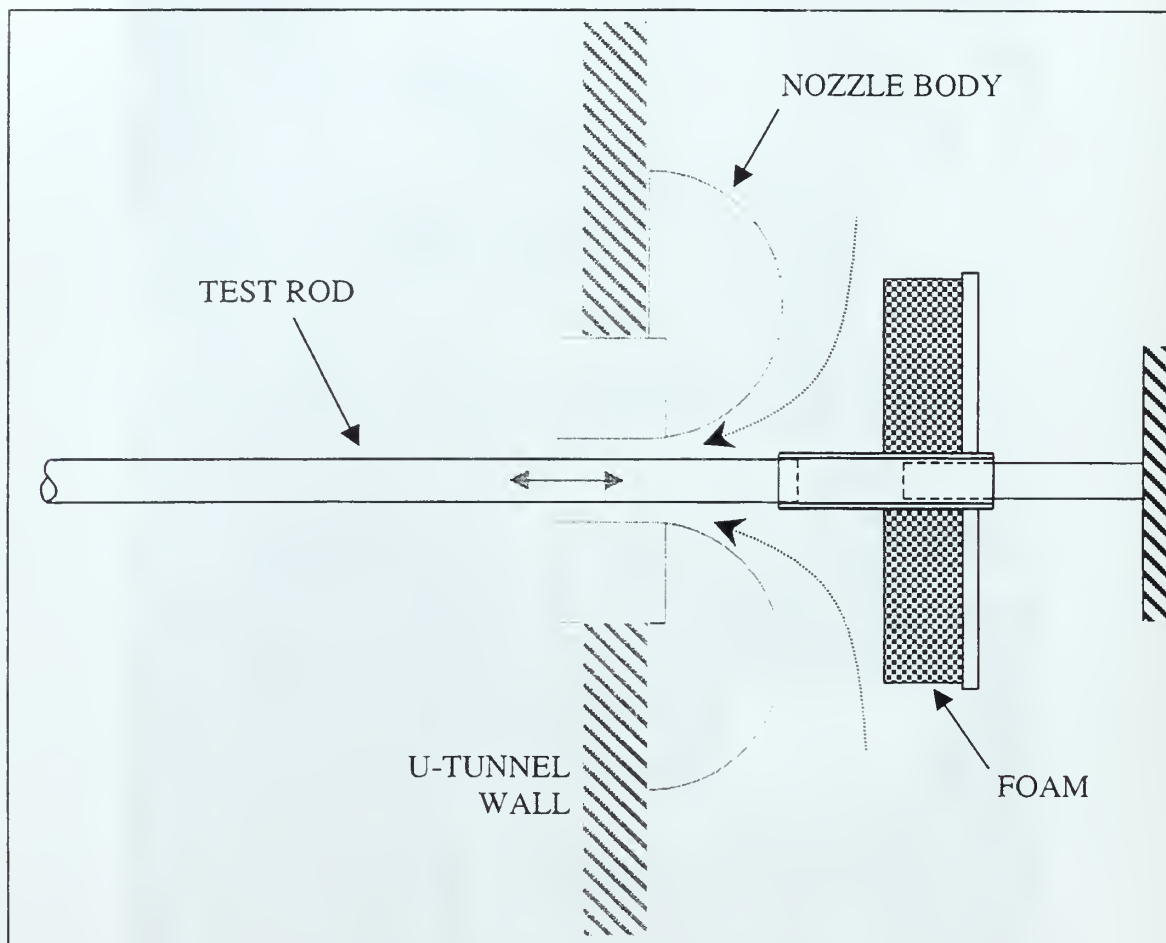


Figure 8. Side view of the axisymmetric nozzle with test rod assembly installed.

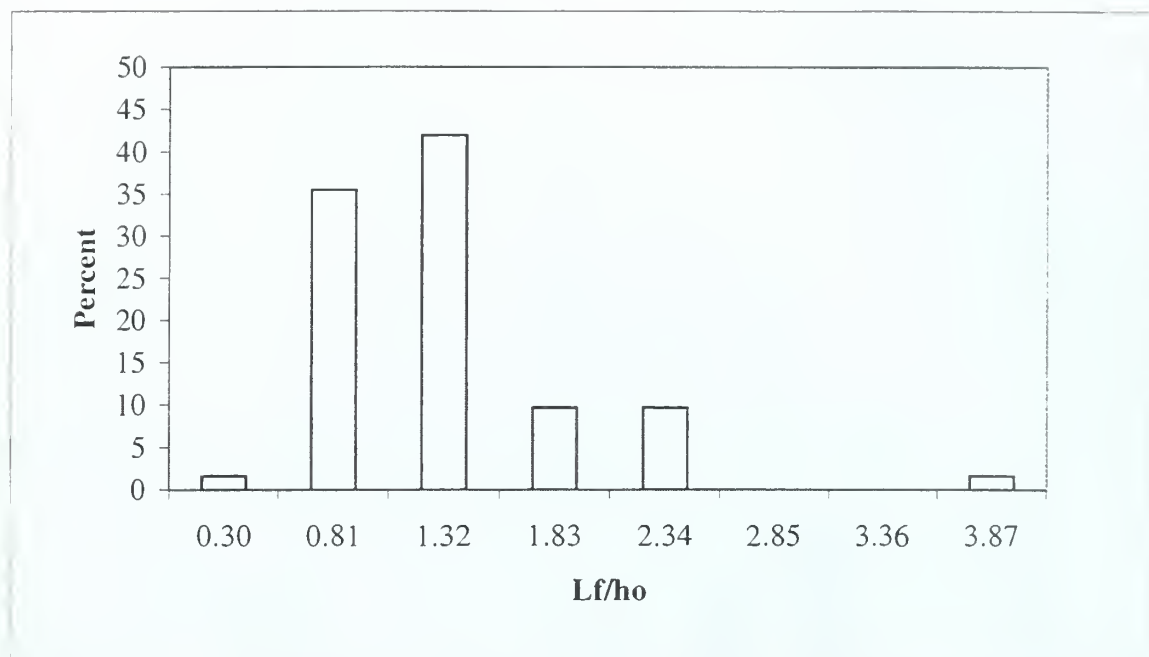


Figure 9. Distribution of the normalized filament length for bead roughness for wall jet thickness = 14mm ( $k/h_o = 0.06$ ,  $Fr = 16.6$ ,  $We = 7367$ ).

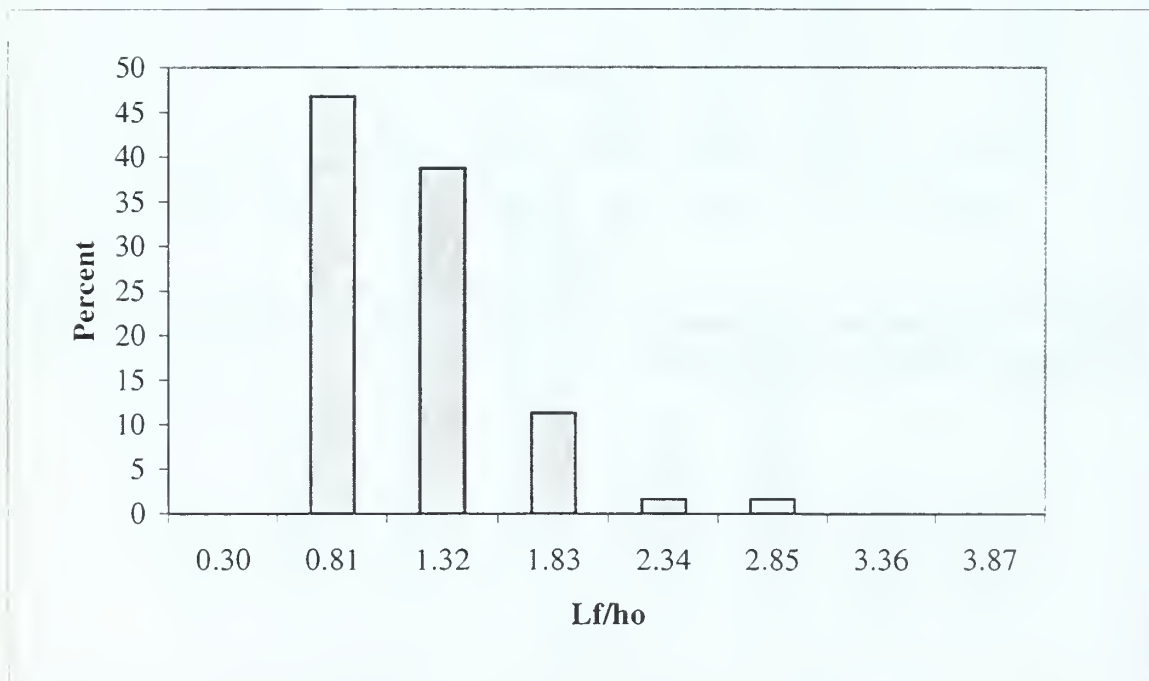


Figure 10. Distribution of the normalized filament length for sand roughness for wall jet thickness = 14mm ( $k/h_o = 0.06$ ,  $Fr = 16.6$ ,  $We = 7367$ ).



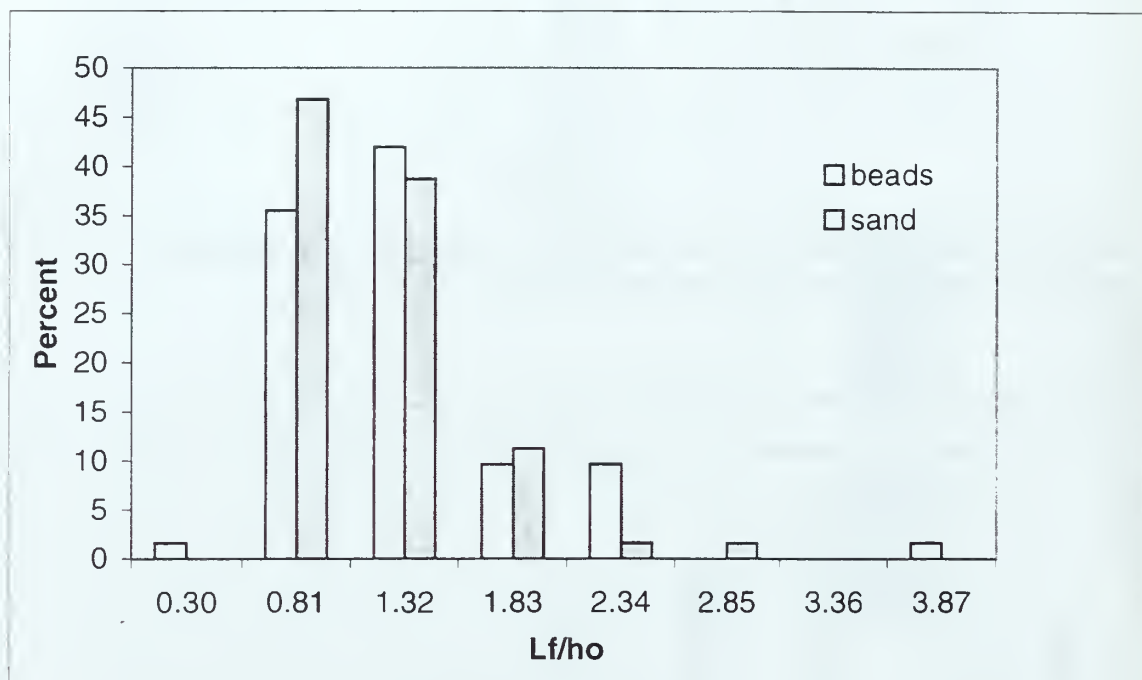


Figure 11. Comparison of the distributions of the normalized filament length for two types of roughness, beads and sand.

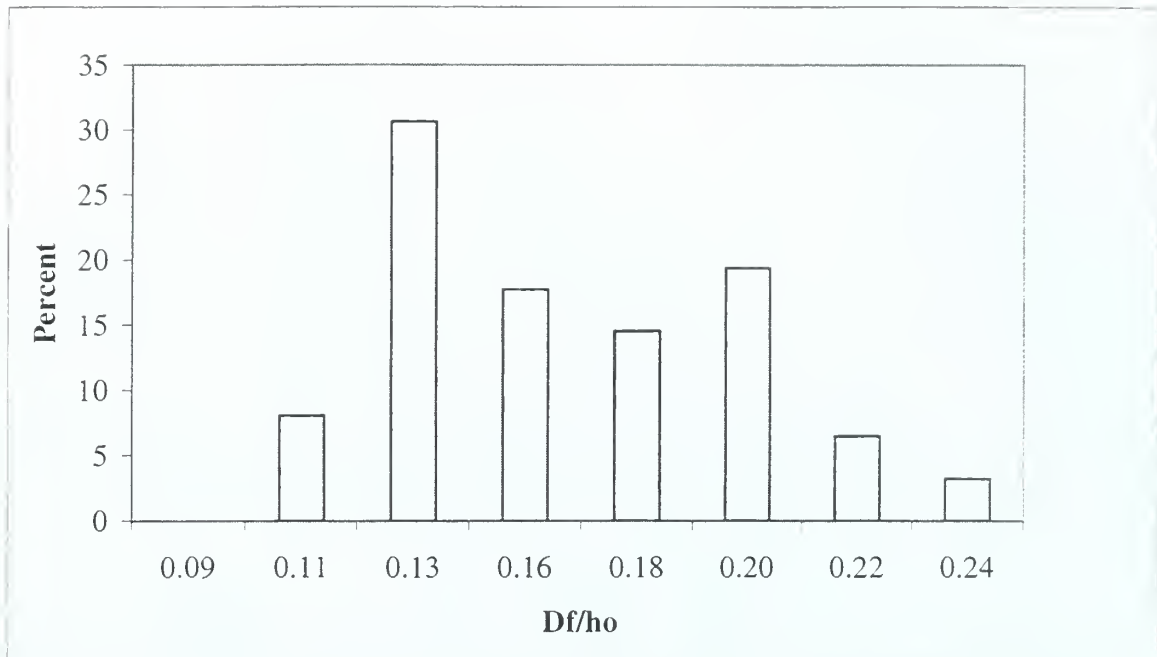


Figure 12. Distribution of the normalized filament diameter for bead roughness for wall jet thickness = 14mm ( $k/ho = 0.06$ ,  $Fr = 16.6$ ,  $We = 7367$ ).

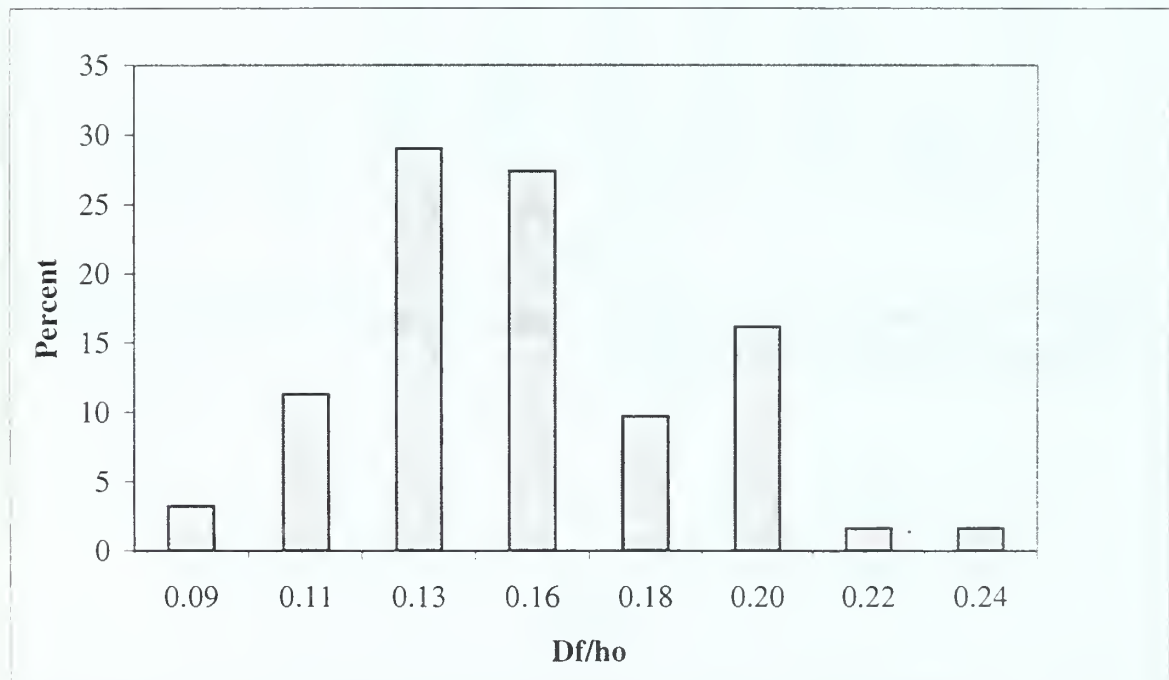


Figure 13. Distribution of the normalized filament diameter for sand roughness for wall jet thickness = 14mm ( $k/ho = 0.06$ ,  $Fr = 16.6$ ,  $We = 7367$ ).

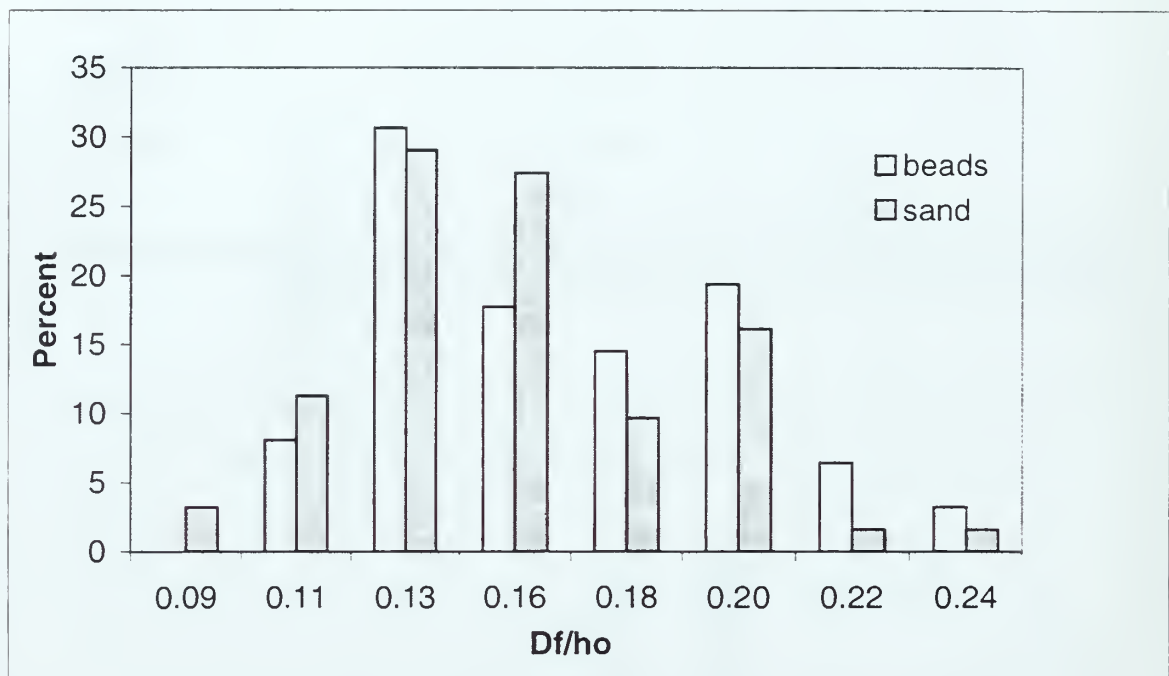


Figure 14. Comparison of the distributions of the normalized filament diameter for two types of roughness, beads and sand.

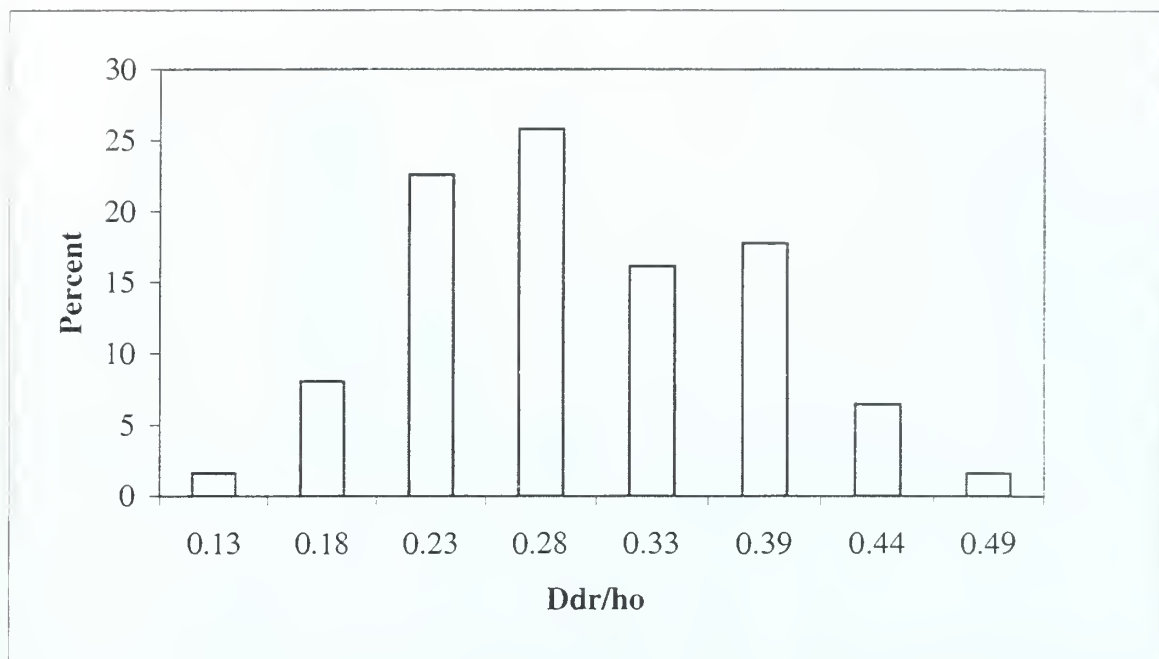


Figure 15. Distribution of the normalized drop diameter for bead roughness for wall jet thickness = 14mm ( $k/h_o = 0.06$ ,  $Fr = 16.6$ ,  $We = 7367$ ).

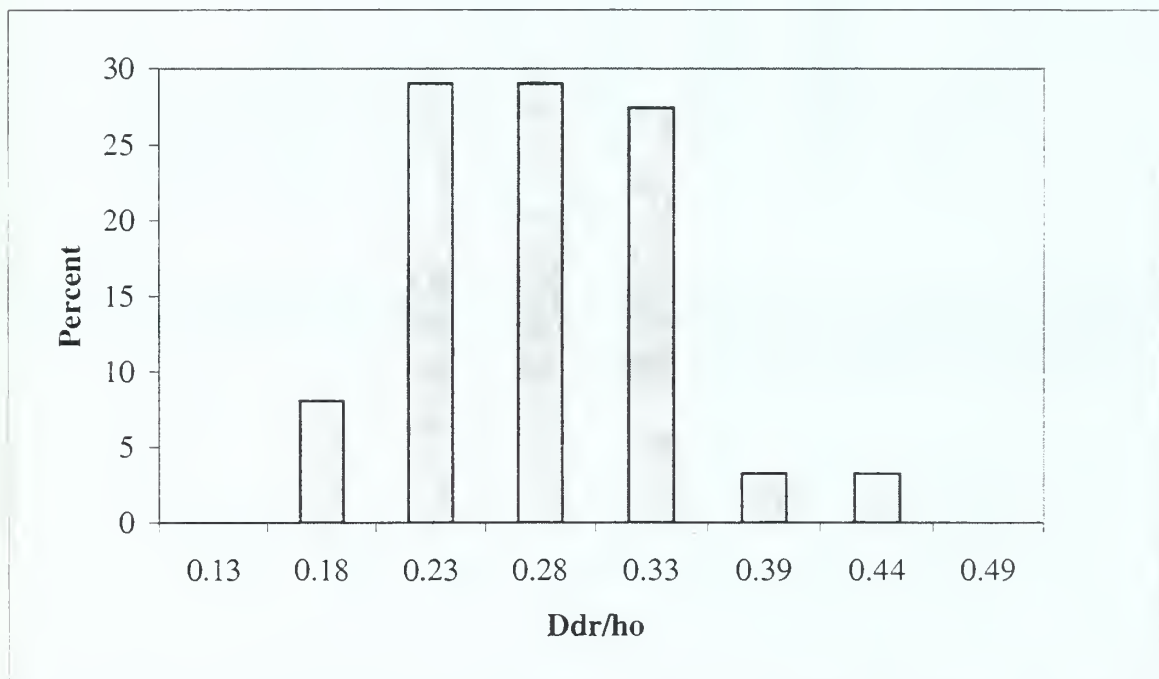


Figure 16. Distribution of the normalized drop diameter for sand roughness for wall jet thickness = 14mm ( $k/h_o = 0.06$ ,  $Fr = 16.6$ ,  $We = 7367$ ).

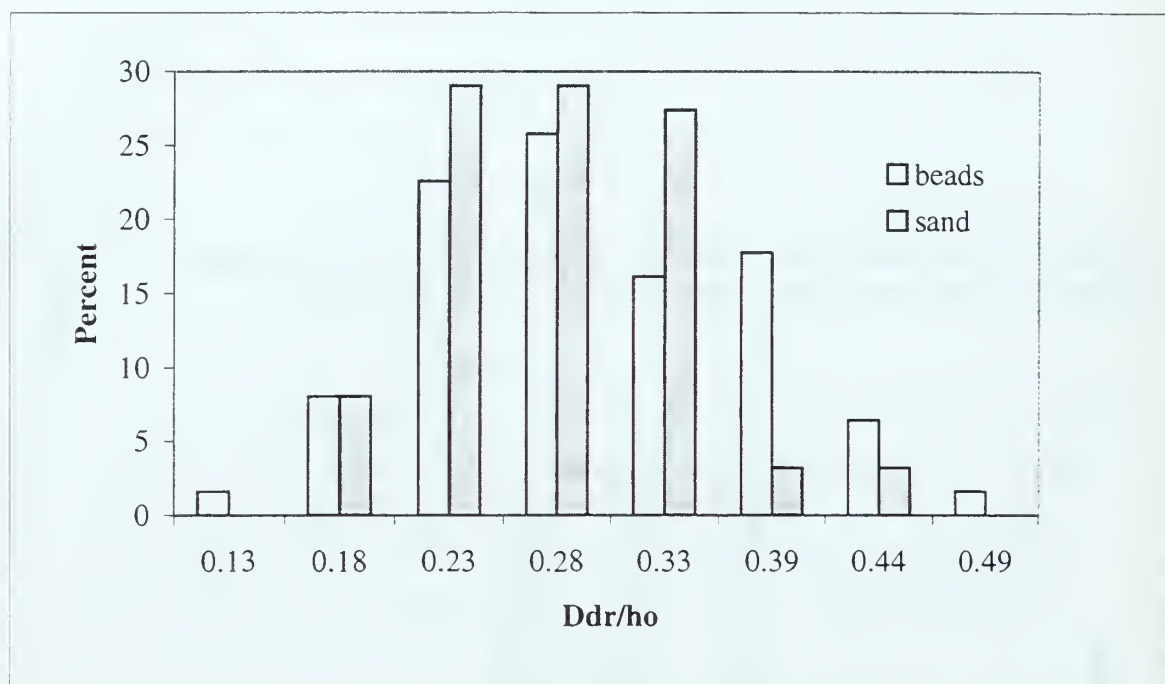


Figure 17. Comparison of the distributions of the normalized drop diameter for two types of roughness, beads and sand.



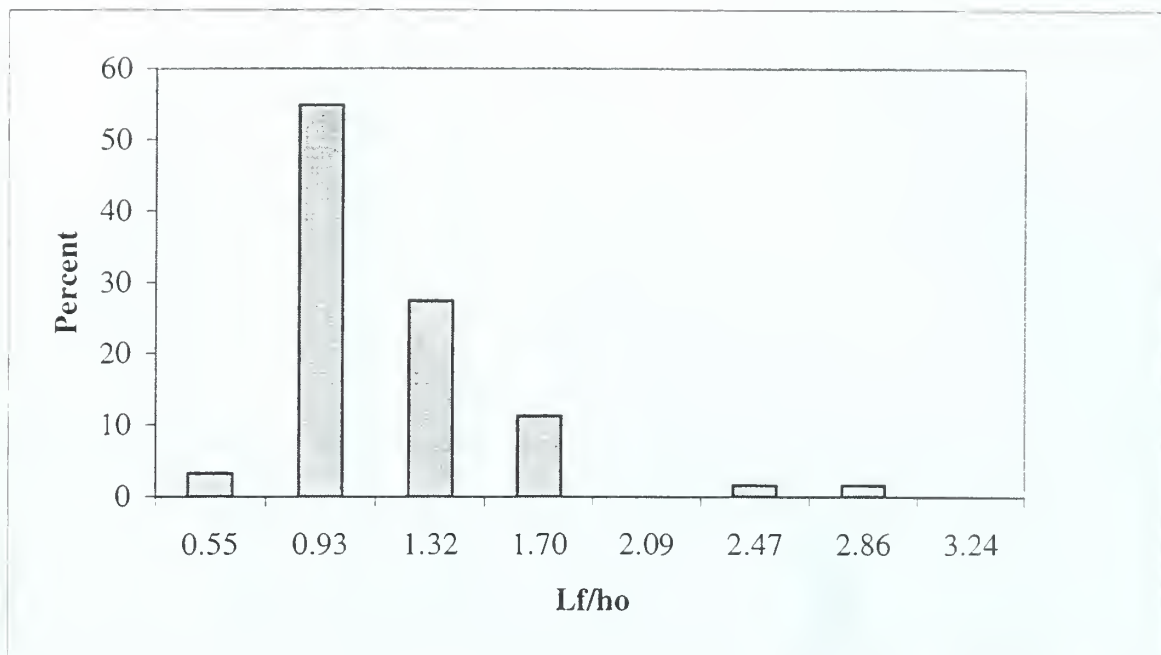


Figure 18. Distribution of the normalized filament length for the liquid wall jet with jet thickness = 14 mm ( $k/h_o = 0.06$ ,  $Fr = 16.6$ ,  $We = 7367$ ).

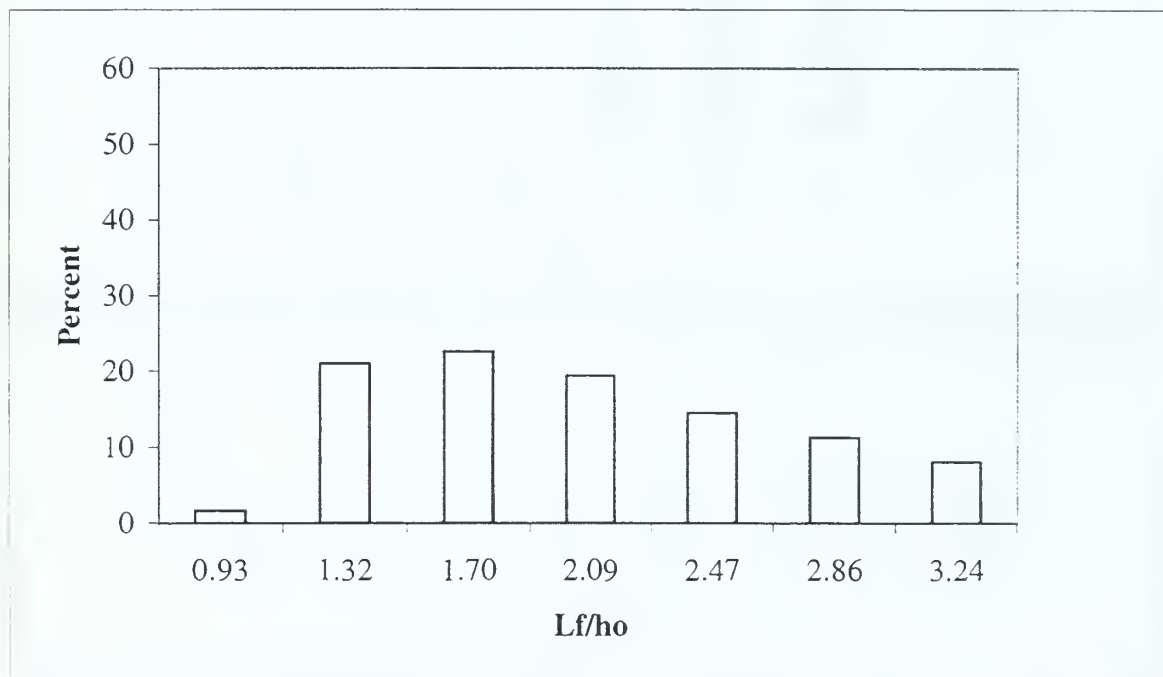


Figure 19. Distribution of the normalized filament length for the liquid wall jet with jet thickness = 5.8 mm ( $k/h_o = 0.06$ ,  $Fr = 25.8$ ,  $We = 3014$ ).

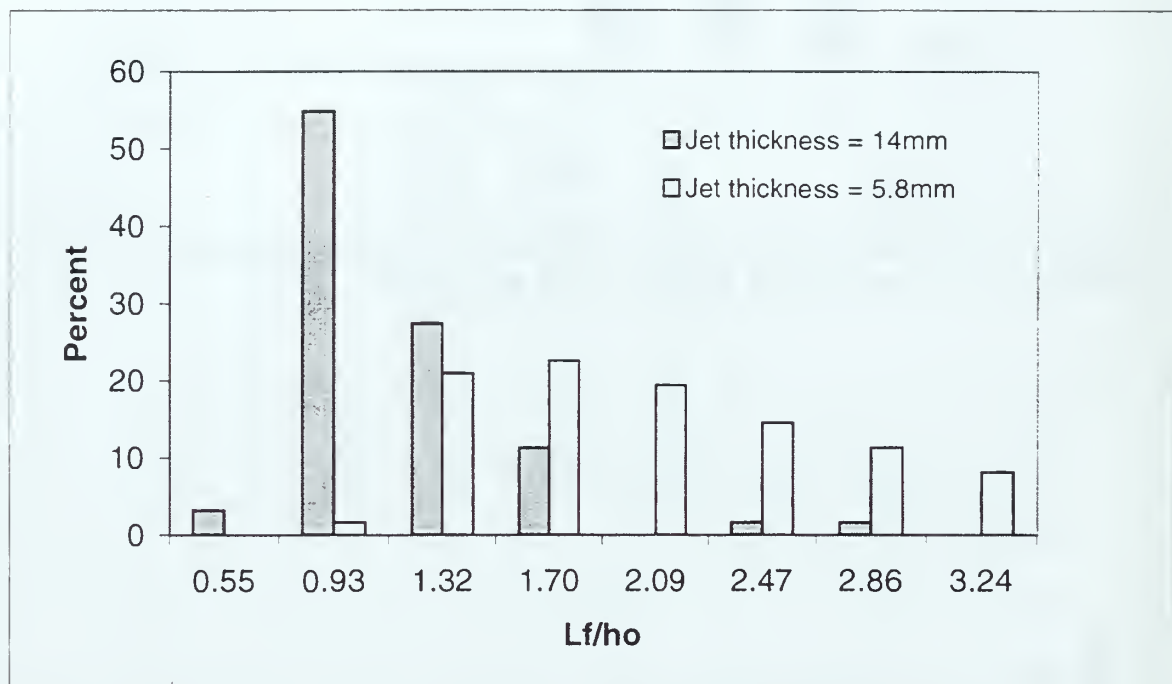


Figure 20. Comparison of the distribution of the normalized filament length for the liquid wall jet for two jet thickness.

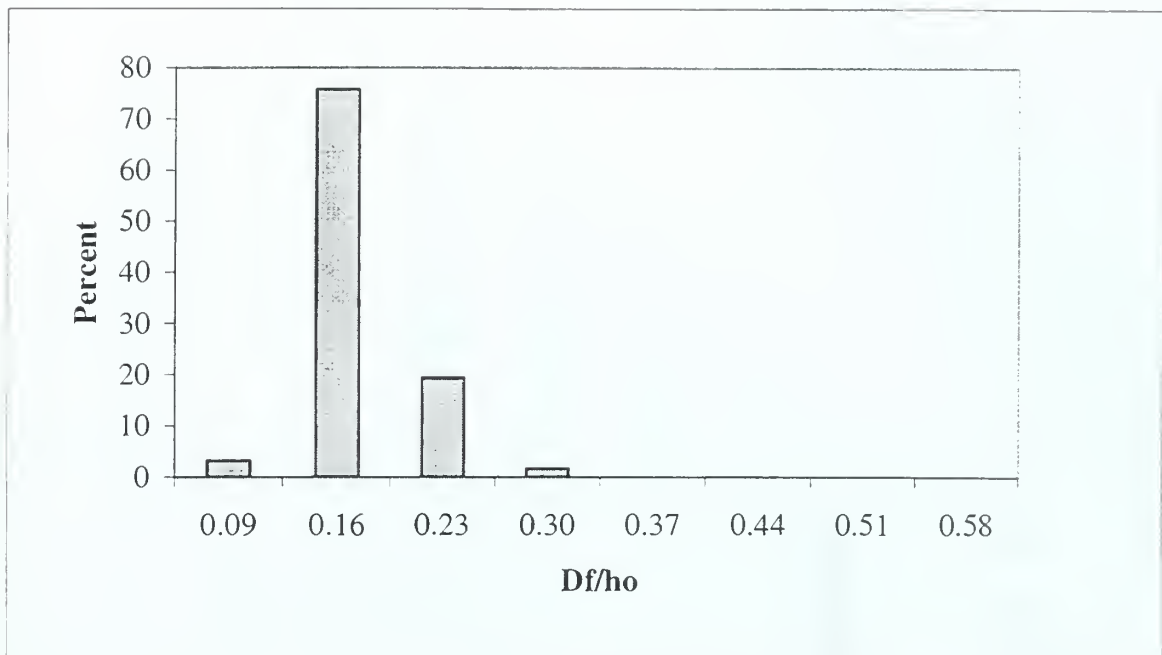


Figure 21. Distribution of the normalized filament diameter for the liquid wall jet with jet thickness = 14 mm ( $k/h_o = 0.06$ ,  $Fr = 16.6$ ,  $We = 7367$ ).

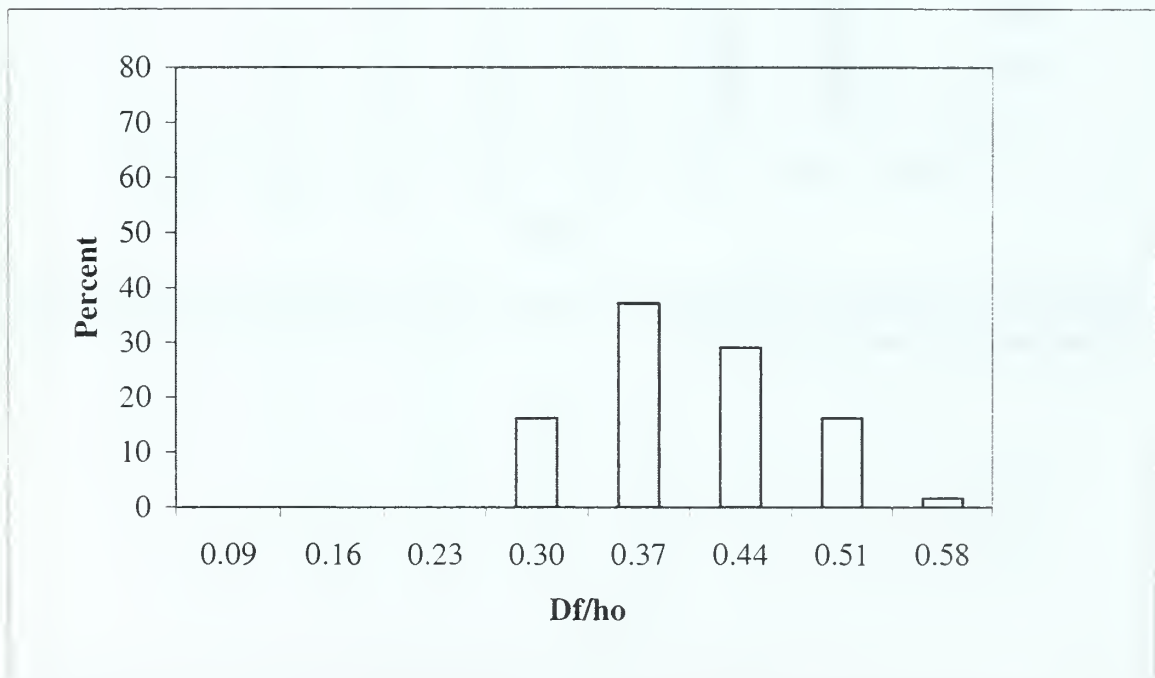


Figure 22. Distribution of the normalized filament diameter for the liquid wall jet with jet thickness = 5.8 mm ( $k/h_o = 0.06$ ,  $Fr = 25.8$ ,  $We = 3014$ ).

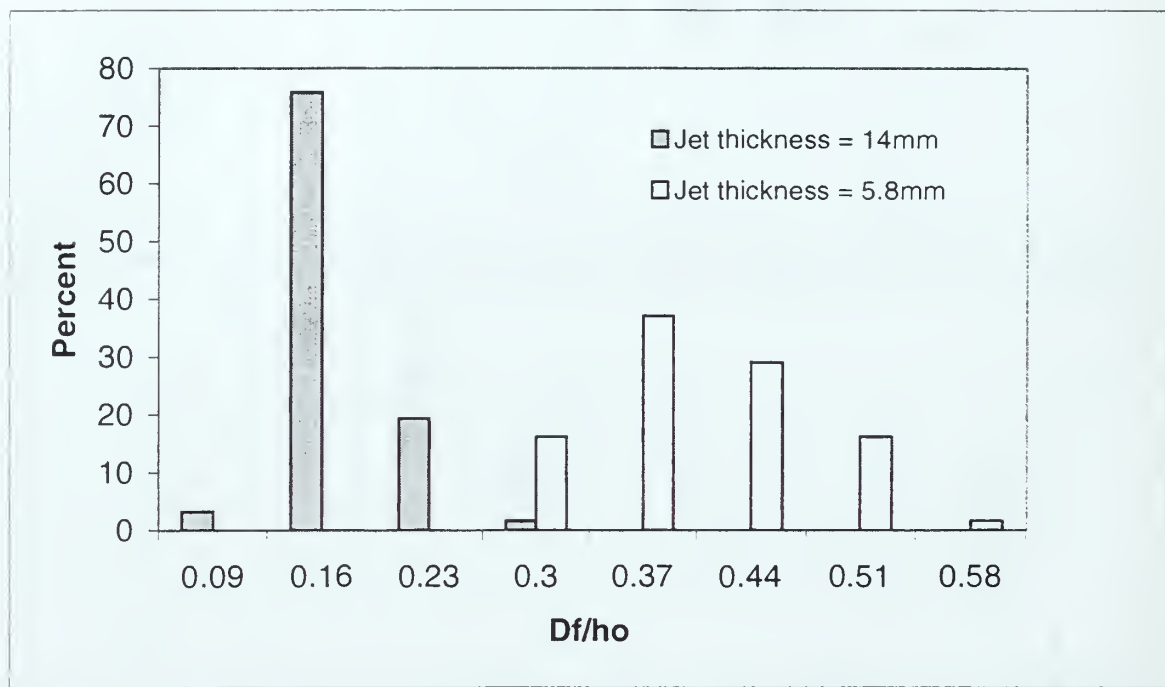


Figure 23. Comparison of the distribution of the normalized filament diameter for the liquid wall jet for two jet thickness.

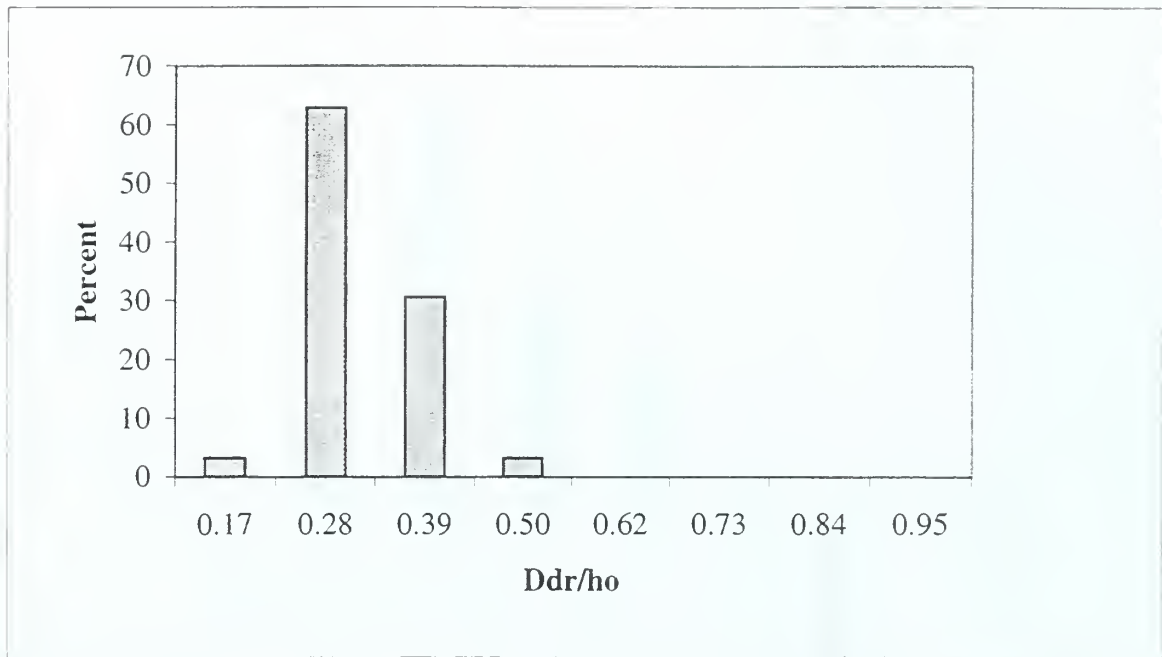


Figure 24. Distribution of the normalized drop diameter for the liquid wall jet with jet thickness = 14 mm ( $k/h_o = 0.06$ ,  $Fr = 16.6$ ,  $We = 7367$ ).

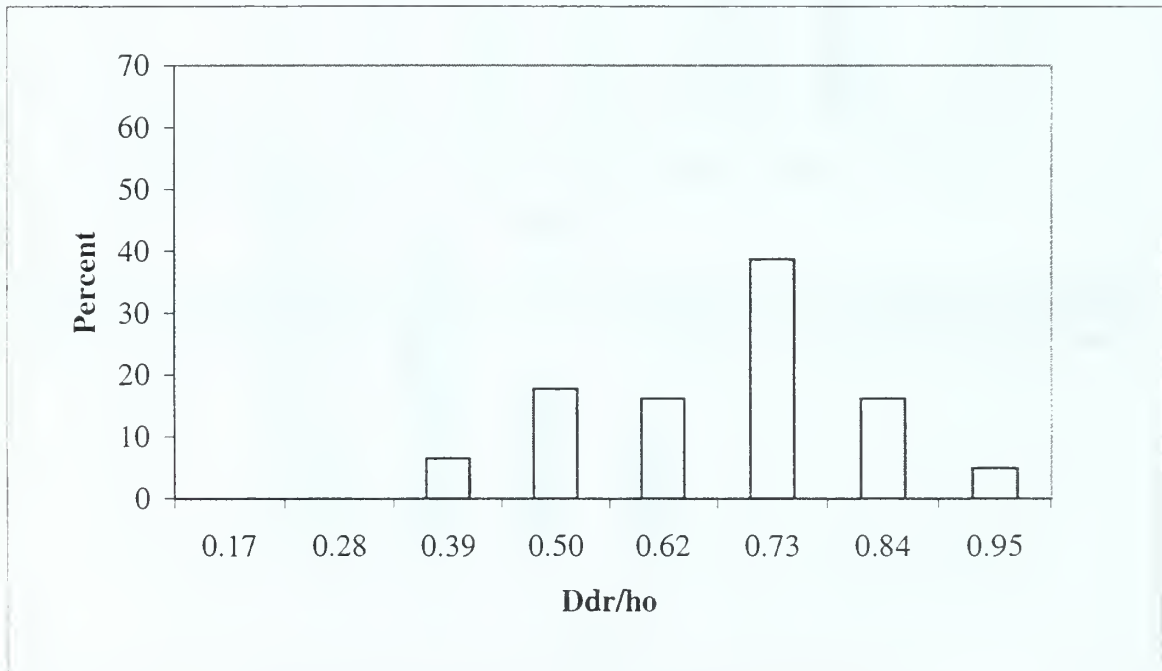


Figure 25. Distribution of the normalized drop diameter for the liquid wall jet with jet thickness = 5.8 mm ( $k/h_o = 0.06$ ,  $Fr = 25.8$ ,  $We = 3014$ ).



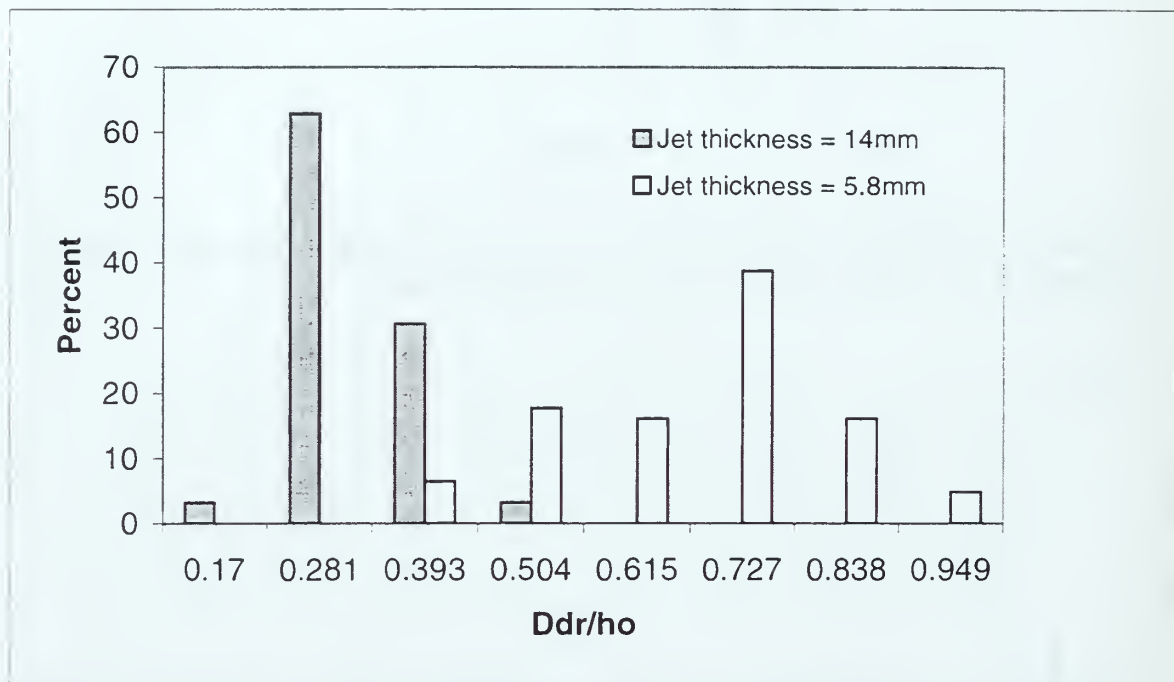


Figure 26. Comparison of the distribution of the normalized drop diameter for the liquid wall jet for two jet thickness.

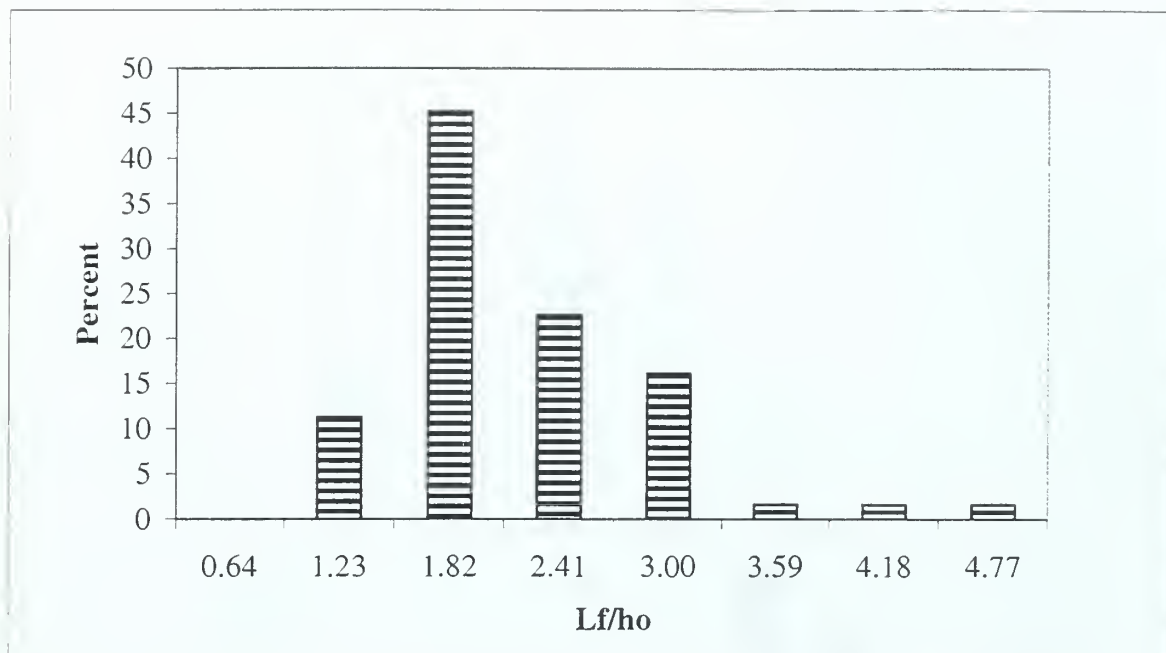


Figure 27. Distribution of the normalized filament length for the axisymmetric jet with roughness ( $k/h_o = 0.02$  ( $h_o = 7.9$  mm,  $Fr = 25.8$ ,  $We = 3014$ ).

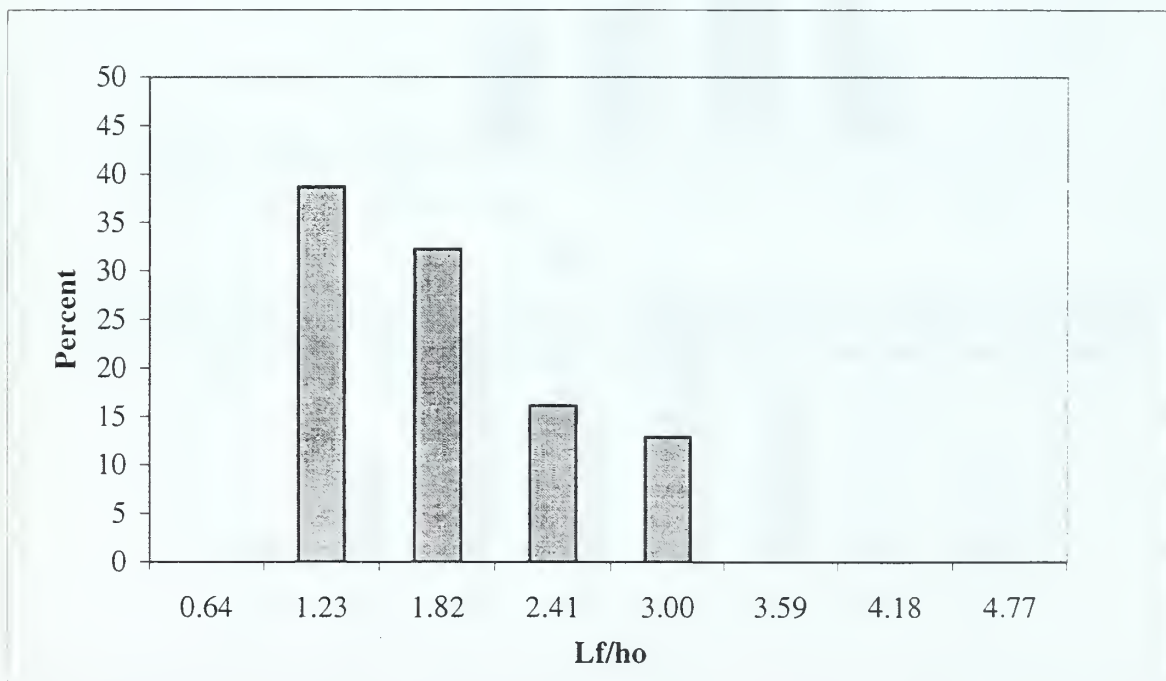


Figure 28. Distribution of the normalized filament length for the liquid wall jet with roughness ( $k/h_o = 0.02$  ( $h_o = 5.8$  mm,  $Fr = 26.5$ ,  $We = 2858$ ).

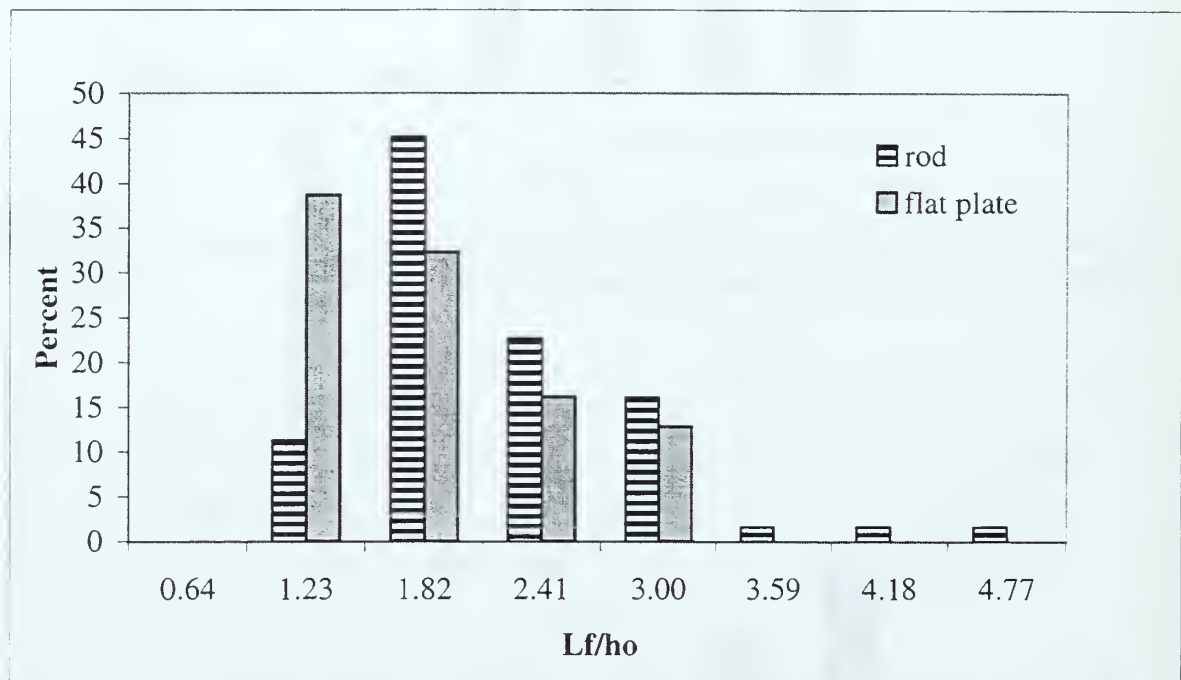


Figure 29. Comparison of the distributions of the normalized filament length for the axisymmetric and wall jet for the same relative roughness,  $k/h_o = 0.02$ .

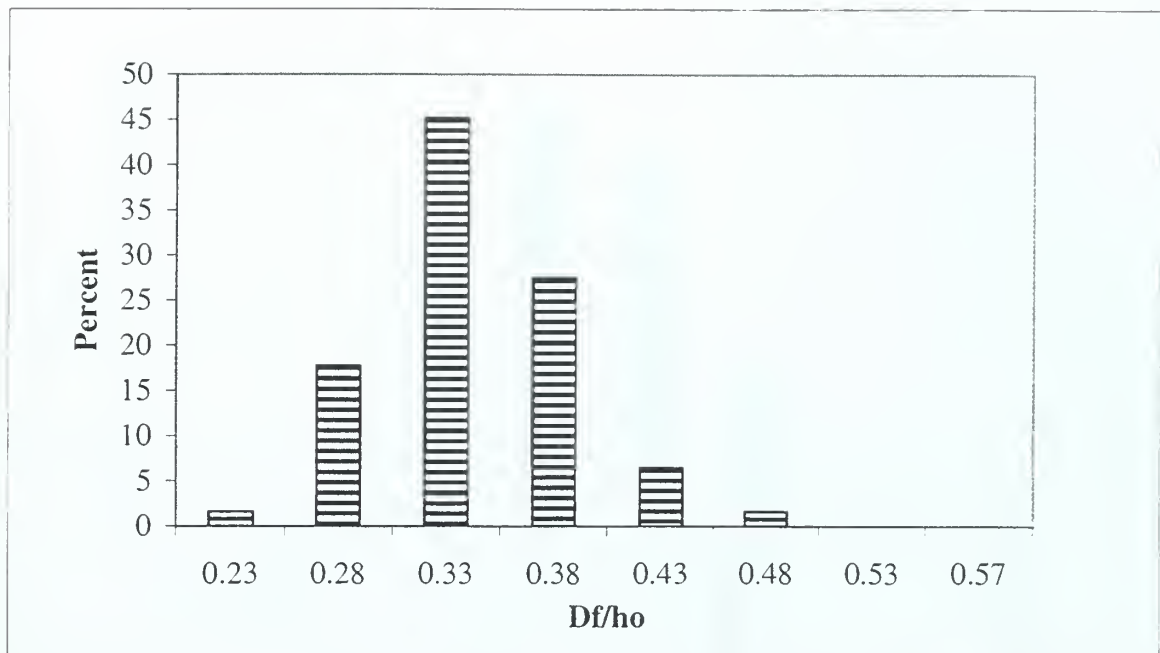


Figure 30. Distribution of the normalized filament diameter for the axisymmetric jet with roughness ( $k/h_o$ ) = 0.02 ( $h_o$  = 7.9 mm,  $Fr$  = 25.8,  $We$  = 3014)

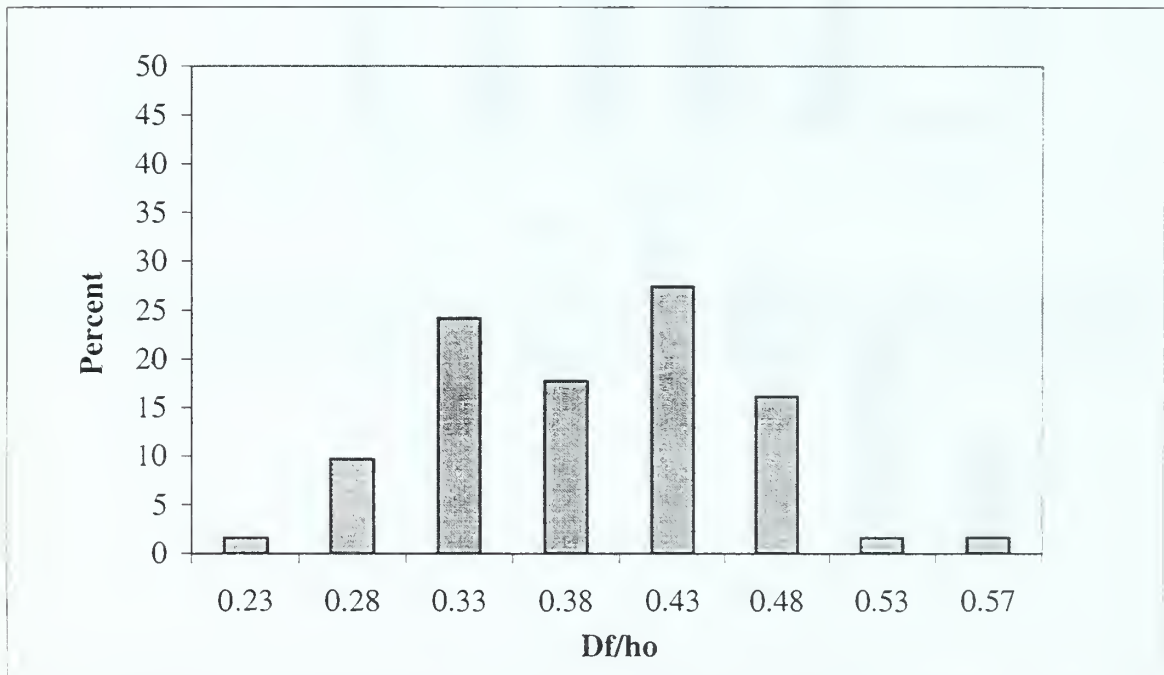


Figure 31. Distribution of the normalized filament diameter for the liquid wall jet with roughness ( $k/h_o$ ) = 0.02 ( $h_o$  = 5.8 mm,  $Fr$  = 26.5,  $We$  = 2858).

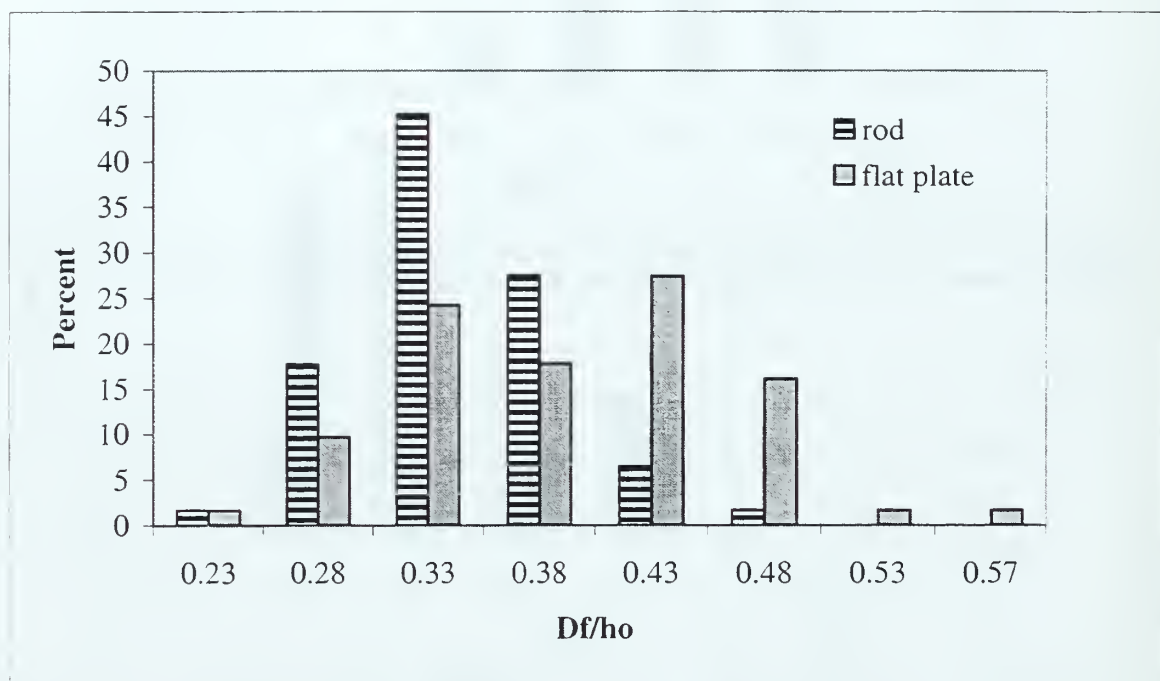


Figure 32. Comparison of the distributions of the normalized filament diameter for the axisymmetric and wall jet for the same relative roughness,  $k/h_o = 0.02$ .

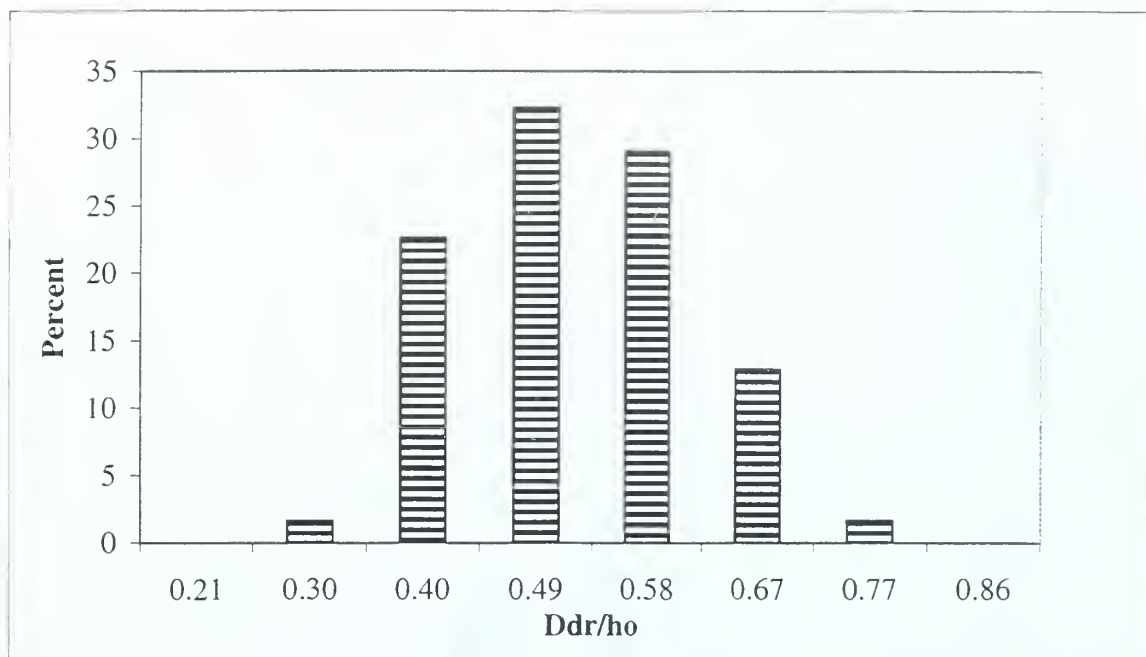


Figure 33. Distribution of the normalized drop diameter for the axisymmetric jet with roughness ( $k/h_o = 0.02$  ( $h_o = 7.9$  mm,  $Fr = 25.8$ ,  $We = 3014$ )).

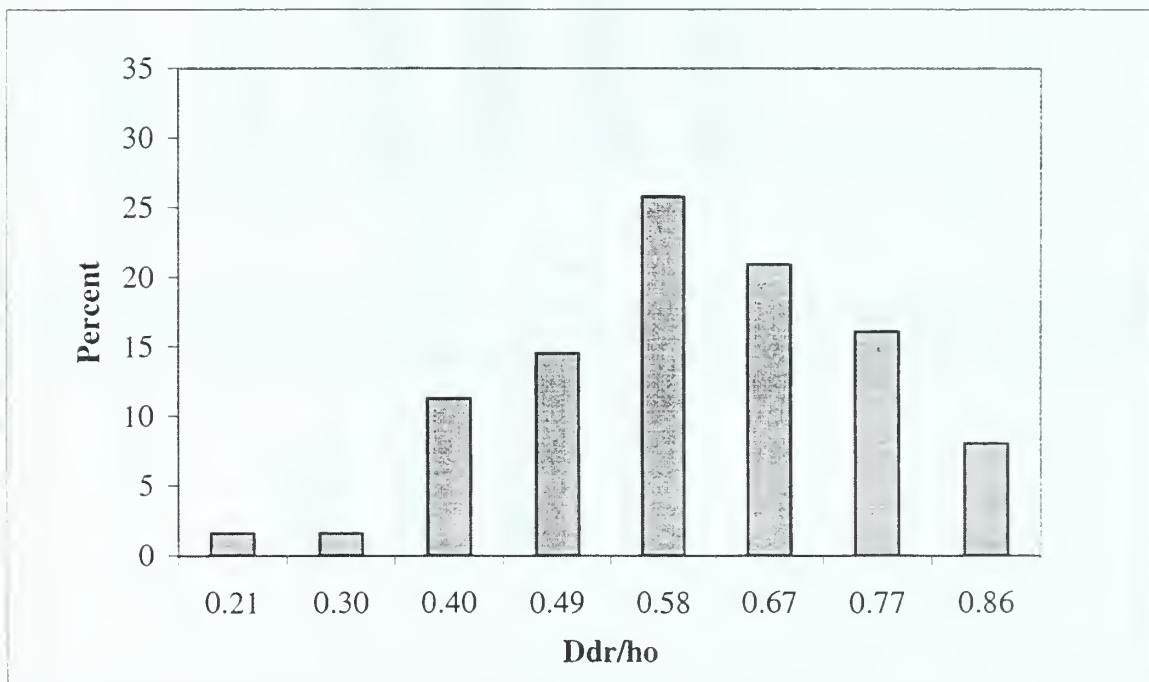


Figure 34. Distribution of the normalized drop diameter for the liquid wall jet with roughness ( $k/h_o = 0.02$  ( $h_o = 5.8$  mm,  $Fr = 26.5$ ,  $We = 2858$ )).



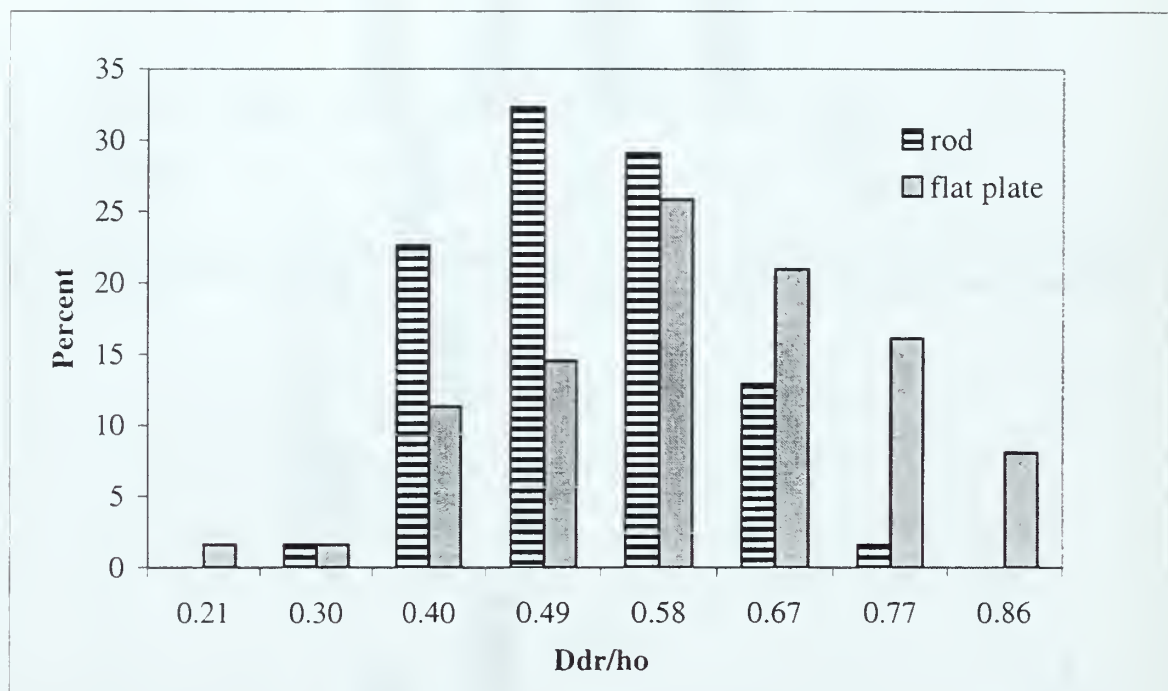


Figure 35. Comparison of the distributions of the normalized drop diameter for the axisymmetric and wall jet for the same relative roughness,  $k/h_o = 0.02$ .

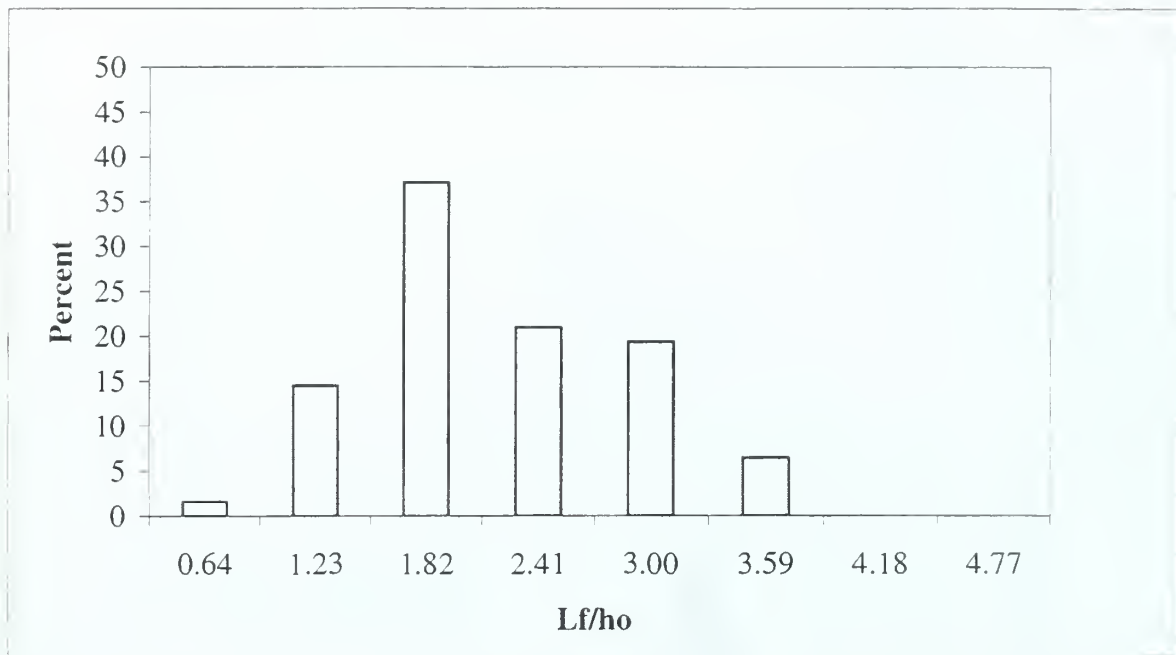


Figure 36. Distribution of the normalized filament length for the liquid wall jet with roughness ( $k/h_o = 0.06$  ( $h_o = 5.8$  mm,  $Fr = 25.8$ ,  $We = 3014$ )).

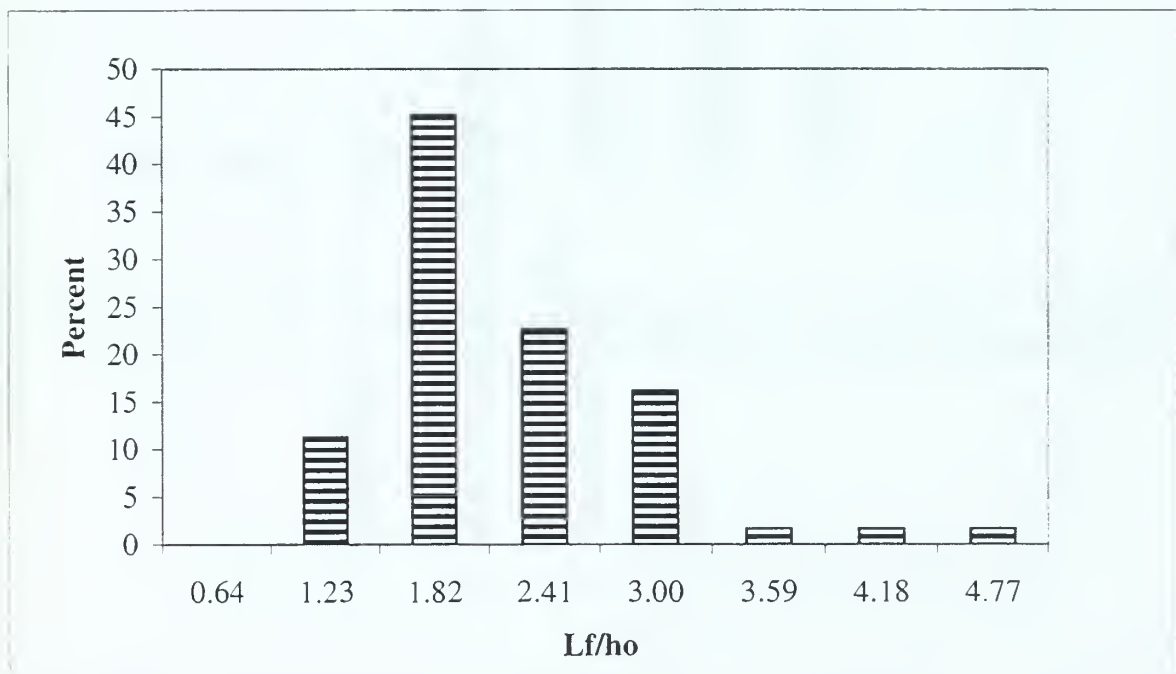


Figure 37. Distribution of the normalized filament length for the axisymmetric jet with roughness ( $k/h_o = 0.02$  ( $h_o = 7.9$  mm,  $Fr = 25.8$ ,  $We = 3014$ )).

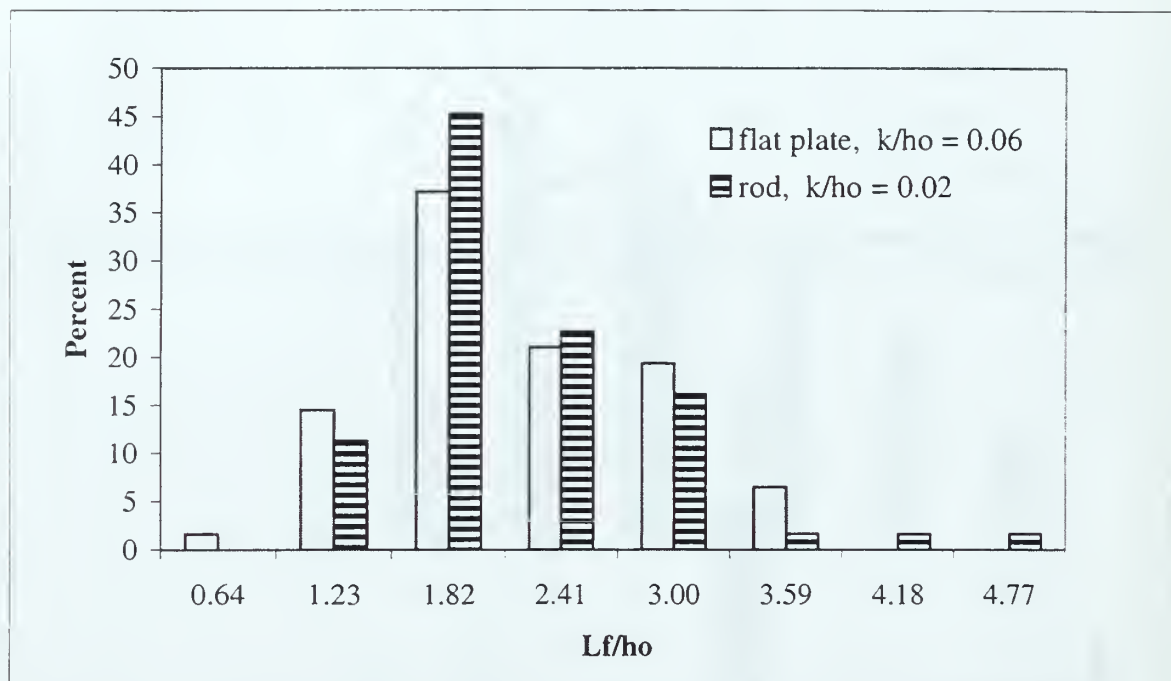


Figure 38. Comparison of the distributions of the normalized filament length for the axisymmetric and wall jet for two relative roughness.

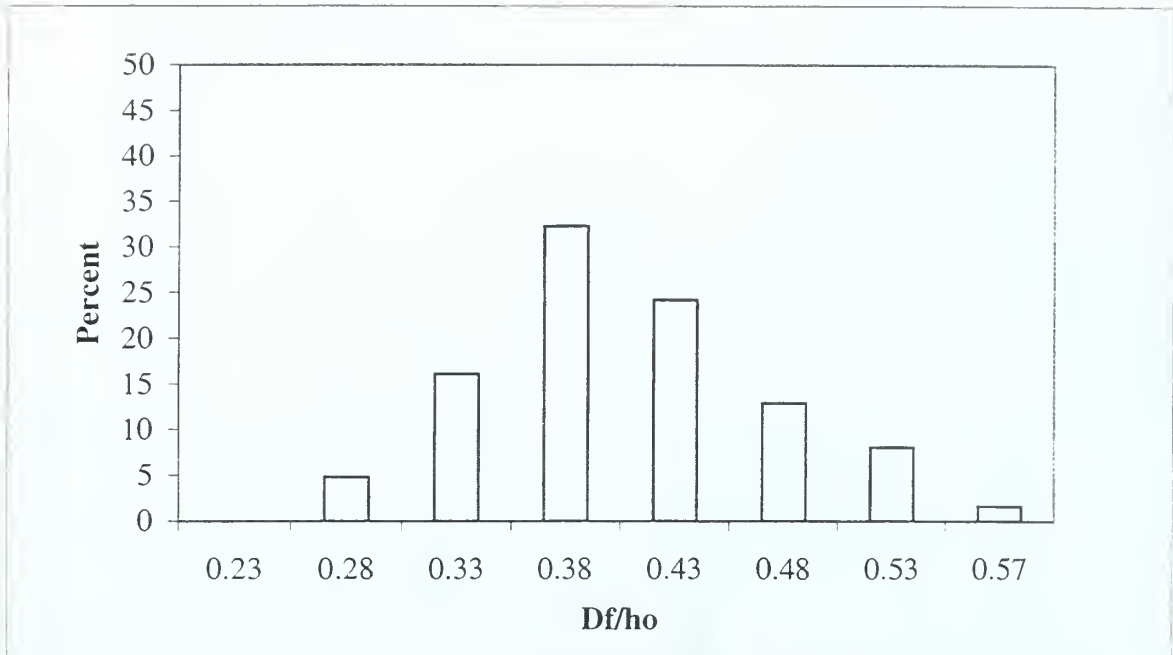


Figure 39. Distribution of the normalized filament diameter for the liquid wall jet with roughness  $(k/h_o) = 0.06$  ( $h_o = 5.8$  mm,  $Fr = 25.8$ ,  $We = 3014$ ).

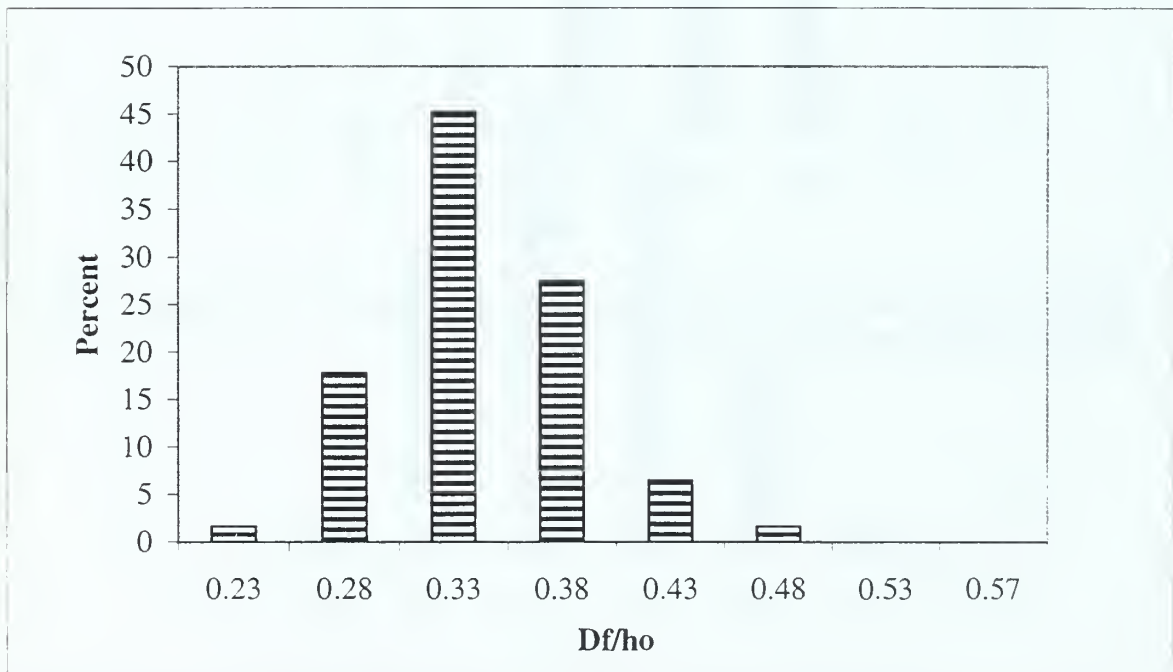


Figure 40. Distribution of the normalized filament diameter for the axisymmetric jet with roughness  $(k/h_o) = 0.02$  ( $h_o = 7.9$  mm,  $Fr = 25.8$ ,  $We = 3014$ ).

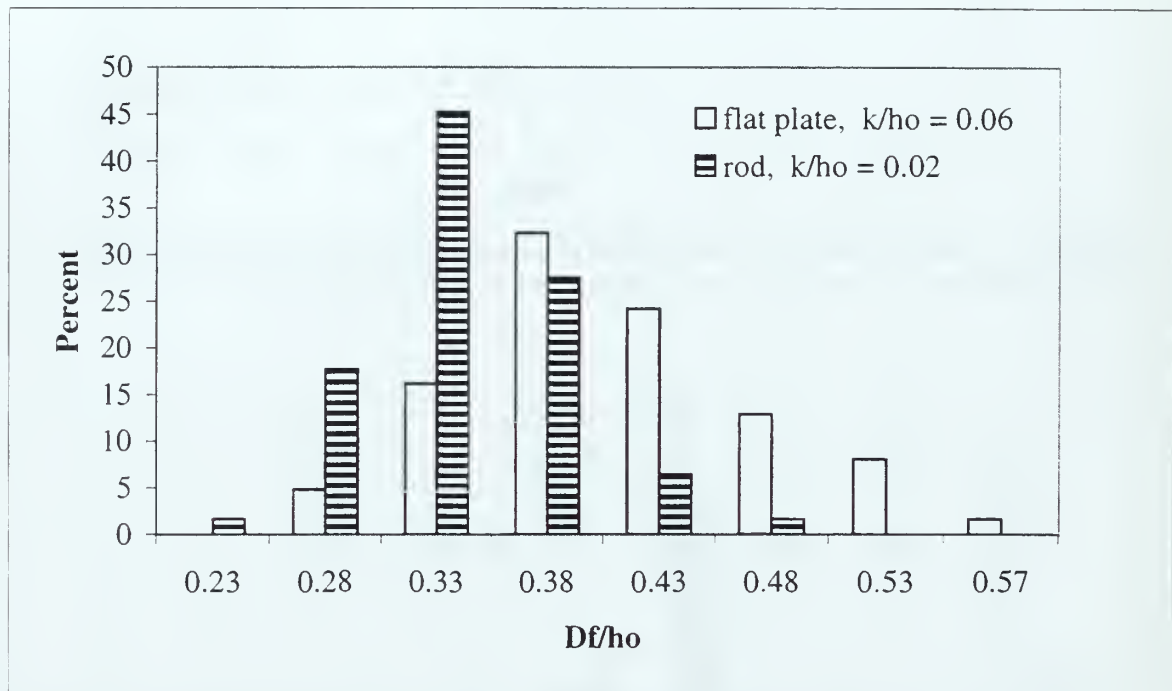


Figure 41. Comparison of the distributions of the normalized filament diameter for the axisymmetric and wall jet for two relative roughness.

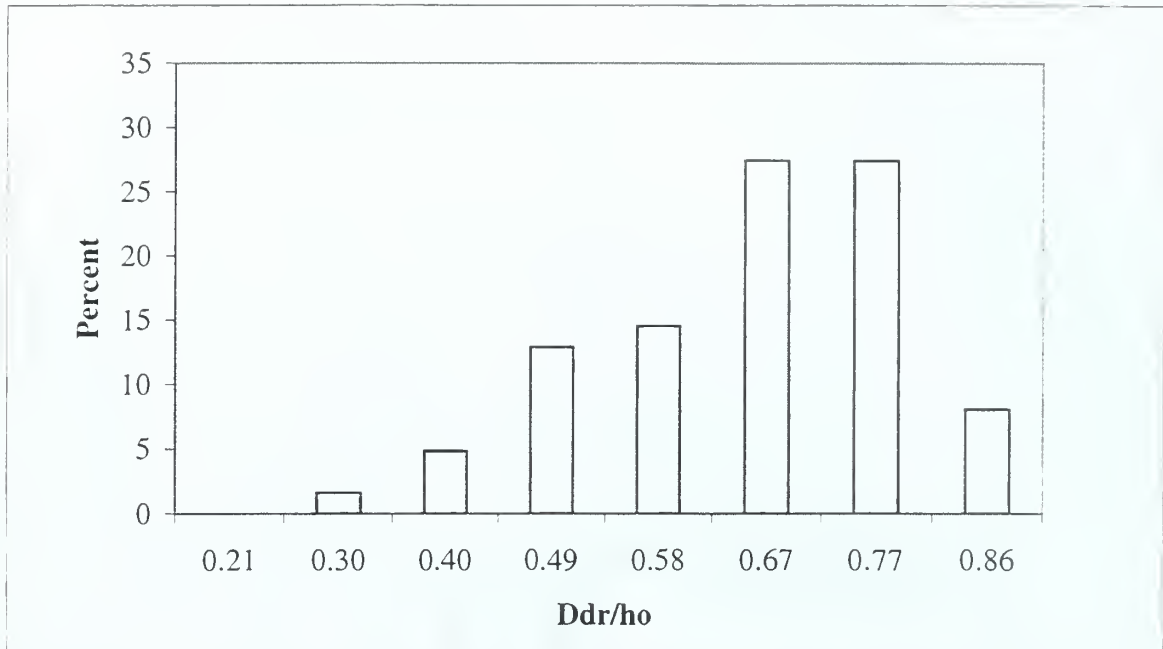


Figure 42. Distribution of the normalized drop diameter for the liquid wall jet with roughness  $(k/h_o) = 0.06$  ( $h_o = 5.8$  mm,  $Fr = 25.8$ ,  $We = 3014$ ).

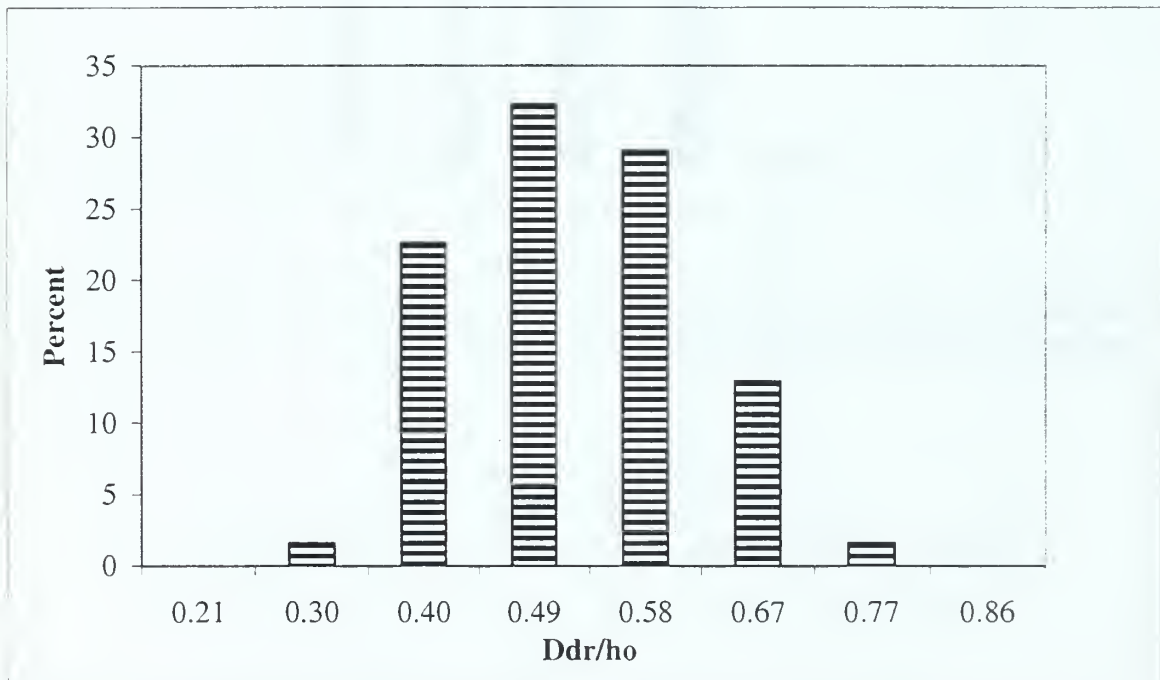


Figure 43. Distribution of the normalized drop diameter for the axisymmetric jet with roughness  $(k/h_o) = 0.02$  ( $h_o = 7.9$  mm,  $Fr = 25.8$ ,  $We = 3014$ ).



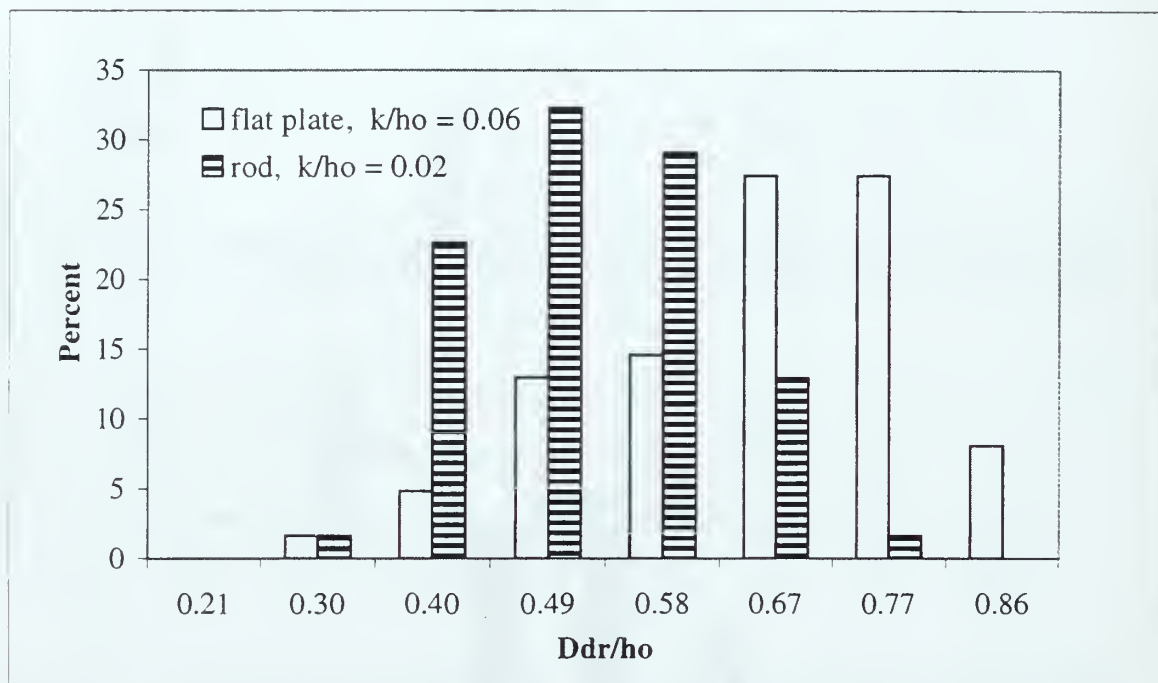


Figure 44. Comparison of the distributions of the normalized drop diameter for the axisymmetric and wall jet for two relative roughness.

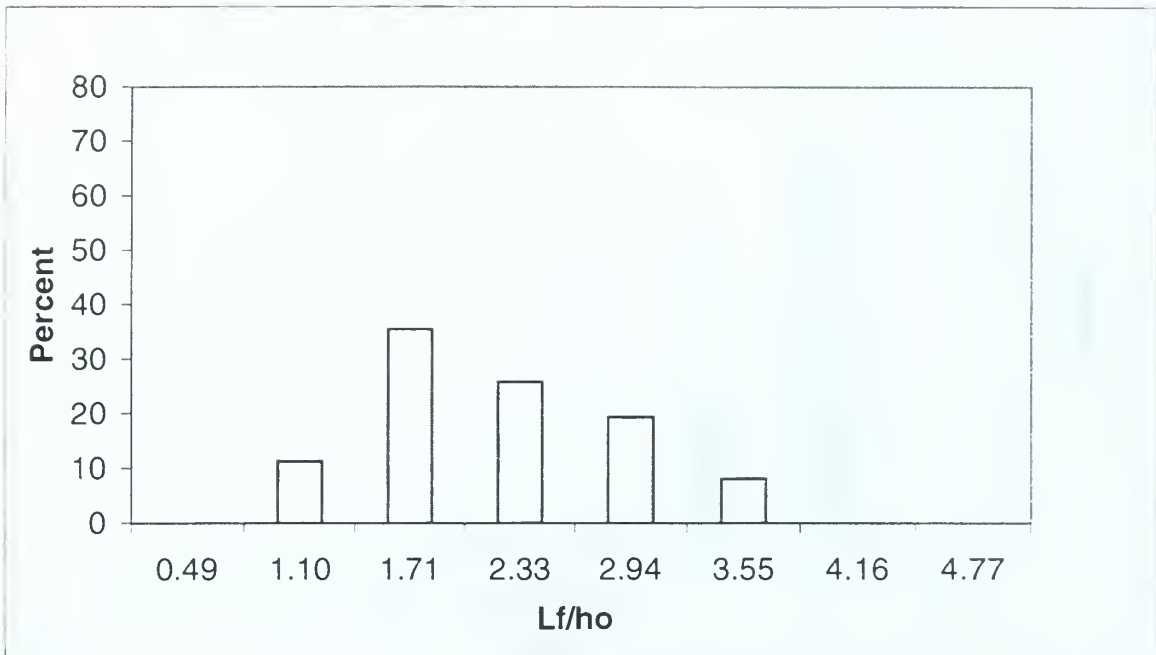


Figure 45. Distributions of normalized filament length for liquid wall jet with jet thickness = 5.8 mm ( $k/h_o = 0.06$ ,  $Fr = 25.8$ ,  $We = 3014$ ).

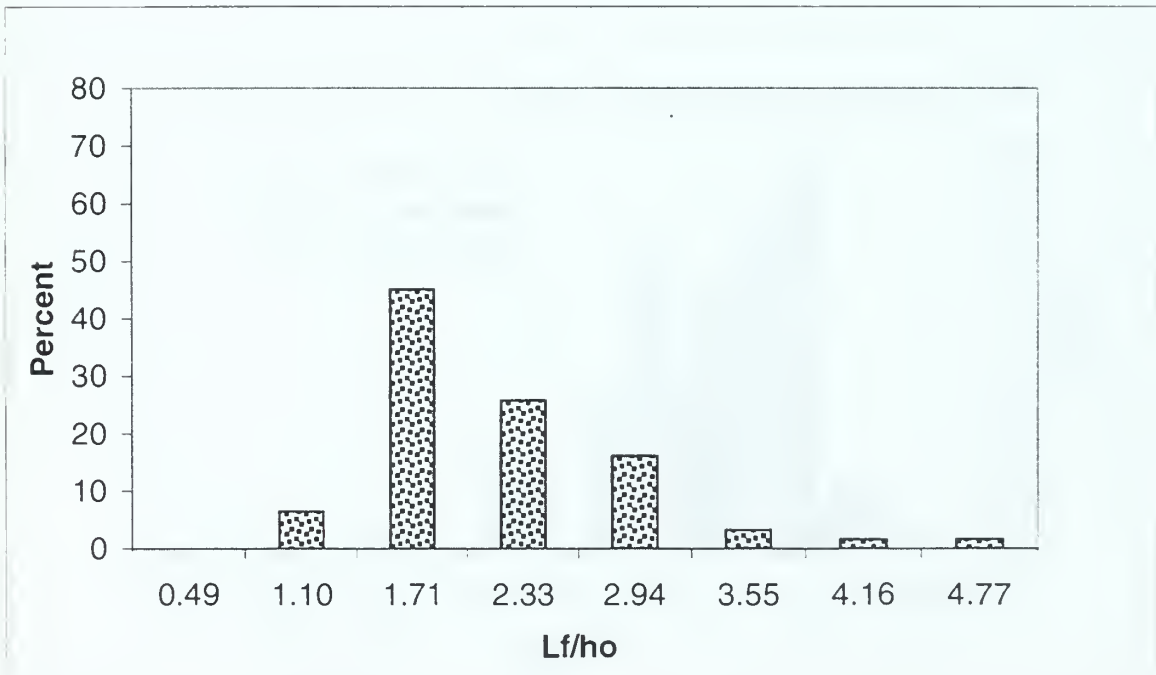


Figure 46. Distributions of normalized filament length for axisymmetric jet with jet thickness = 7.9 mm ( $k/h_o = 0.06$ ,  $Fr = 25.8$ ,  $We = 3014$ ).

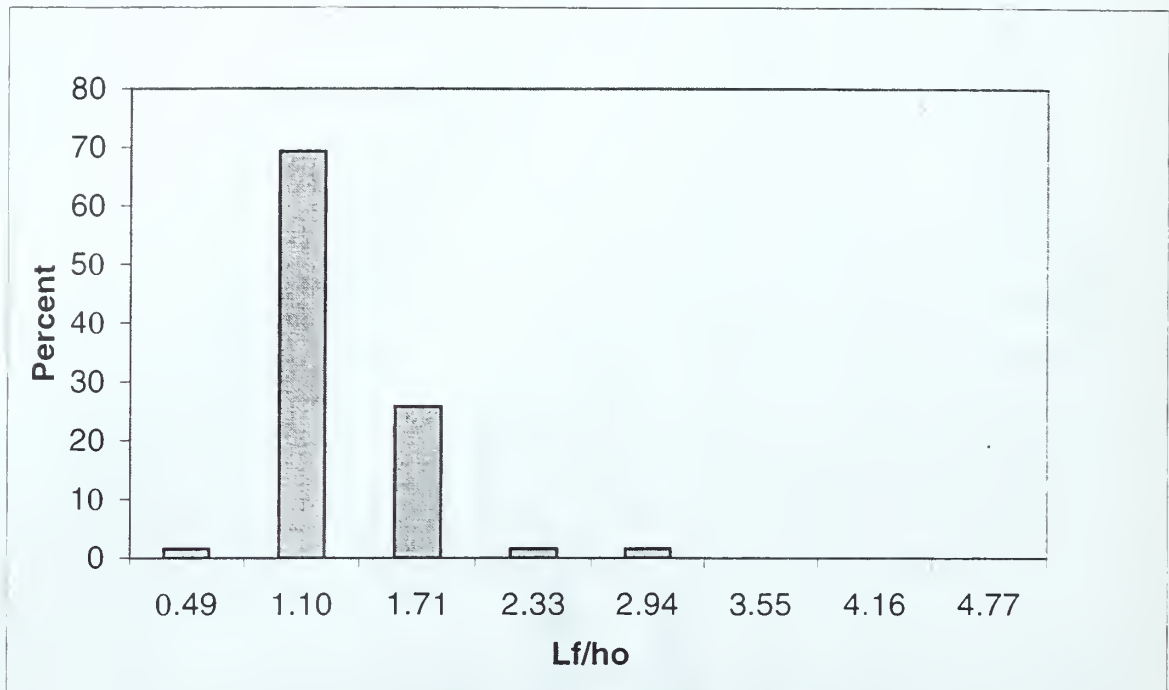


Figure 47. Distributions of normalized filament length for liquid wall jet with jet thickness = 14 mm ( $k/h_o = 0.06$ ,  $Fr = 16.6$ ,  $We = 7367$ ).

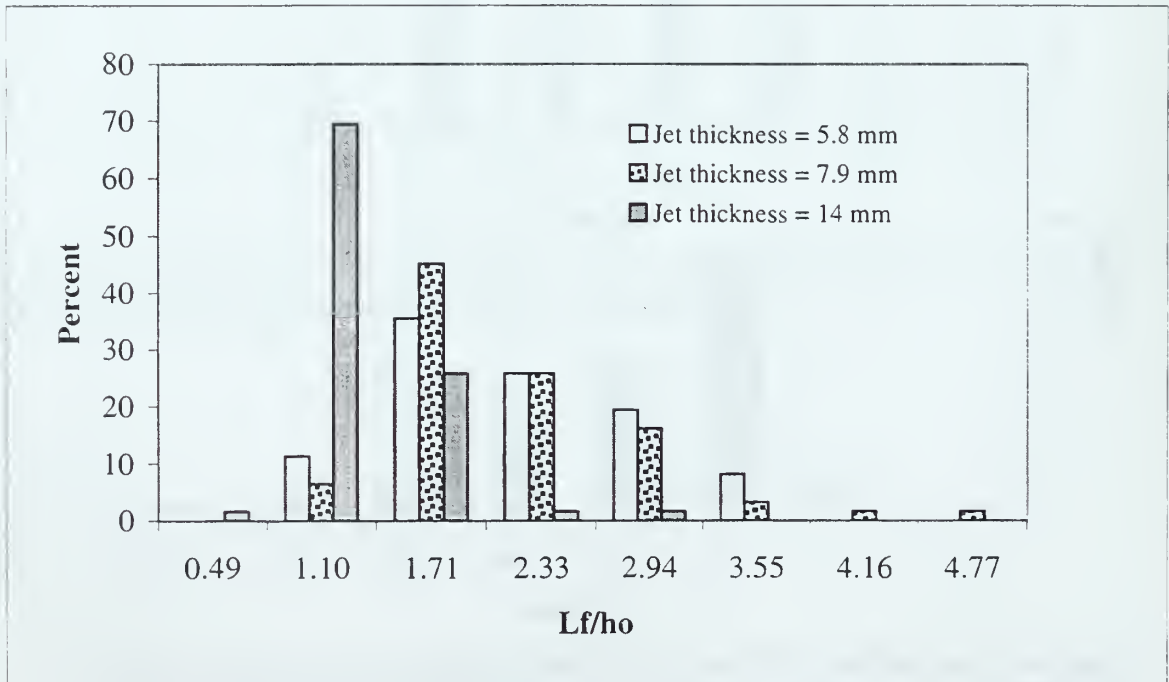


Figure 48. Comparison of the distributions of normalized filament length for liquid jets for three jet thicknesses.

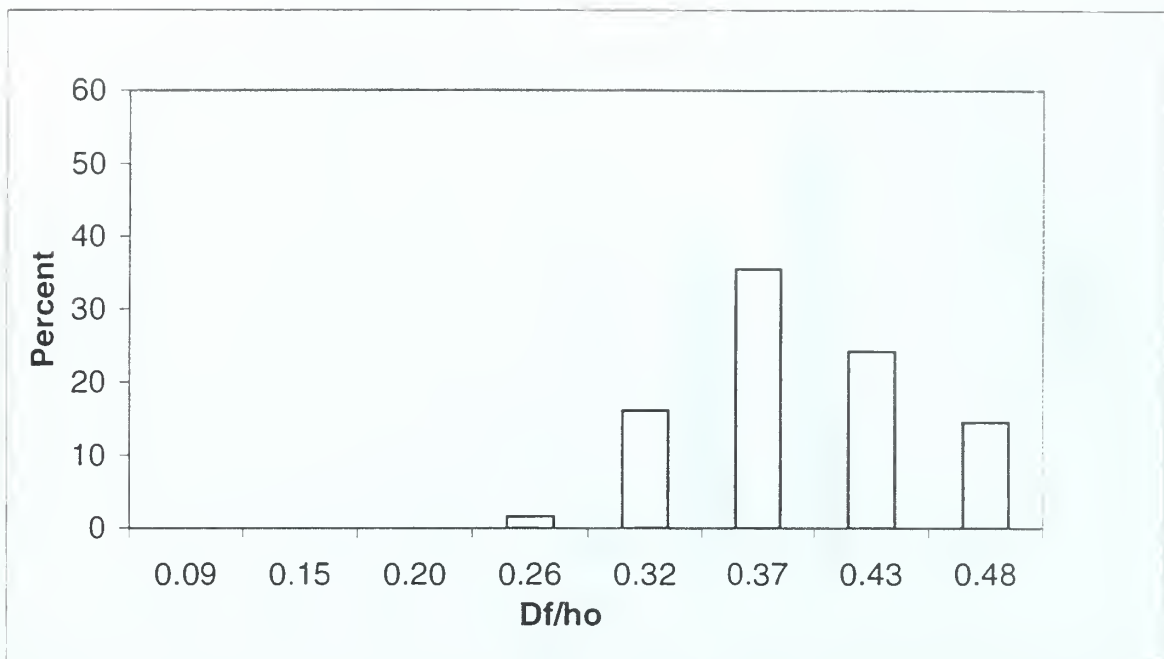


Figure 49. Distributions of normalized filament diameter for liquid wall jet with jet thickness = 5.8 mm ( $k/h_o = 0.06$ ,  $Fr = 25.8$ ,  $We = 3014$ ).

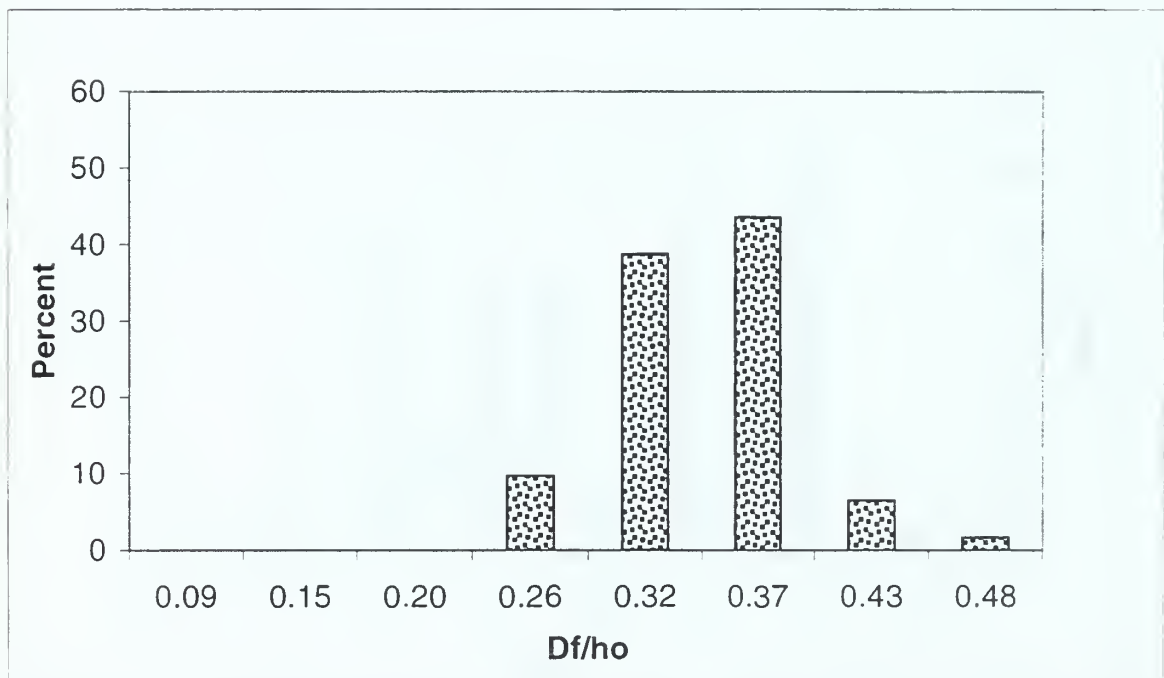


Figure 50. Distributions of normalized filament diameter for axisymmetric jet with jet thickness = 7.9 mm ( $k/h_o = 0.06$ ,  $Fr = 25.8$ ,  $We = 3014$ ).

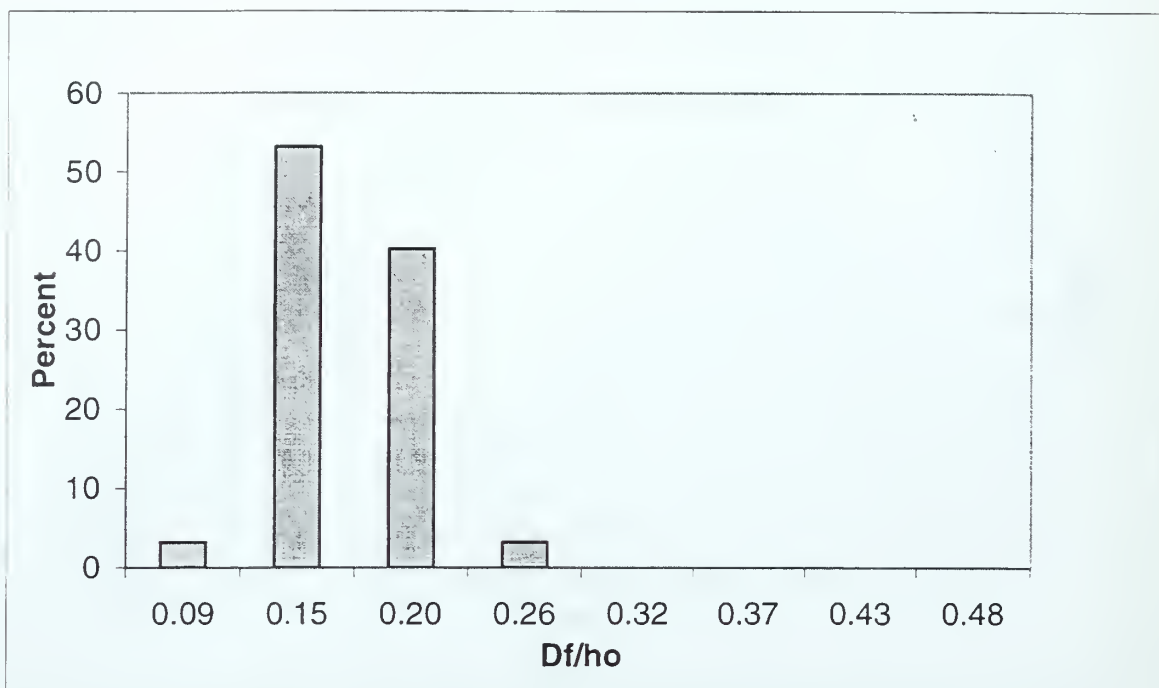


Figure 51. Distributions of normalized filament diameter for liquid wall jet with jet thickness = 14 mm ( $k/h_o = 0.06$ ,  $Fr = 16.6$ ,  $We = 7367$ ).

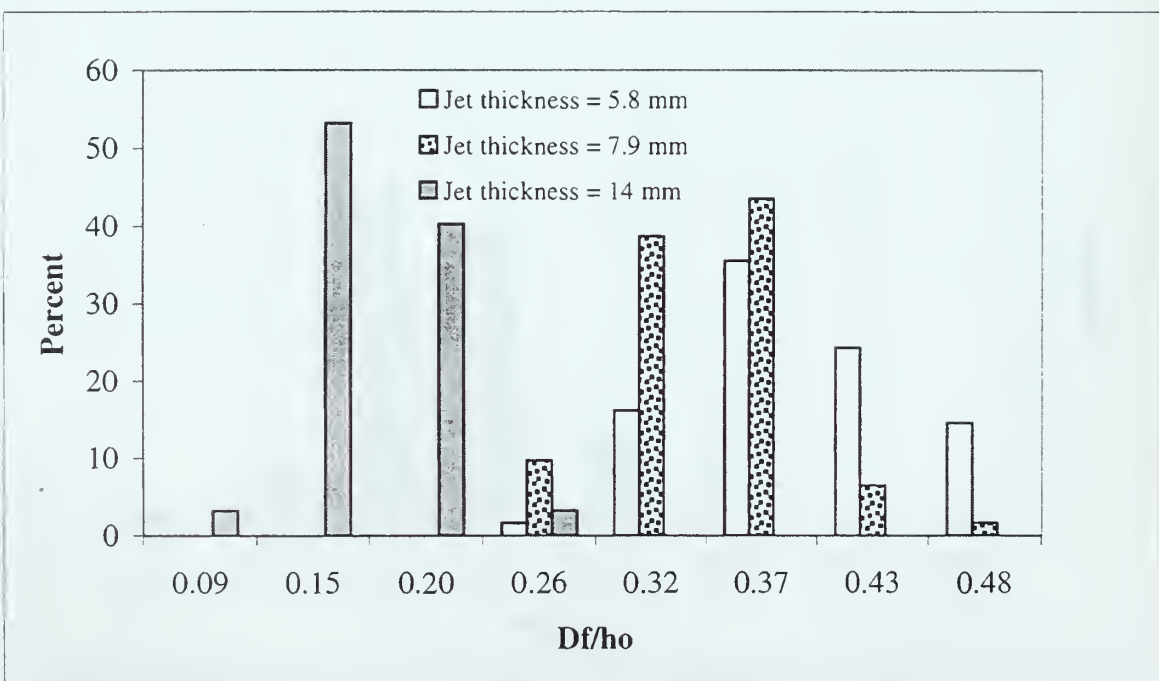


Figure 52. Comparison of the distributions of normalized filament length for liquid jets for three jet thicknesses.

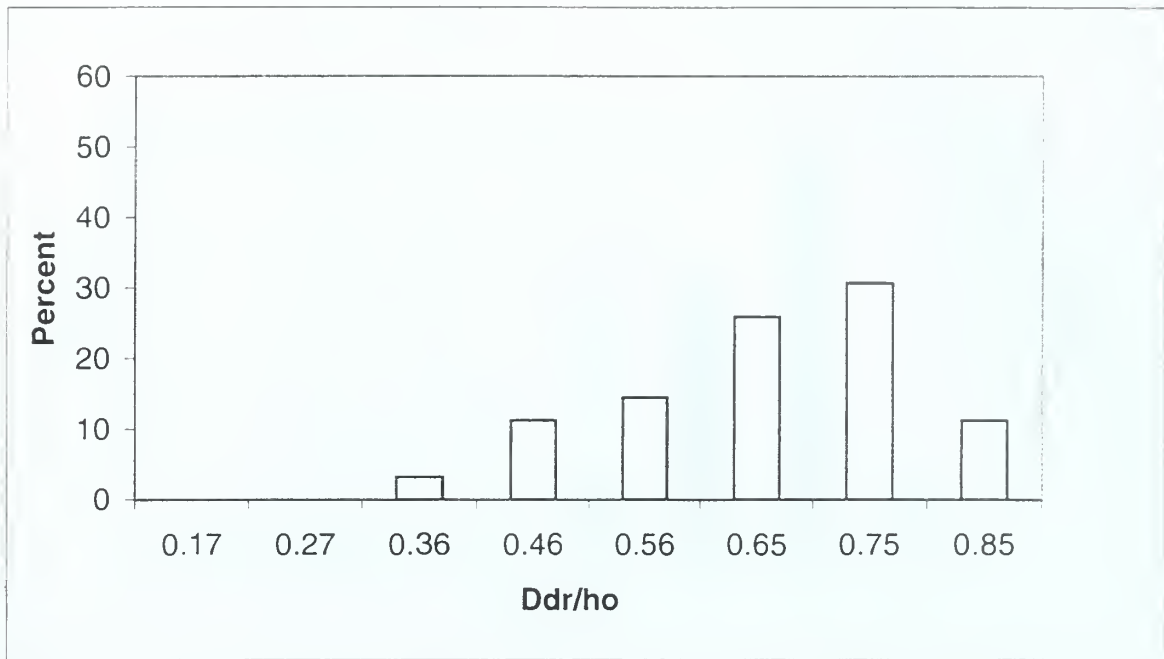


Figure 53. Distributions of normalized drop diameter for liquid wall jet with jet thickness = 5.8 mm ( $k/h_o = 0.06$ ,  $Fr = 25.8$ ,  $We = 3014$ ).

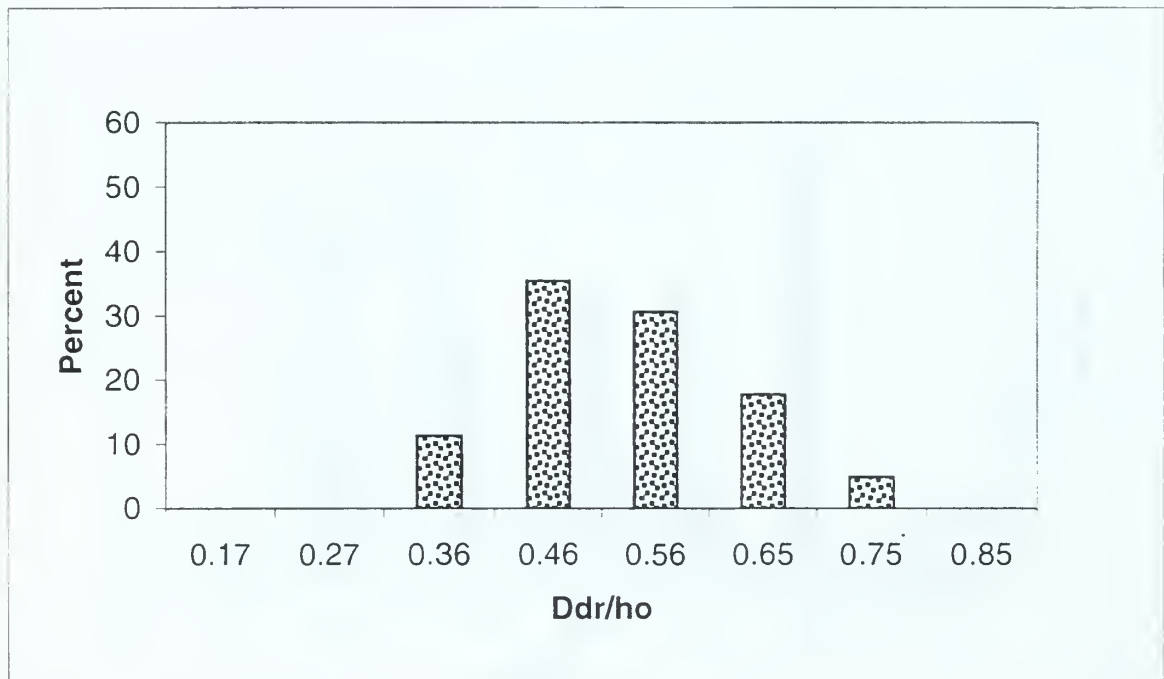


Figure 54. Distributions of normalized drop diameter for axisymmetric jet with jet thickness = 7.9 mm ( $k/h_o = 0.06$ ,  $Fr = 25.8$ ,  $We = 3014$ ).



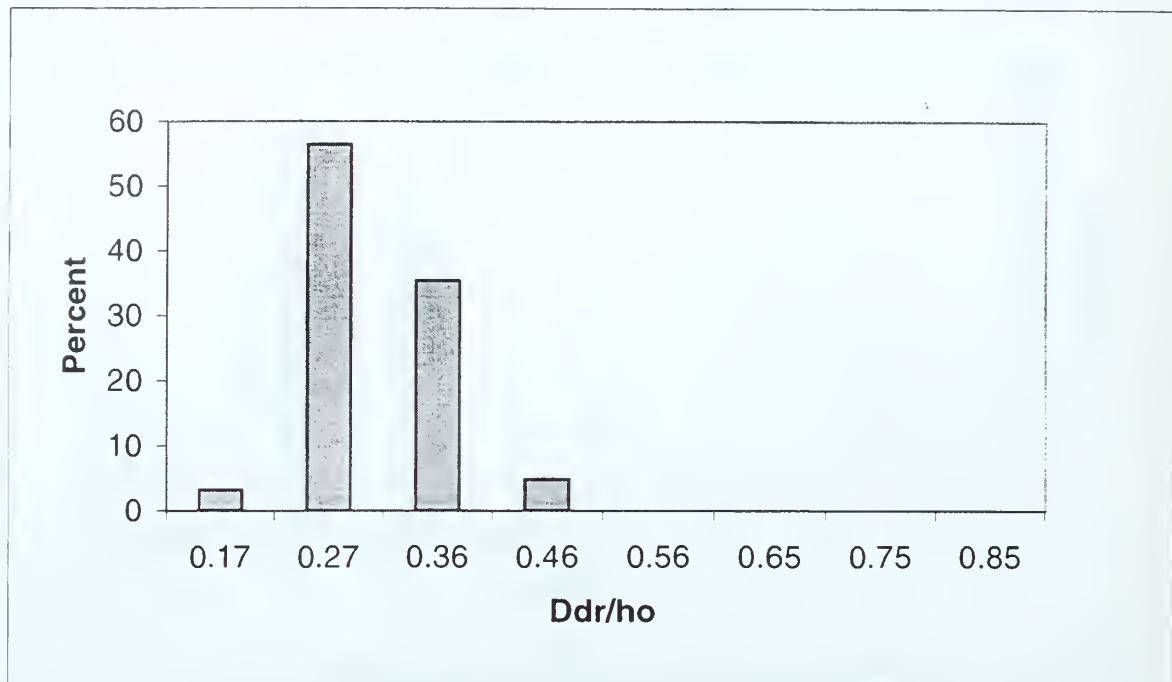


Figure 55. Distributions of normalized drop diameter for liquid wall jet with jet thickness = 14 mm ( $k/h_o = 0.06$ ,  $Fr = 16.6$ ,  $We = 7367$ ).

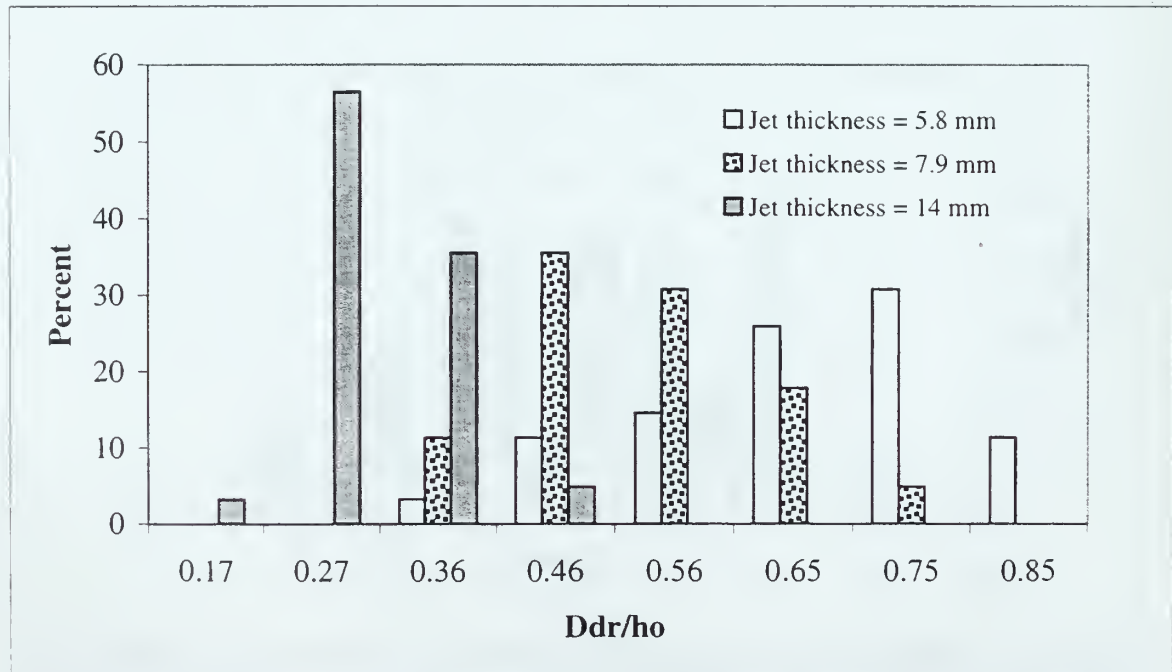


Figure 56. Comparison of the distributions of normalized drop diameter for liquid jets for three jet thicknesses.

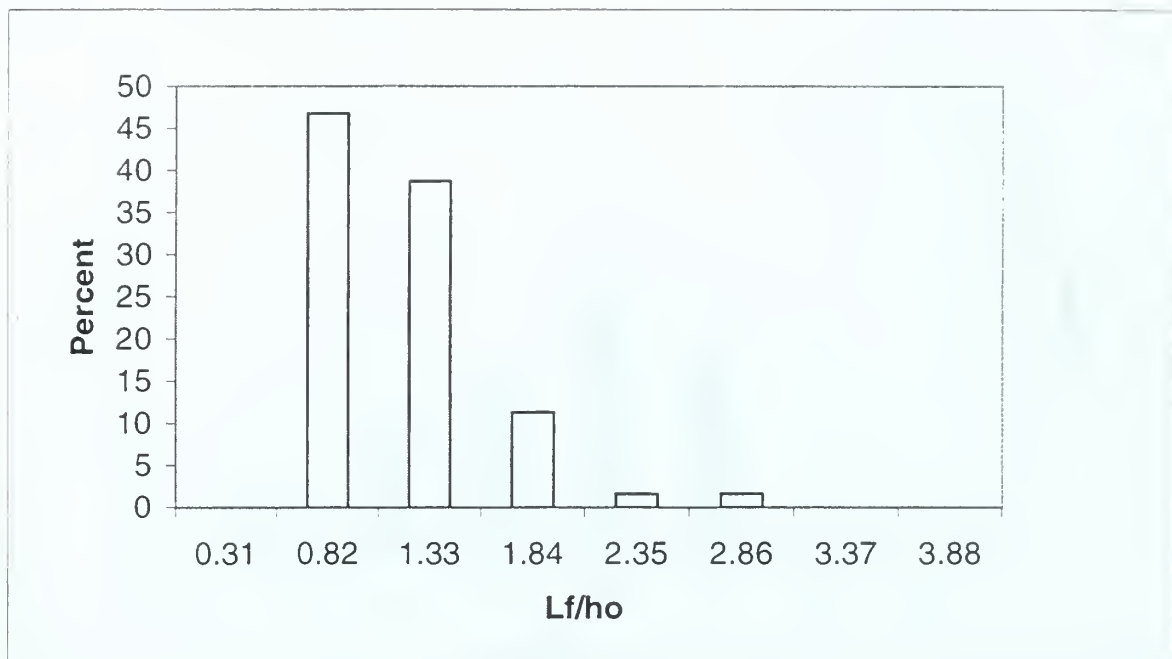


Figure 57. Distributions of normalized filament length for liquid wall jet with medium roughness sand and  $Fr = 16.6$  ( $k/h_o = 0.06$ ,  $We = 7367$ ).

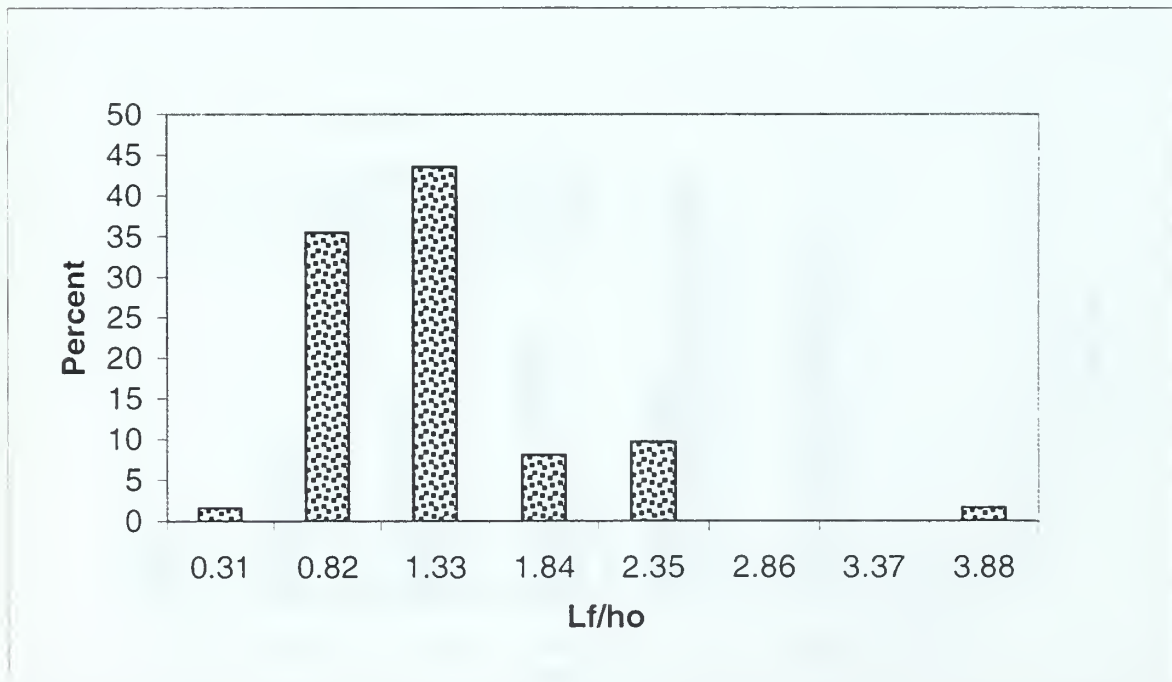


Figure 58. Distributions of normalized filament length for liquid wall jet with medium roughness beads and  $Fr = 16.6$  ( $k/h_o = 0.06$ ,  $We = 7367$ ).

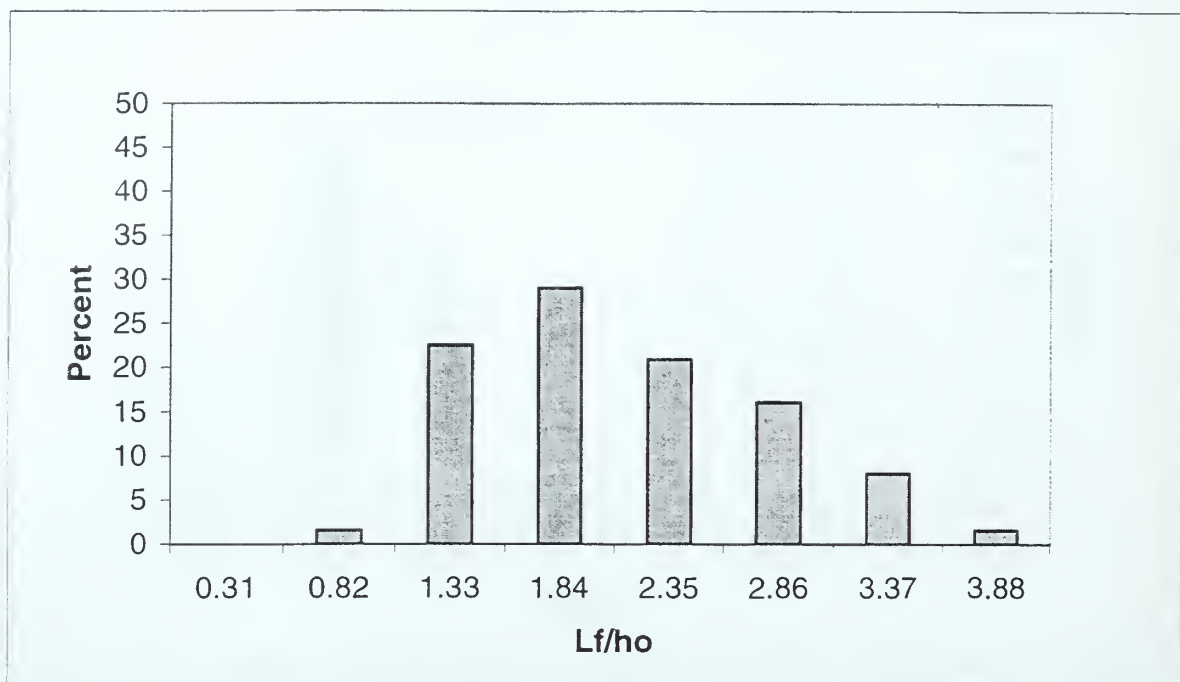


Figure 59. Distributions of normalized filament length for liquid wall jet with medium roughness sand and  $Fr = 25.8$  ( $k/h_o = 0.06$ ,  $We = 3014$ ).

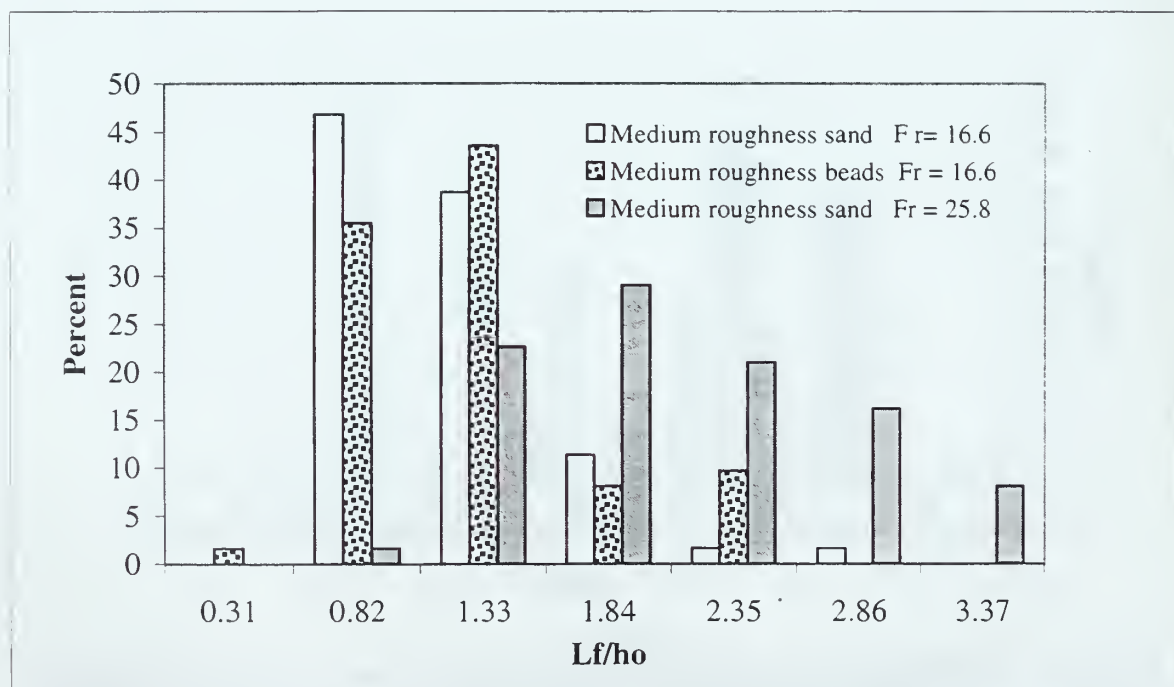


Figure 60. Comparison of the distributions of normalized filament length for liquid wall jets with medium roughness for three Froude numbers.

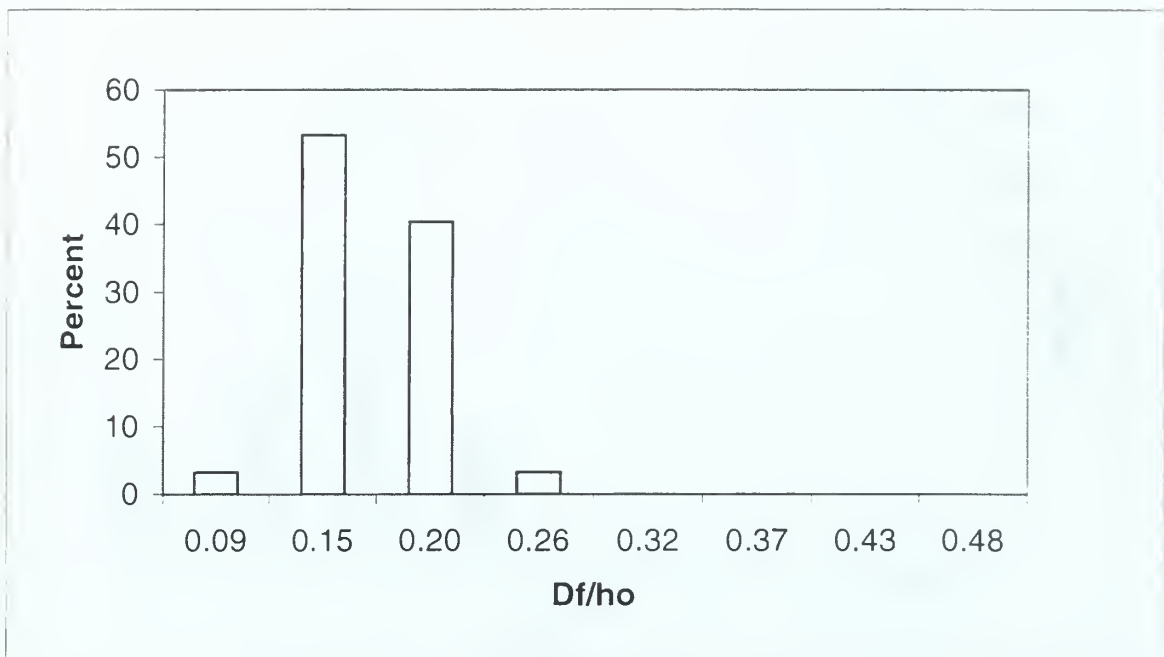


Figure 61. Distributions of normalized filament diameter for liquid wall jet with medium roughness sand and  $Fr = 16.6$  ( $k/h_o = 0.06$ ,  $We = 7367$ ).

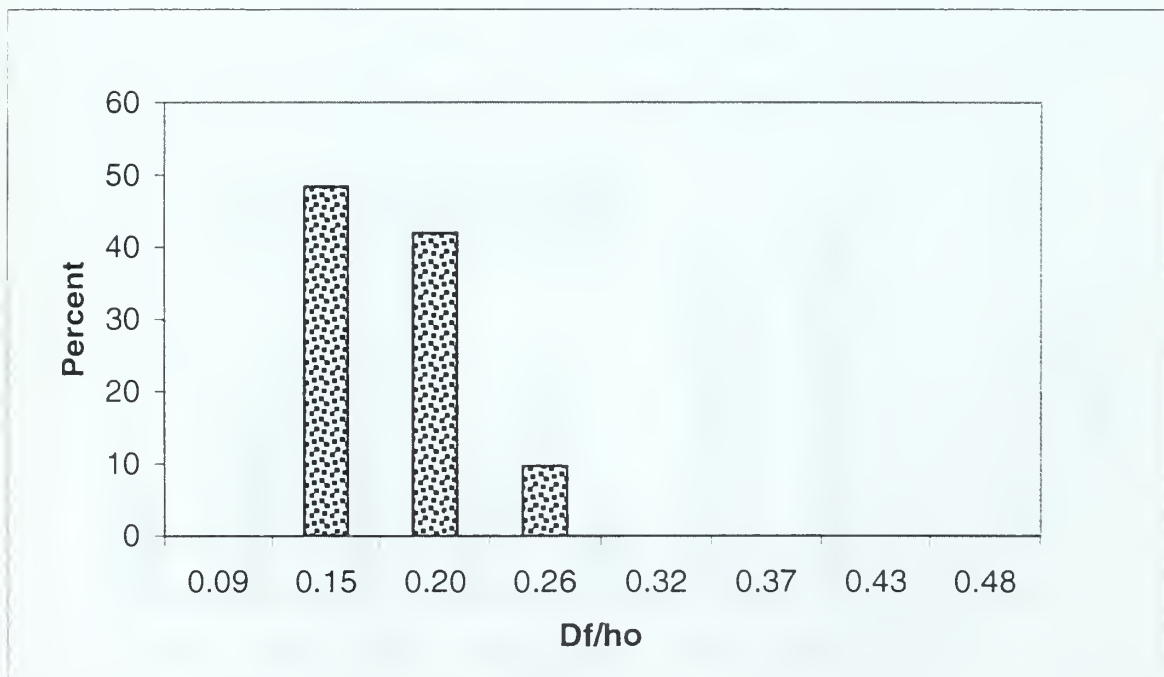


Figure 62. Distributions of normalized filament diameter for liquid wall jet with medium roughness beads and  $Fr = 16.6$  ( $k/h_o = 0.06$ ,  $We = 7367$ ).

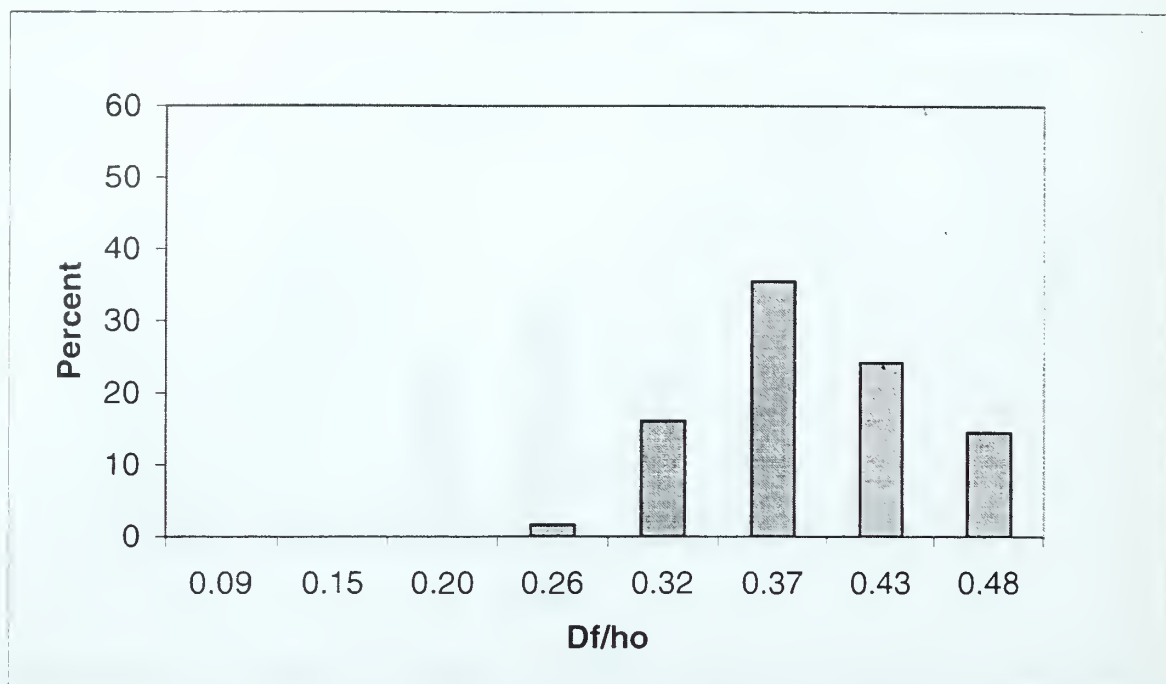


Figure 63. Distributions of normalized filament diameter for liquid wall jet with medium roughness sand and  $Fr = 25.8$  ( $k/ho = 0.06$ ,  $We = 3014$ ).

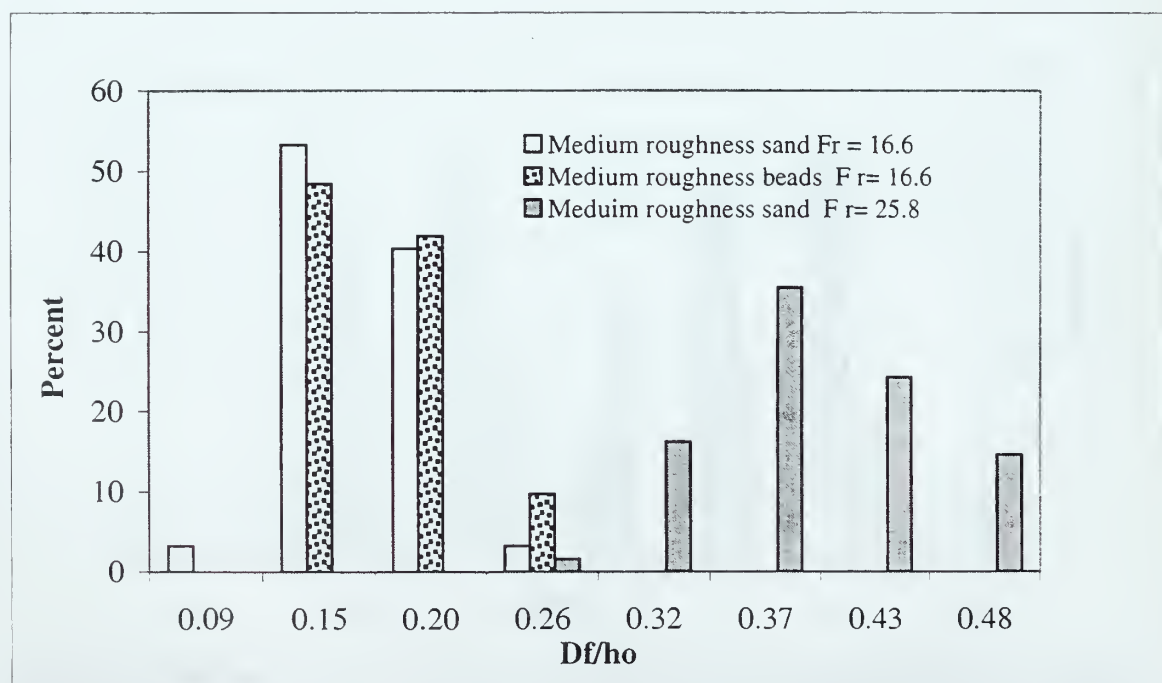


Figure 64. Comparison of the distributions of normalized filament diameter for liquid wall jets with medium roughness for three Froude numbers.

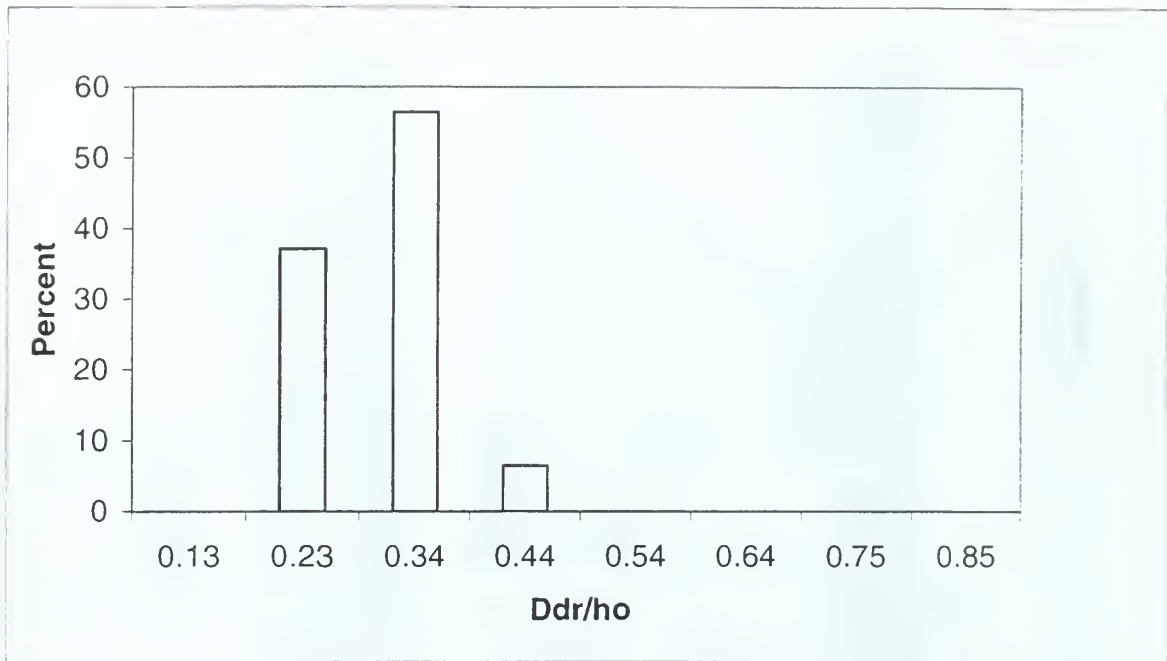


Figure 65. Distributions of normalized drop diameter for liquid wall jet with medium roughness sand and  $Fr = 16.6$  ( $k/h_o = 0.06$ ,  $We = 7367$ ).

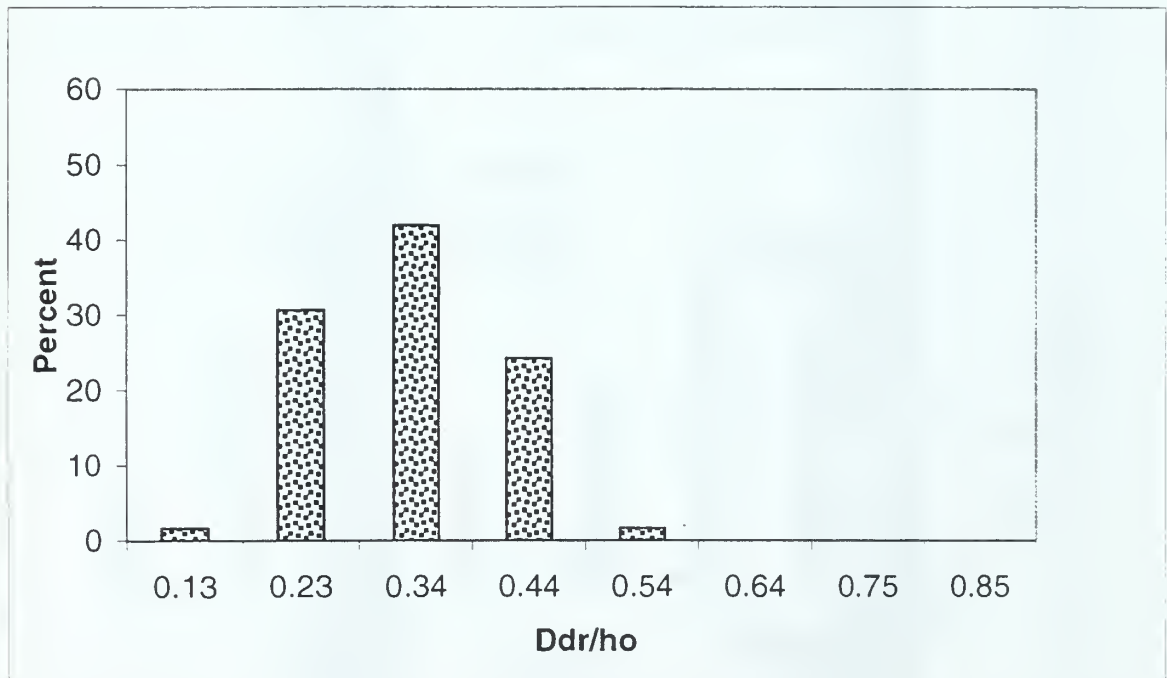


Figure 66. Distributions of normalized drop diameter for liquid wall jet with medium roughness beads and  $Fr = 16.6$  ( $k/h_o = 0.06$ ,  $We = 7367$ ).



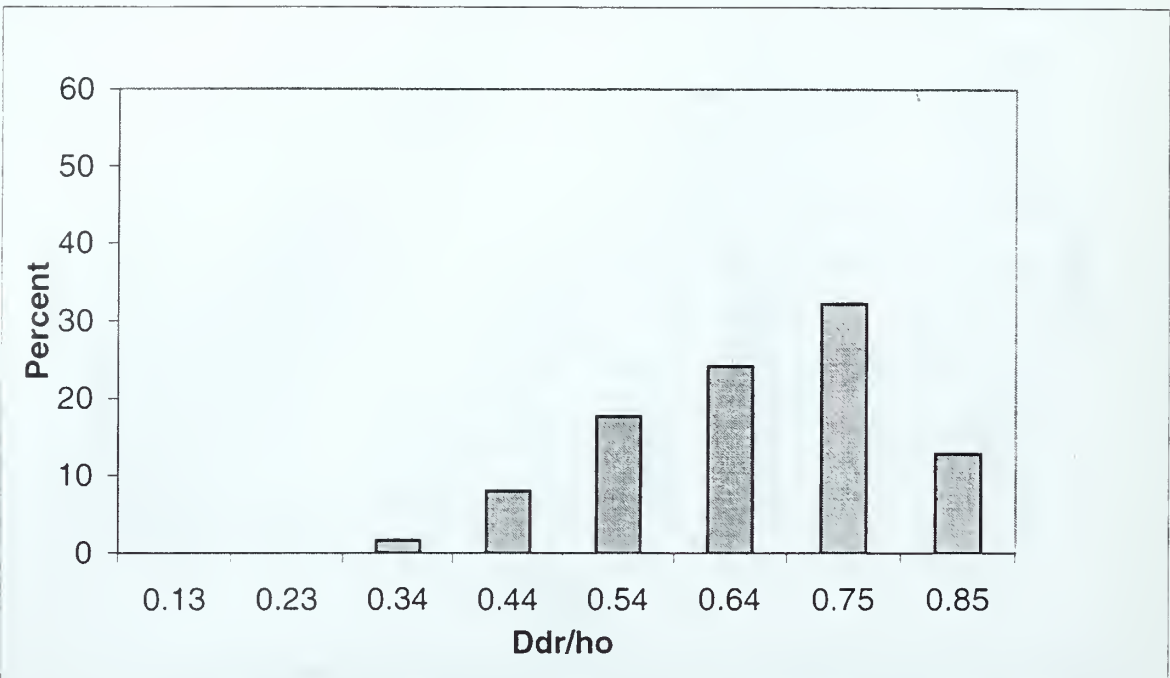


Figure 67. Distributions of normalized drop diameter for liquid wall jet with medium roughness sand and  $Fr = 25.8$  ( $k/ho = 0.06$ ,  $We = 3014$ ).

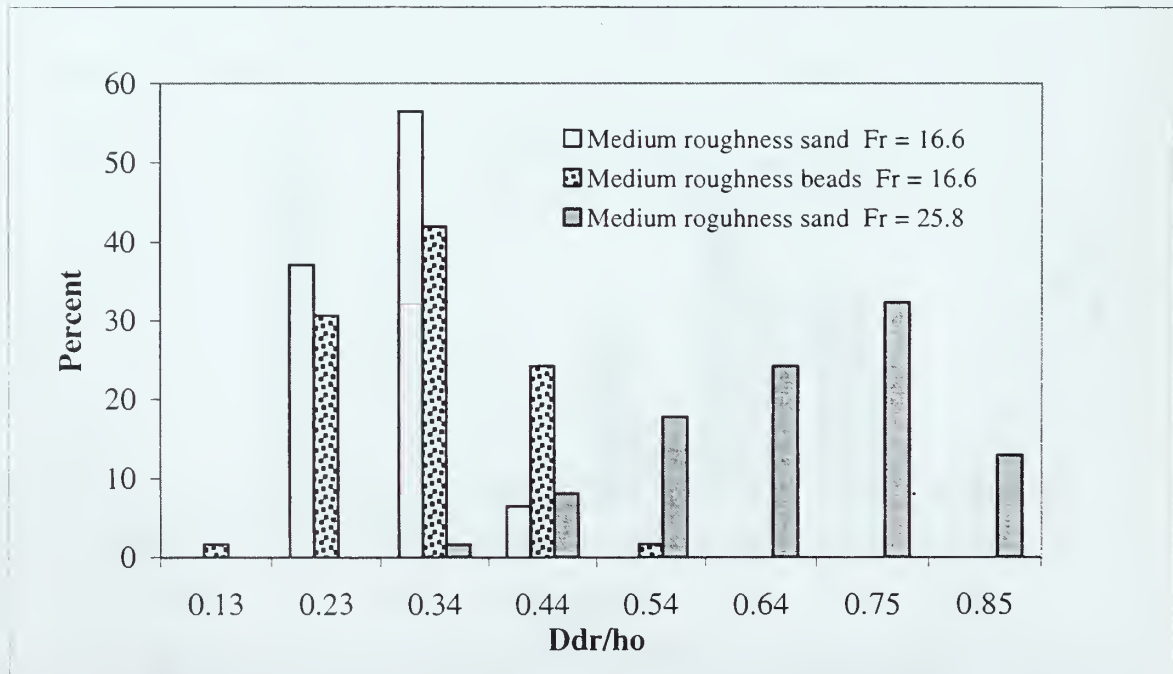


Figure 68. Comparison of the distributions of normalized drop diameter for liquid wall jets with medium roughness for three Froude numbers.

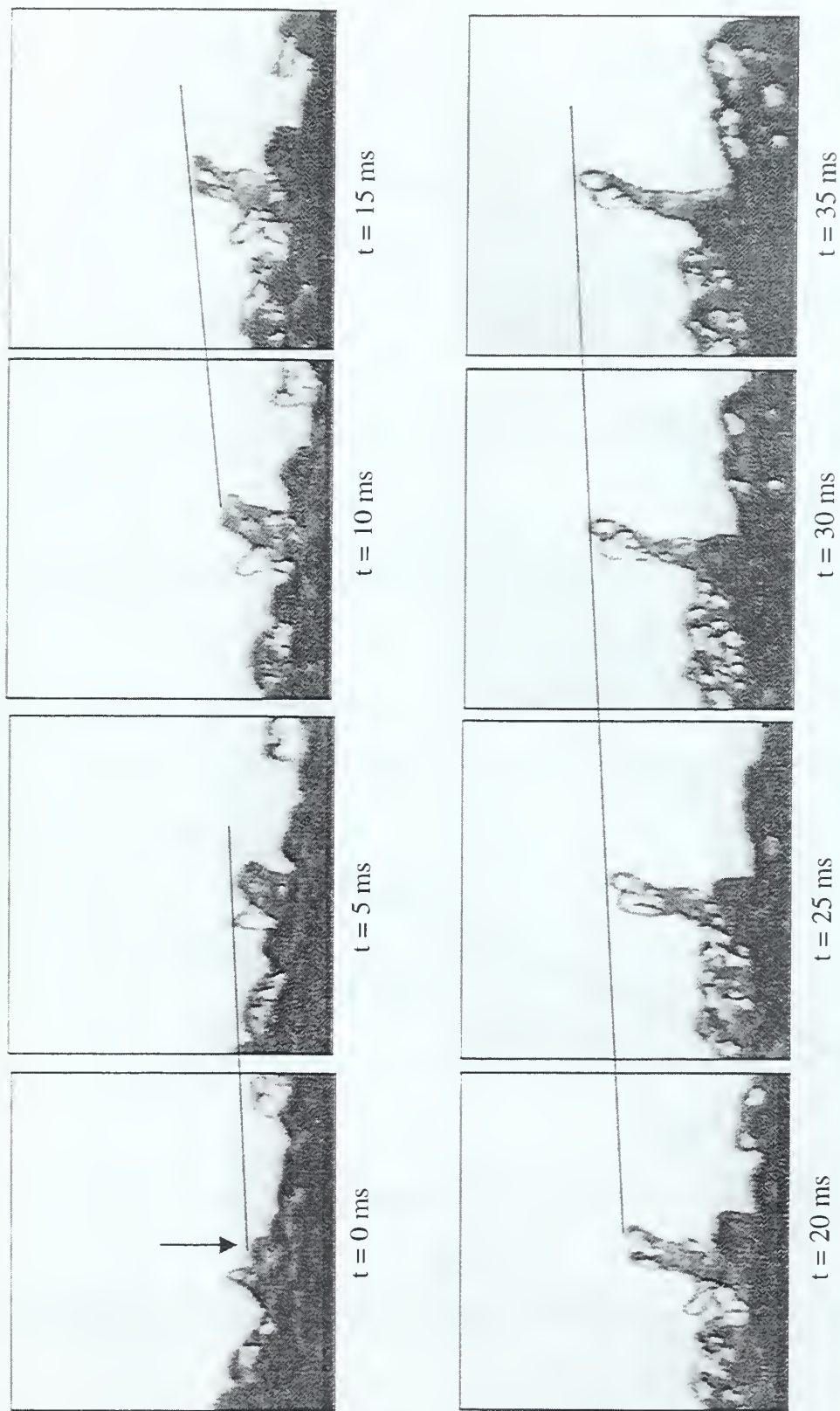


Figure 69. Sequence of images, captured for filament analysis (Case 1), where the ligament is born directly behind another developing ligament, makes an attempt to separate into two, and is nearly normal to the free surface.

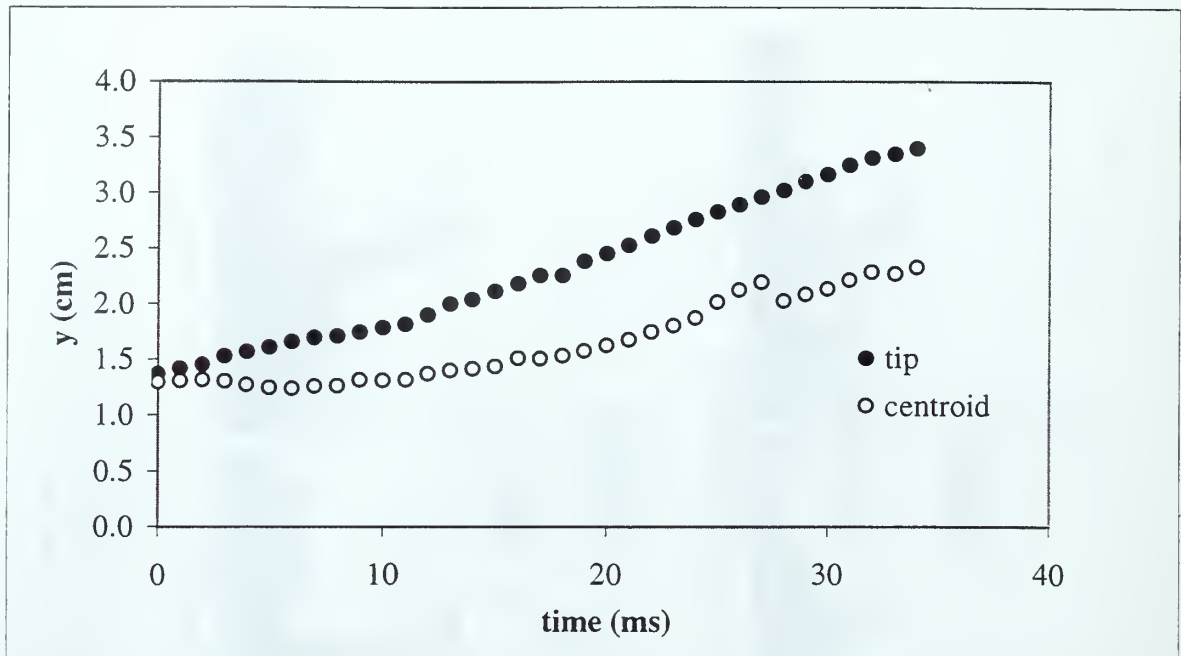


Figure 70a. Y-component of position of the filament tip and centroid as a function of time.

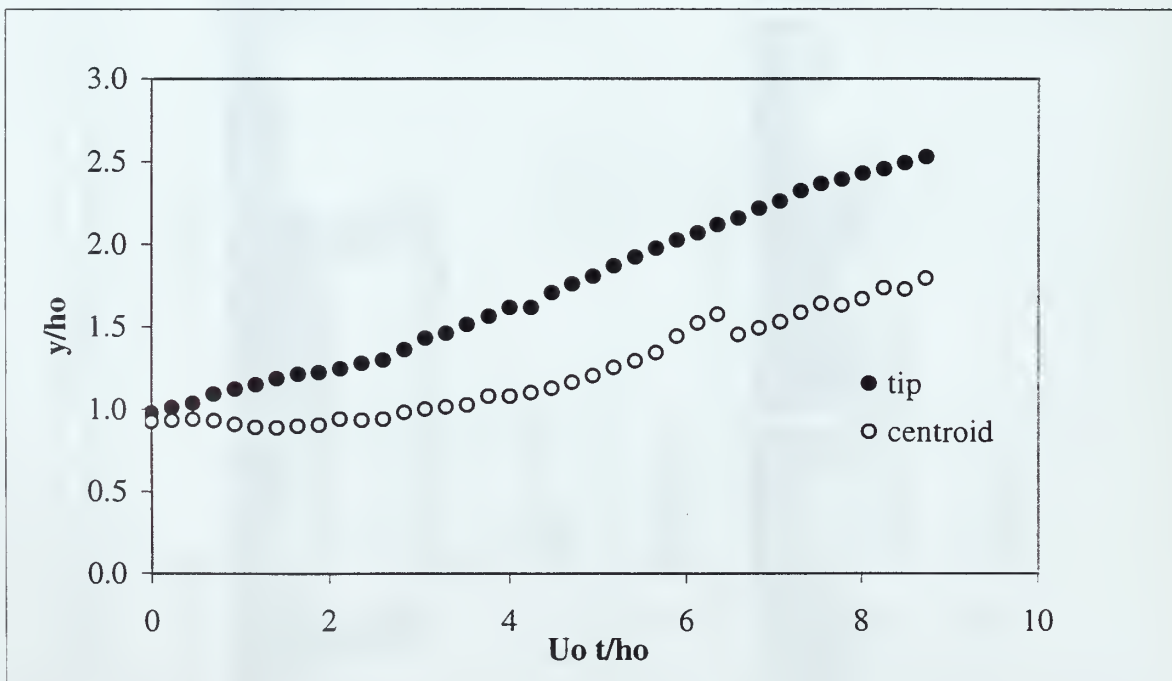


Figure 70b. Normalized y-component of position of the filament tip and centroid as a function of normalized time.



Figure 71. Sequence of images, captured for filament analysis (Case 2), where the ligament is born nearly normal to the free surface, and does not undergo necking within the observation period.



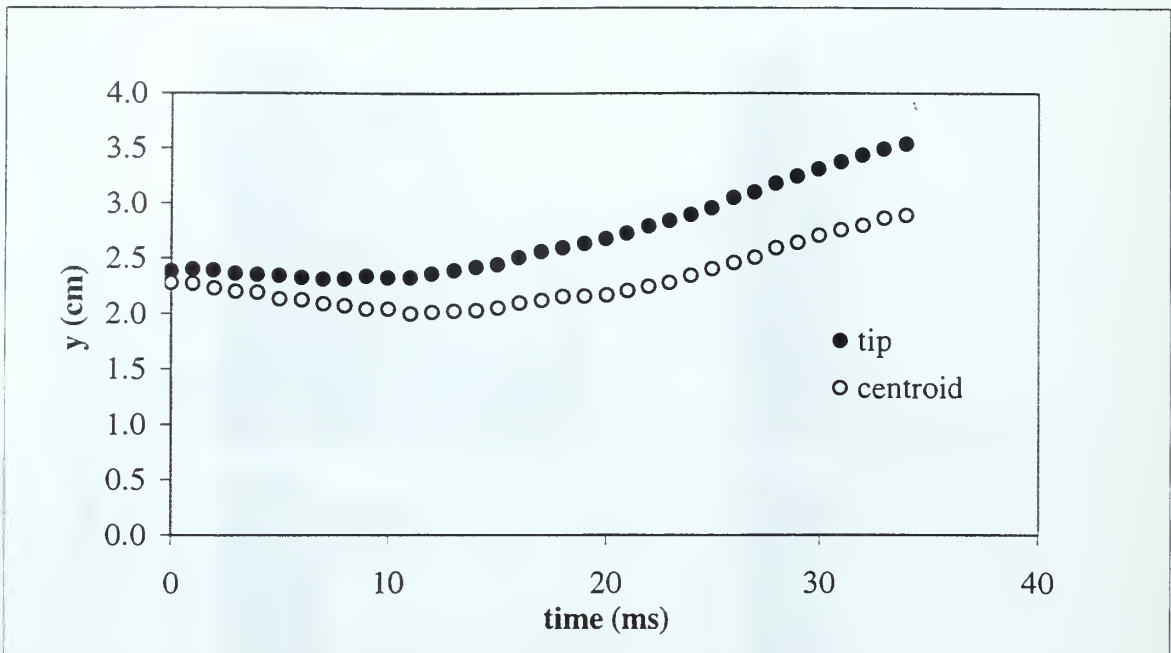


Figure 72a. Y-component of position of the filament tip and centroid as a function of time.

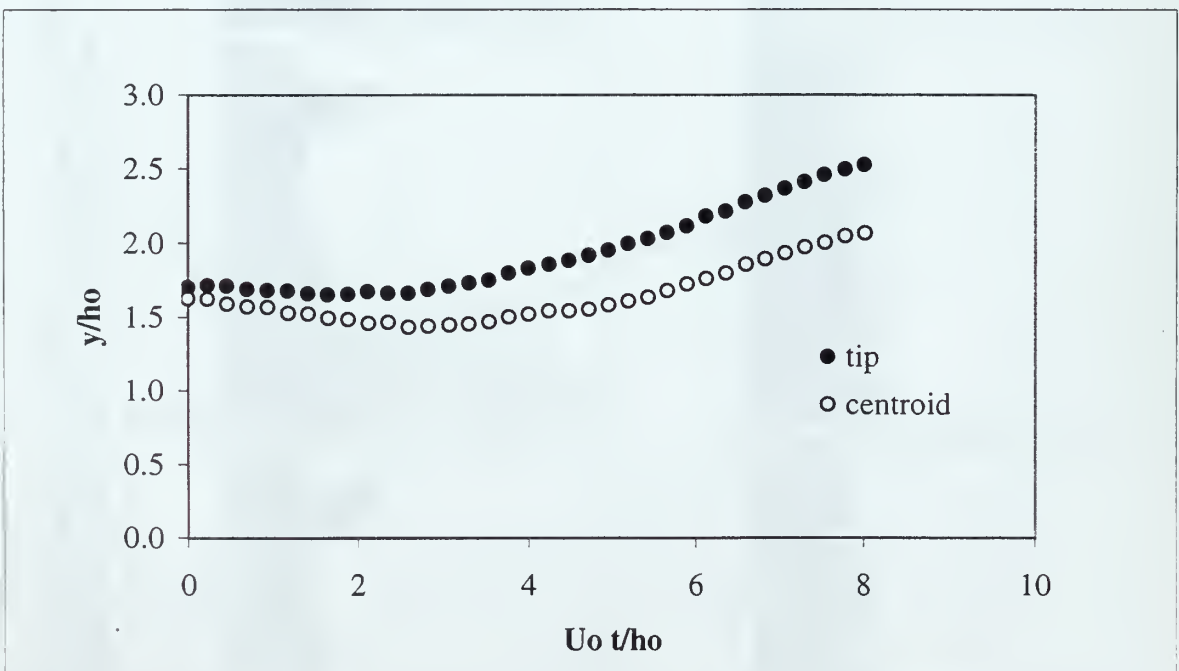


Figure 72b. Normalized y-component of position of the filament tip and centroid as a function of normalized time.

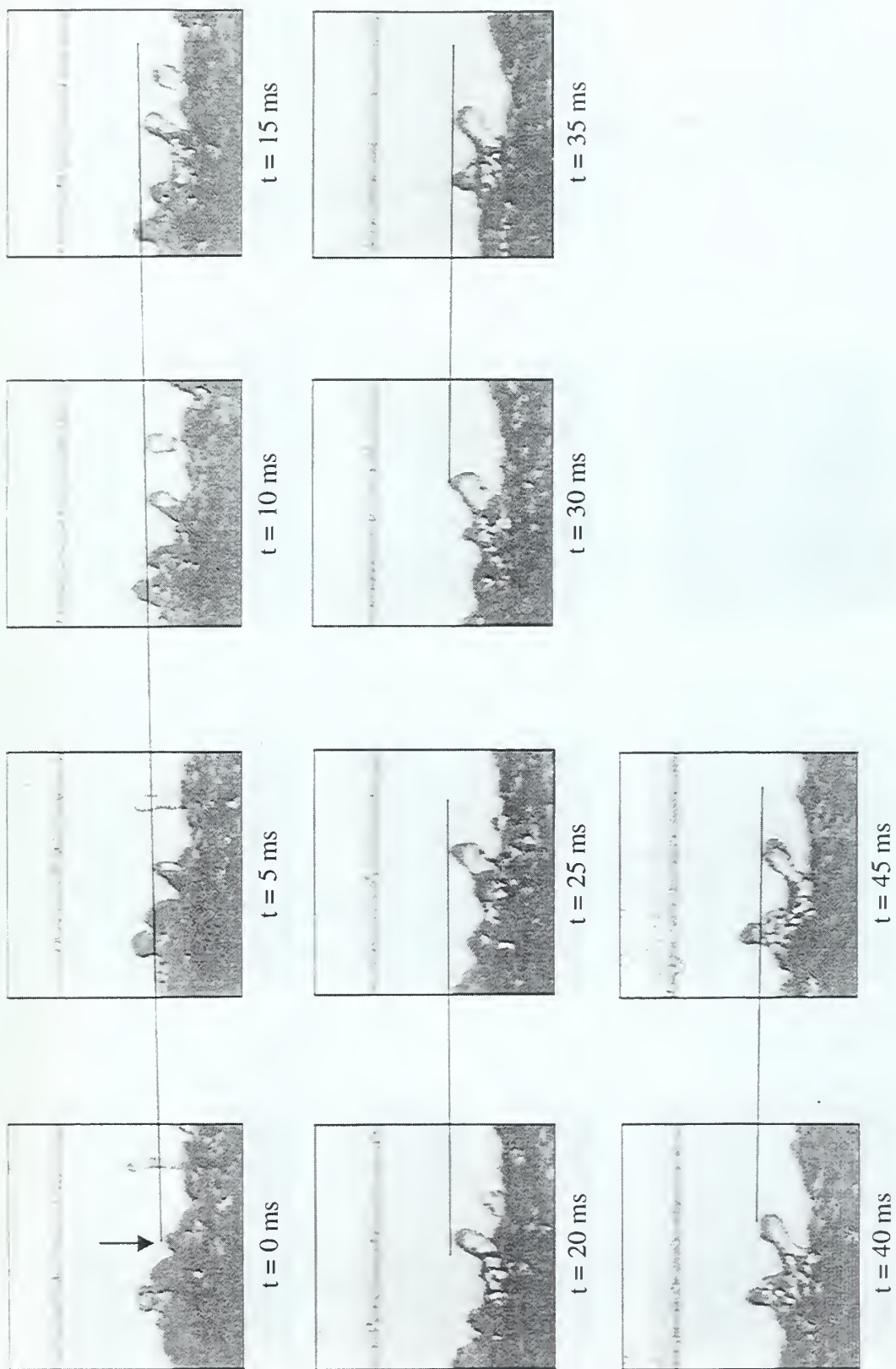


Figure 73. Sequence of images, captured for the filament analysis (Case 3), where the ligament is born amidst a "forest" of ligaments, leans backwards, starts to neck but not sufficiently to produce a droplet.



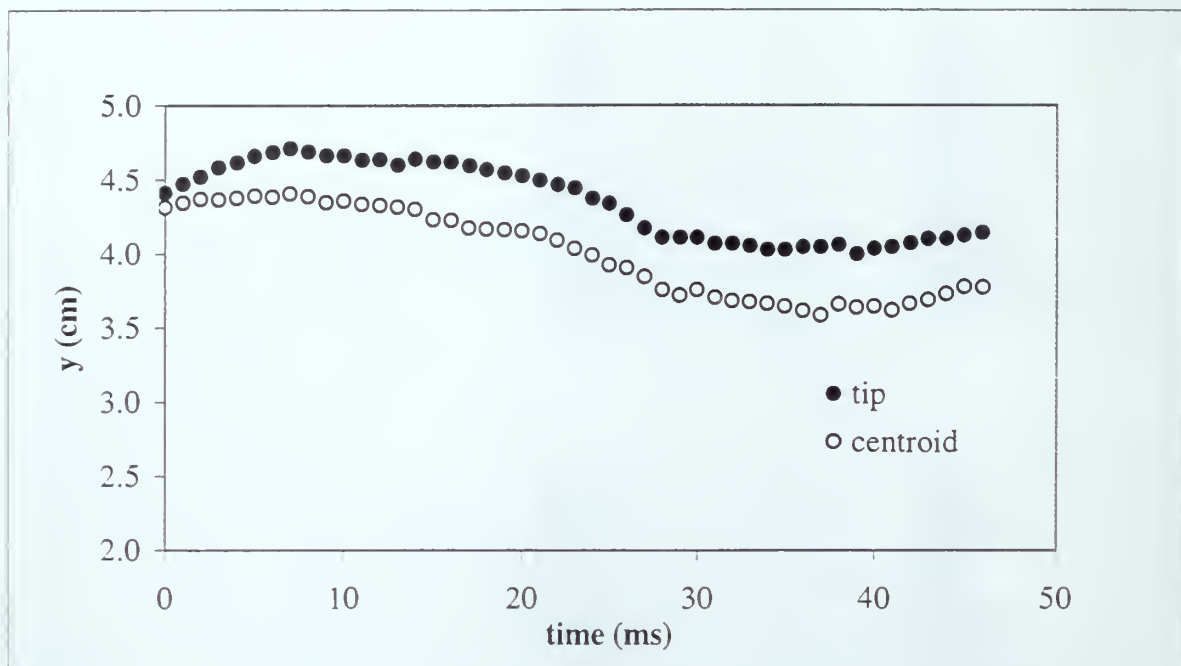


Figure 74a. Y-component of position of the filament tip and centroid as a function of time.

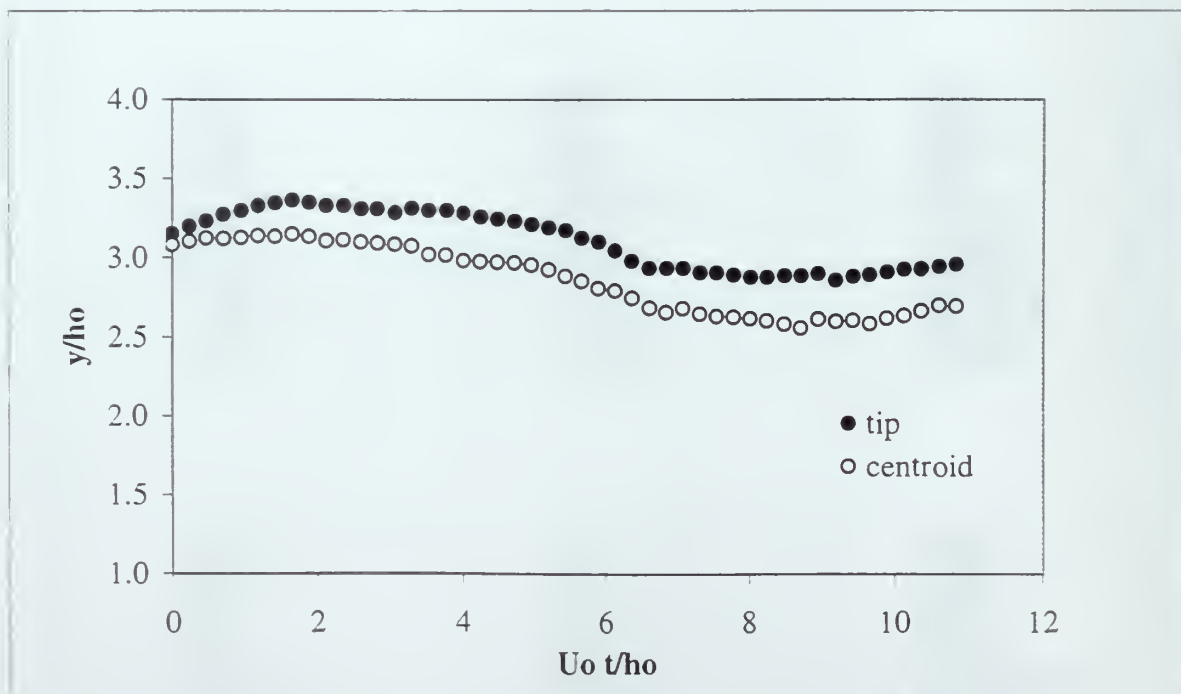


Figure 74b. Normalized y-component of position of the filament tip and centroid as a function of normalized time.

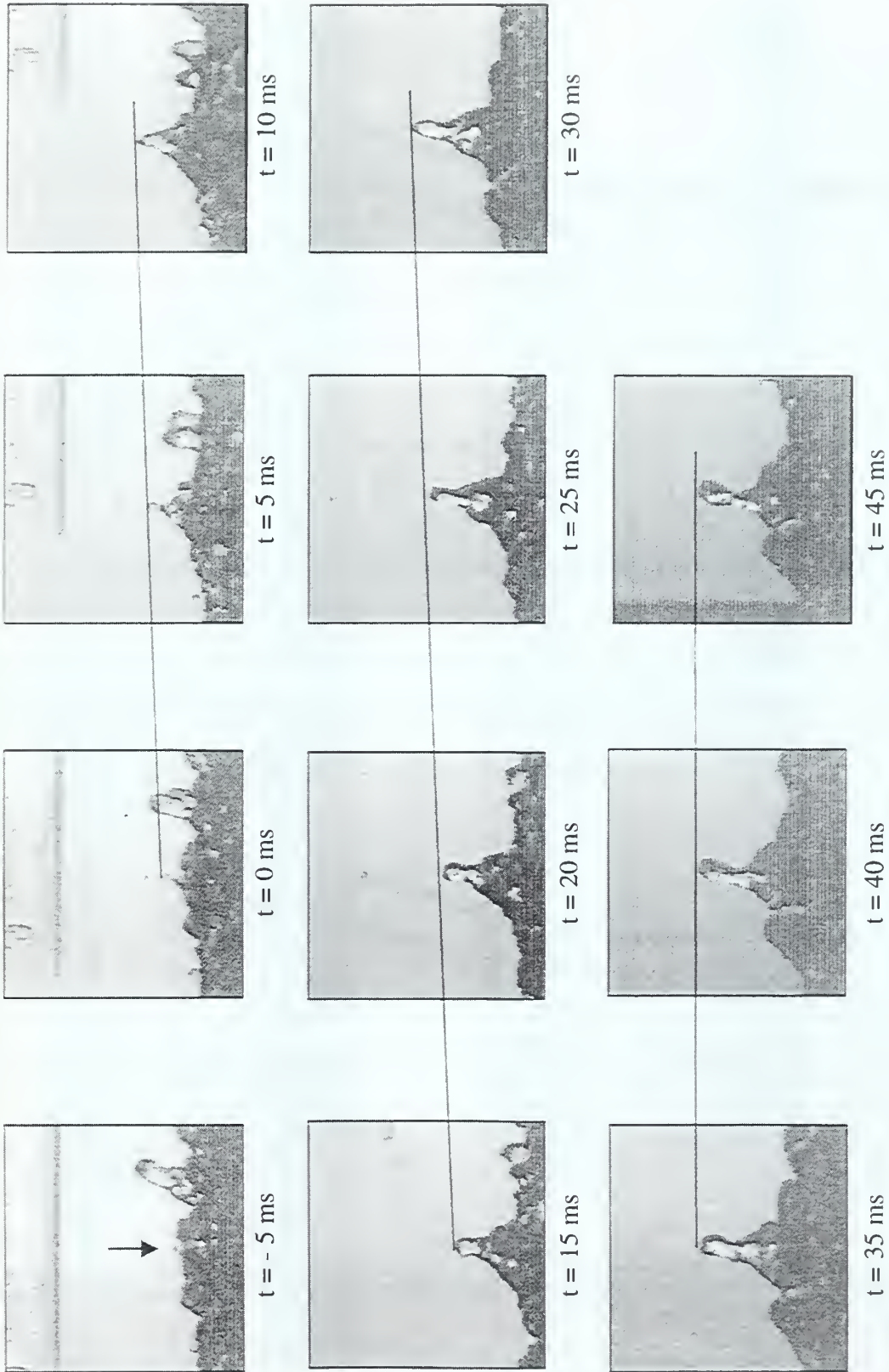


Figure 75. Sequence of images, capture for filament analysis (Case 4), where a ligament is born, immediately produces a droplet, continues to grow, and starts to neck.

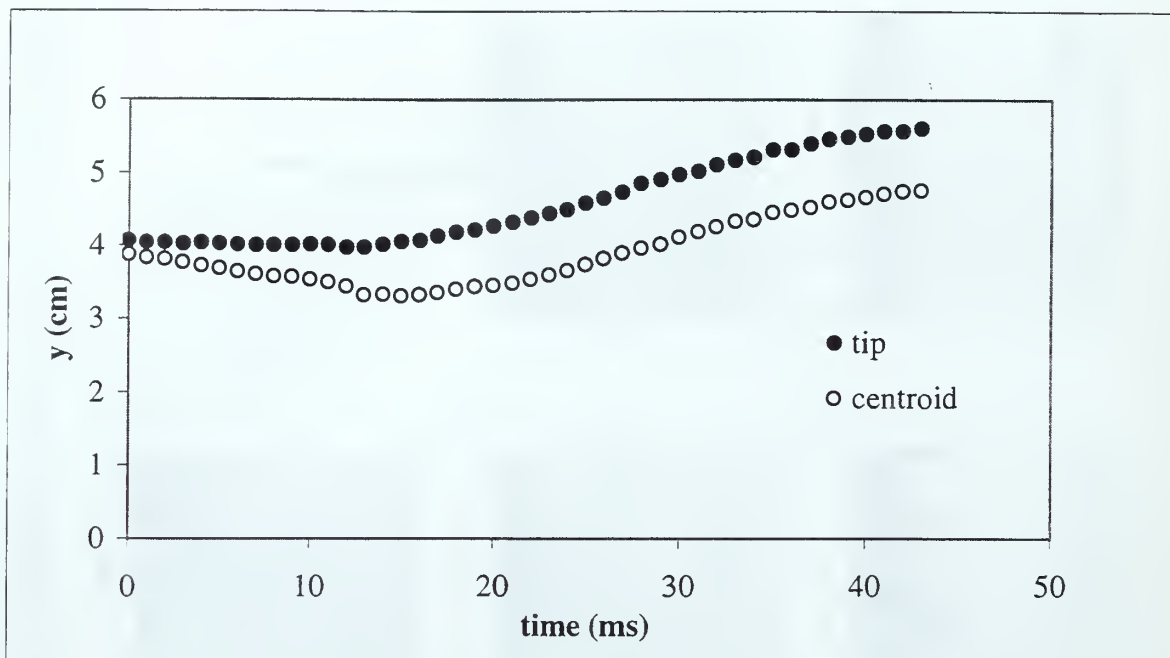


Figure 76a. Y-component of position of the filament tip and centroid as a function of time.

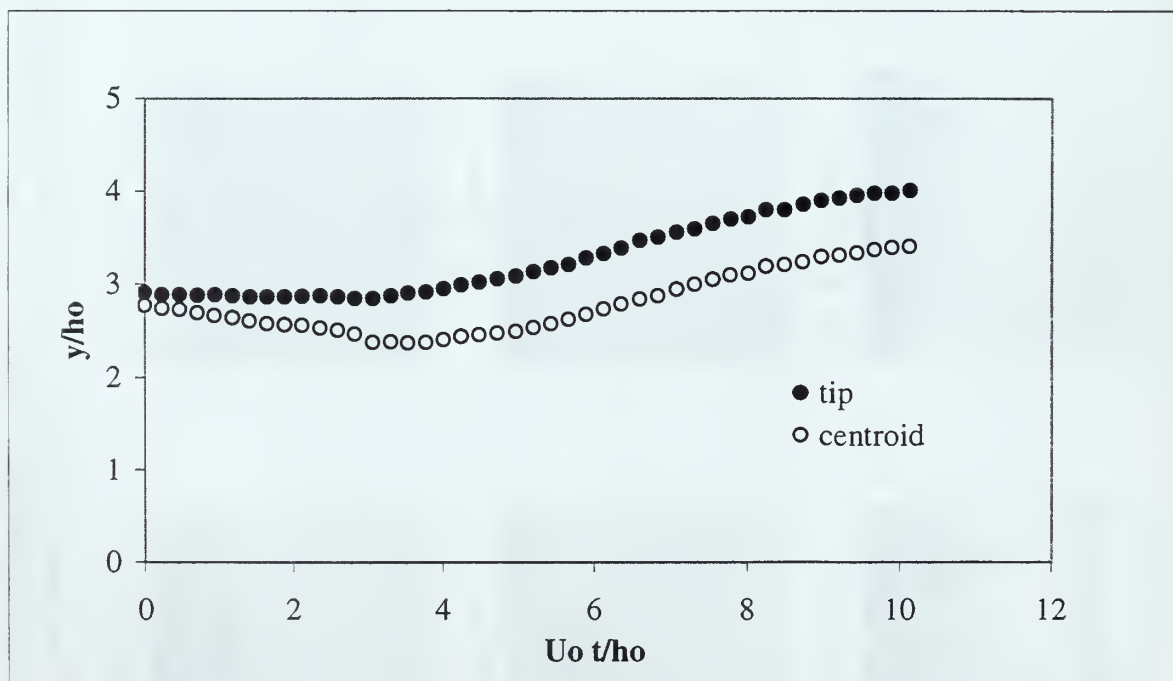


Figure 76b. Normalized y-component of acceleration of the filament tip and centroid as a function of normalized time.

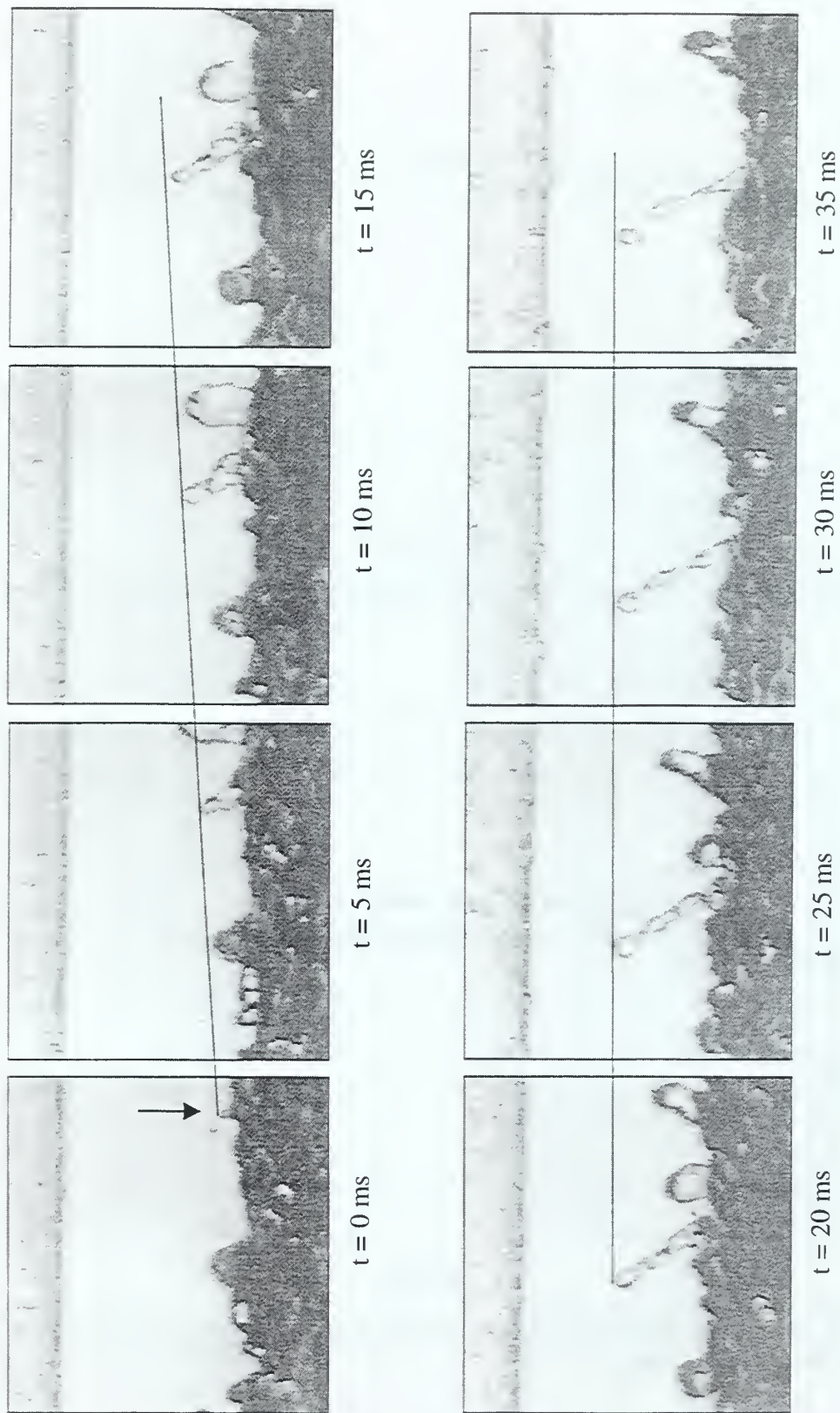


Figure 77. Sequence of images, captured for filament analysis (Case 5), where a ligament is born, leans forward, necks, and produces a droplet.



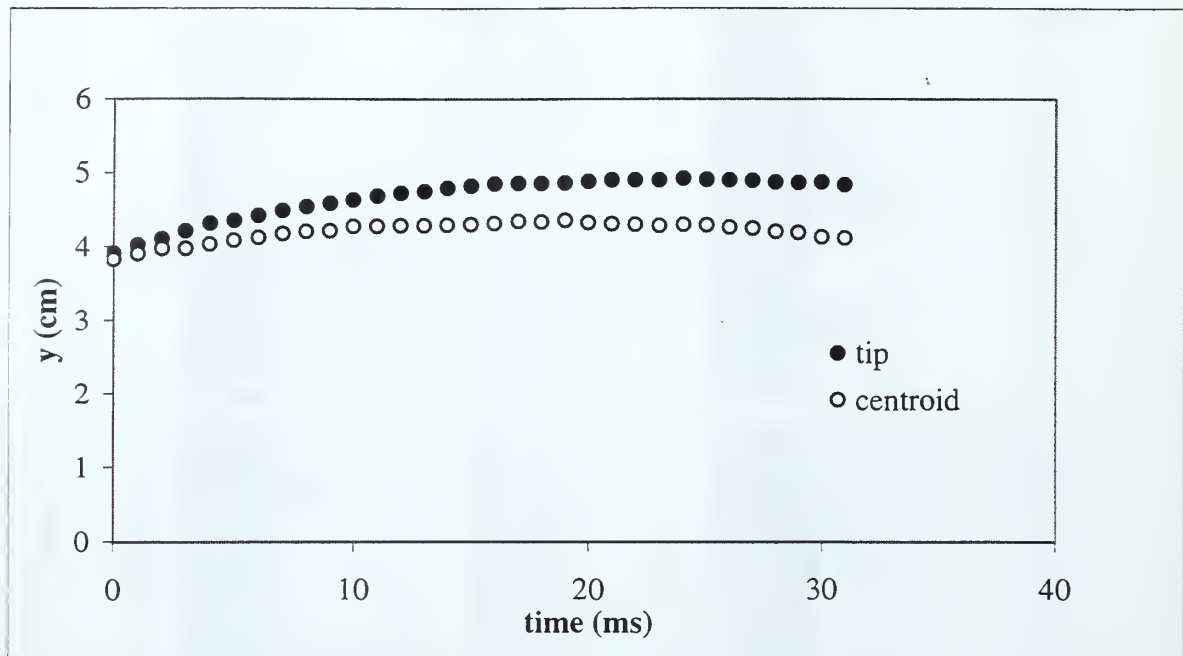


Figure 78a. Y-component of position of the filament tip and centroid as a function of time.

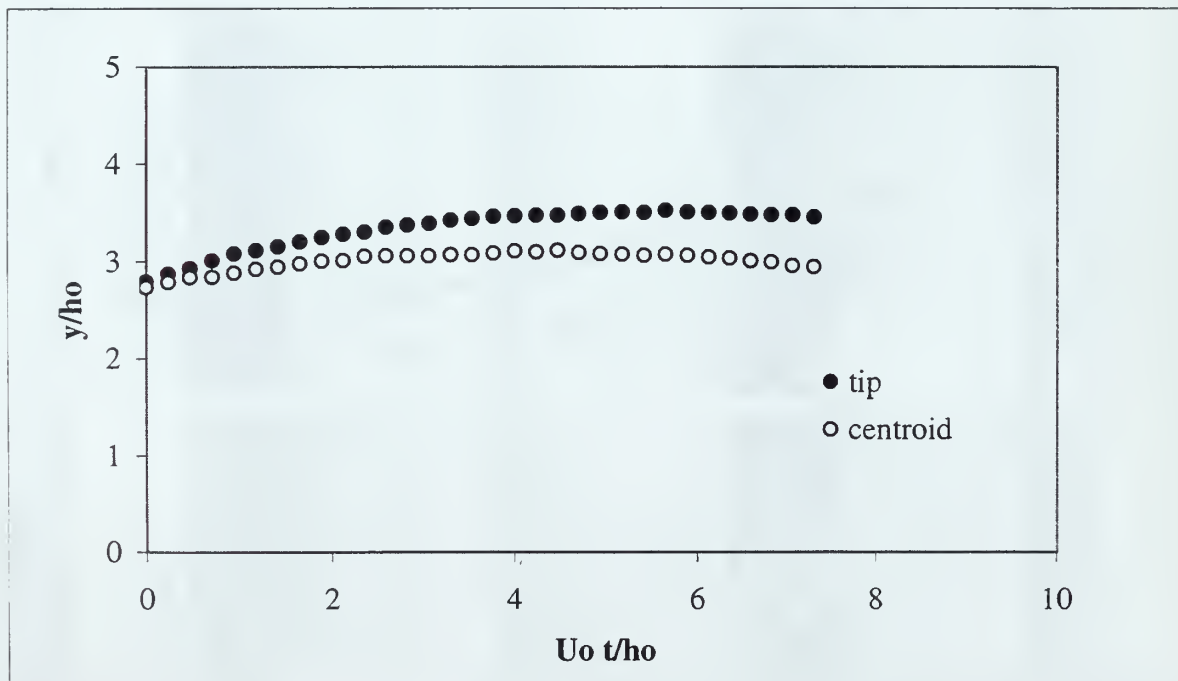


Figure 78b. Normalized y-component of position of the filament tip and centroid as a function of normalized time.

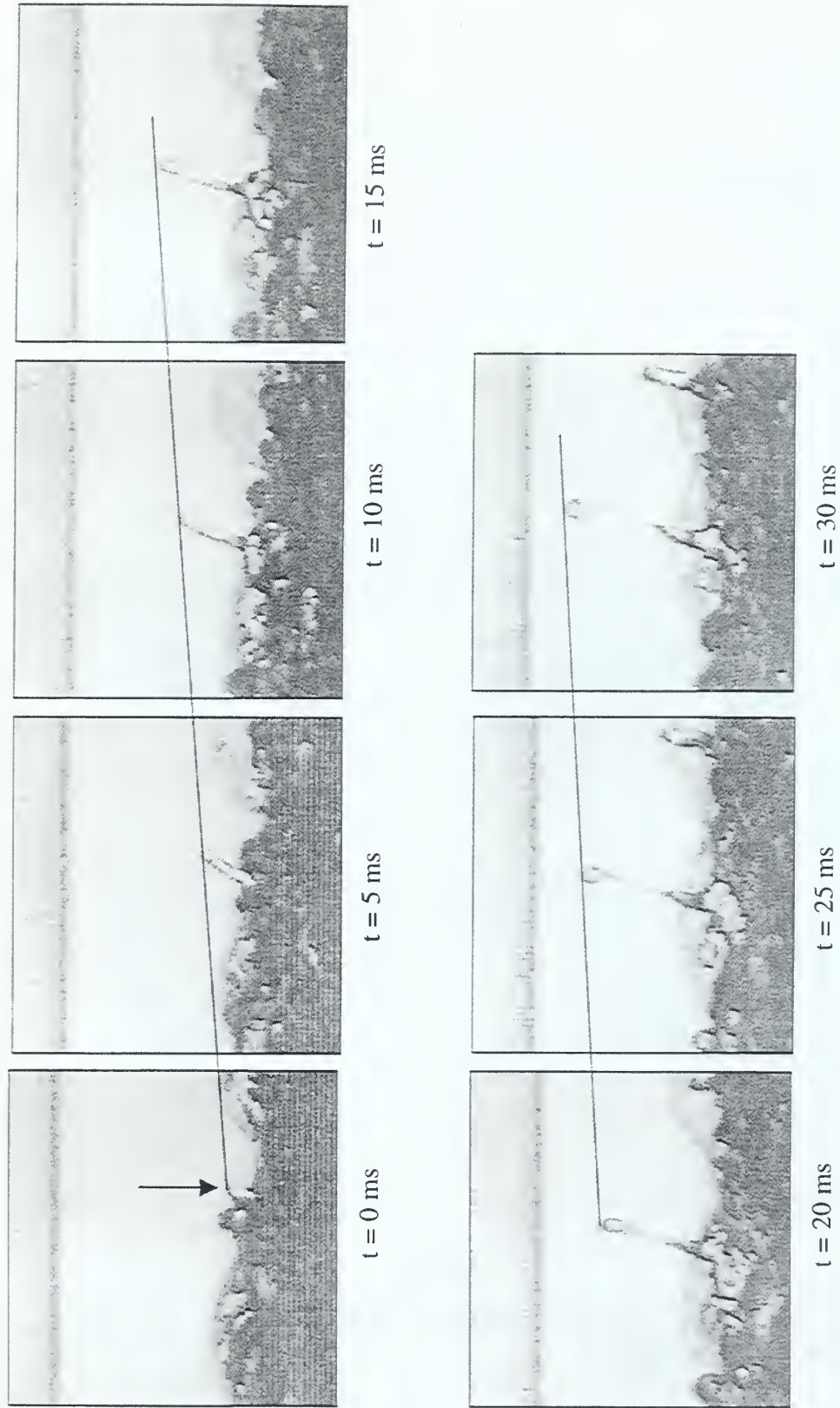


Figure 79. Sequence of images, captured for filament analysis (Case 6), where a ligament is born, leans backward, necks, and produces a droplet.



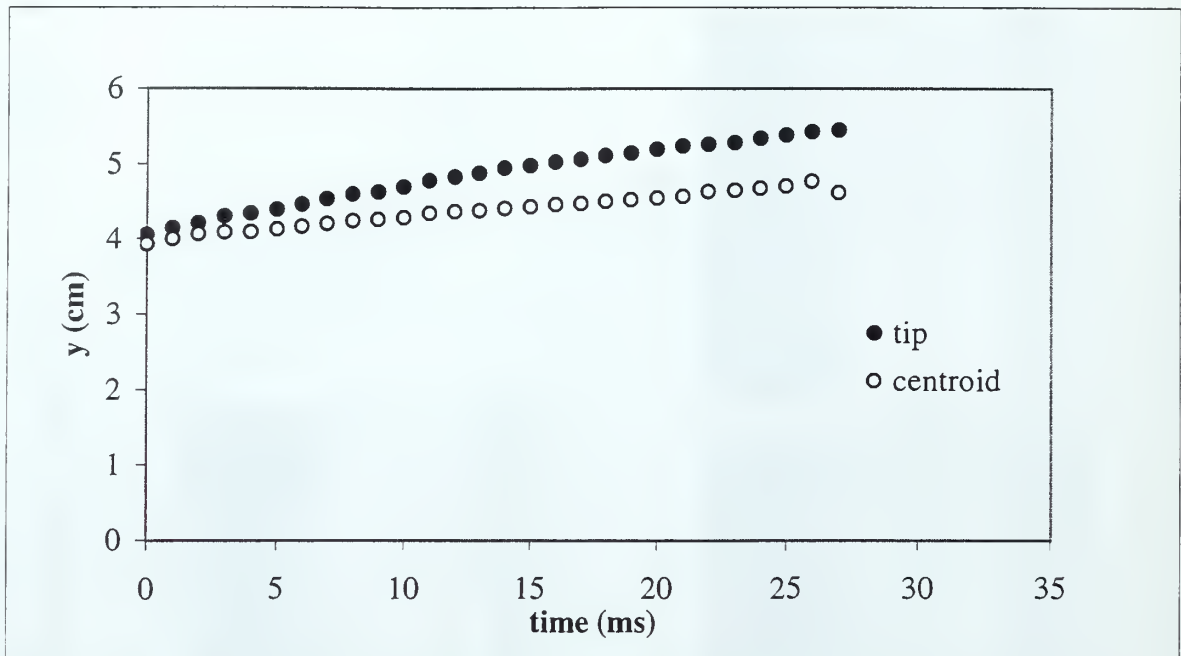


Figure 80a. Y-component of position of the filament tip and centroid as a function of time.

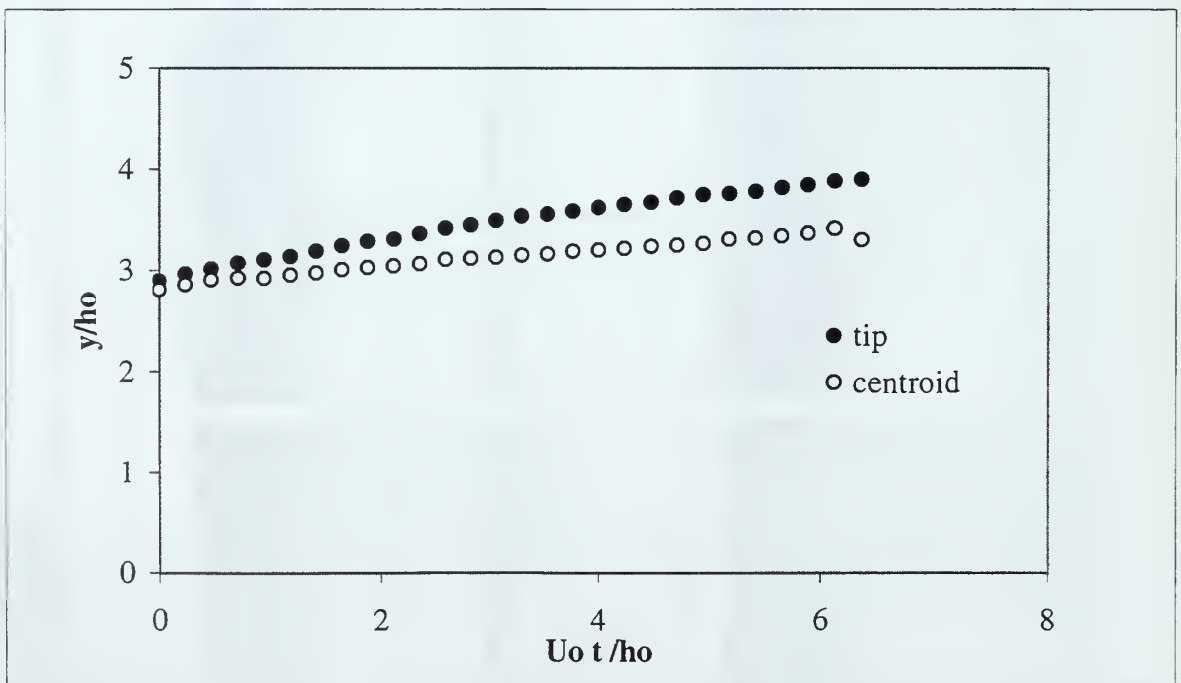
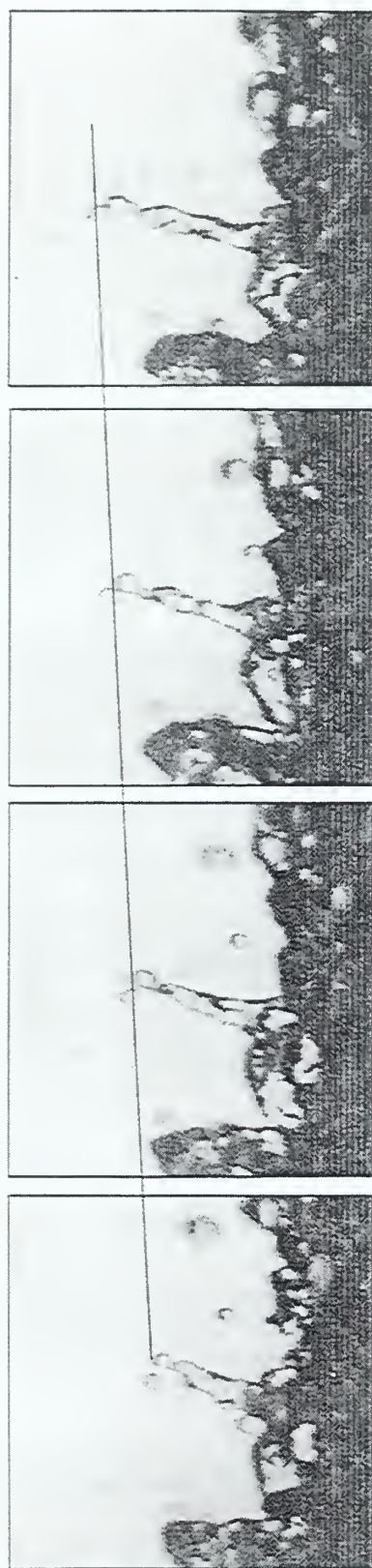
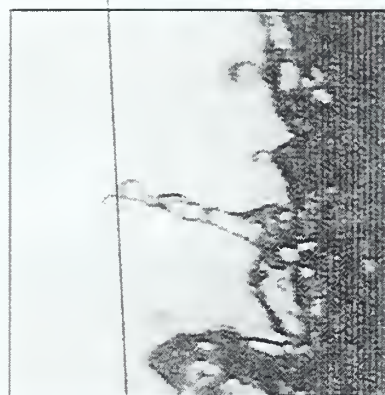


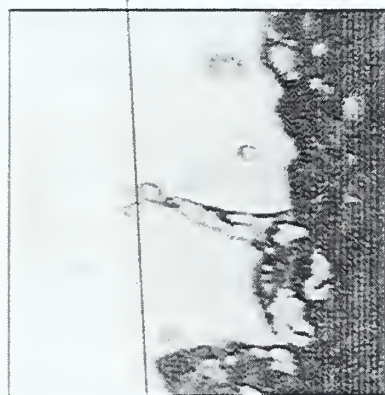
Figure 80b. Normalized y-component of position of the filament tip and centroid as a function of normalized time.



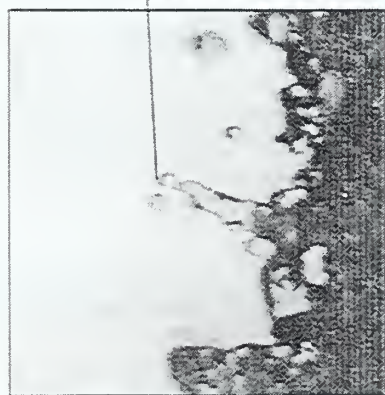
$t = 15$  ms



$t = 10$  ms



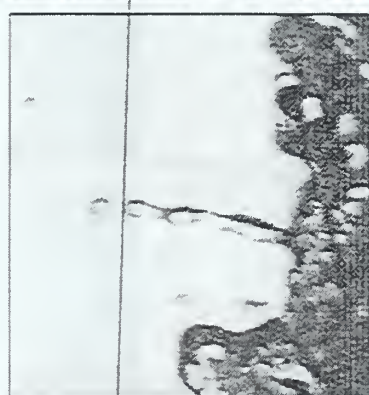
$t = 5$  ms



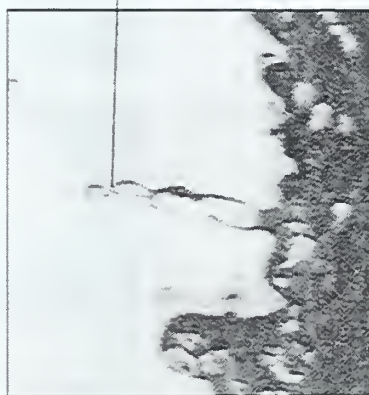
$t = 0$  ms



$t = 30$  ms



$t = 25$  ms



$t = 20$  ms

Figure 81. Sequence of images, captured for filament analysis (Case 7), where a ligament has developed, leans backward, starts to neck at various regions, and retracts.

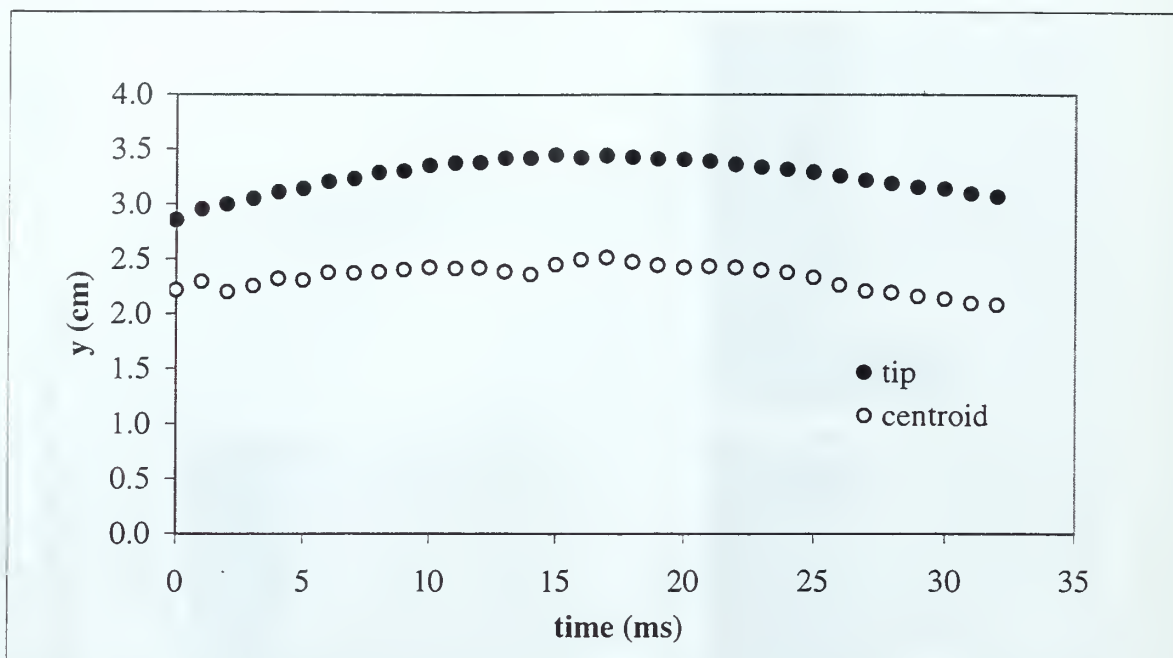


Figure 82a. Y-component of position of the filament tip and centroid as a function of time.

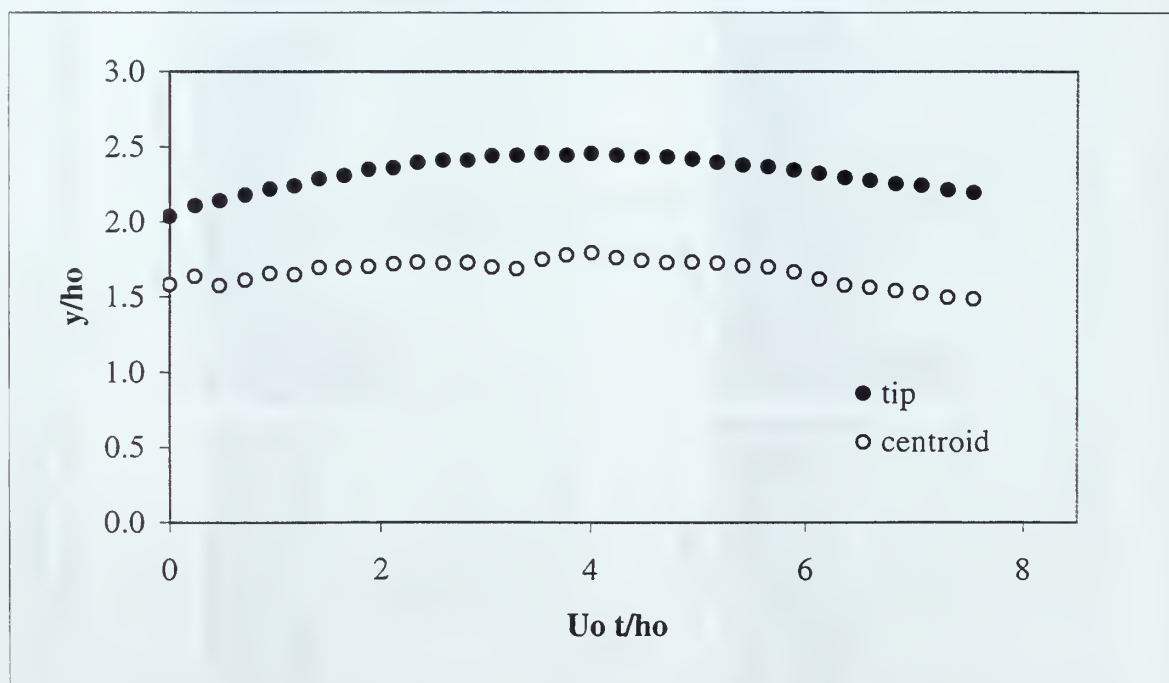


Figure 82b. Normalized y-component of position of the filament tip and centroid as a function of normalized time.



Figure 83. Sequence of images, captured for filament analysis (Case 8), where a ligament is born in between two other ligament necks and produces a droplet.

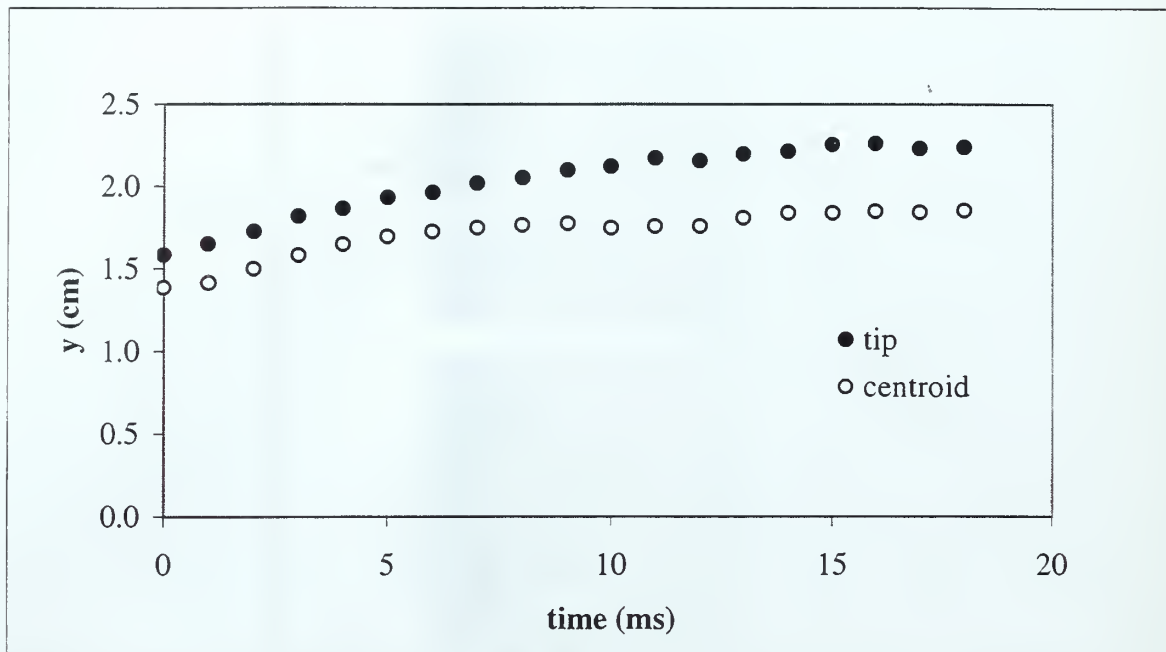


Figure 84a. Y-component of velocity of the filament tip and centroid as a function of time.

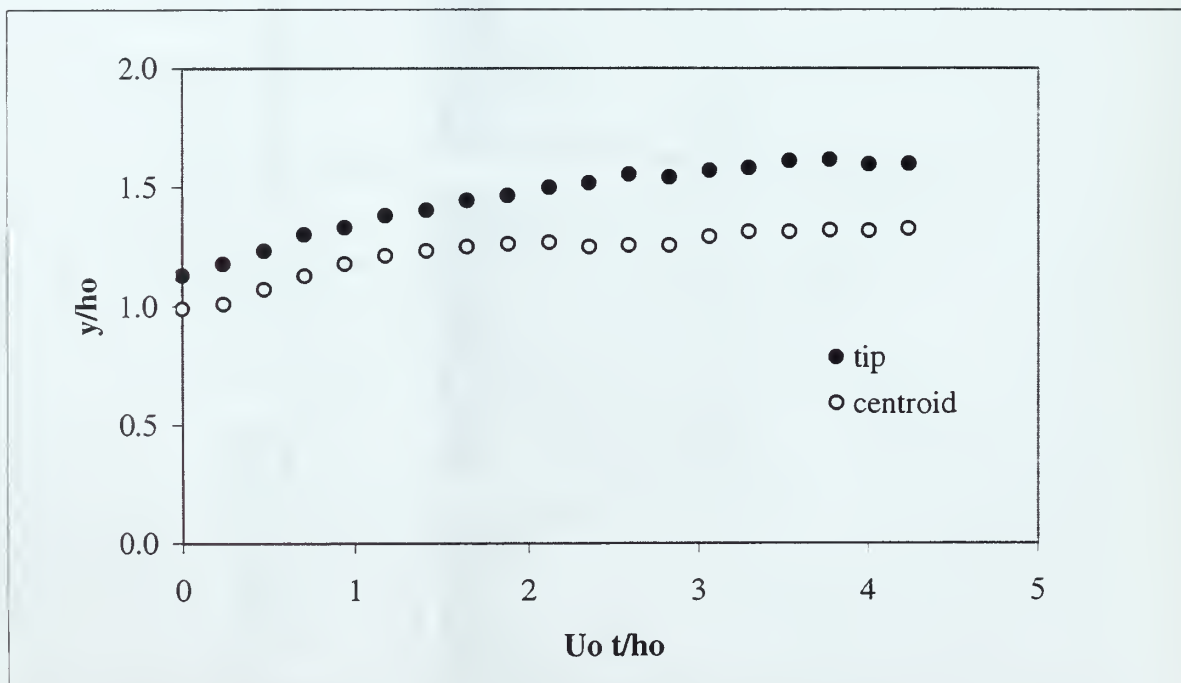


Figure 84b. Normalized y-component of position of the filament tip and centroid as a function of normalized time.



## REFERENCES

- Dia, Z., Chou, W-H., and Faeth, G.M. 1998. "Drop formation due to turbulent primary breakup at the free surface of plane liquid wall jets," *Physics of Fluids*, Vol. 10, pp. 1147-1157.
- Dombrowski, N. and Hooper, P. C. 1962. "The Effect of Ambient Density on Drop Formation in Sprays," *Chemical Engineering. Science.*, Vol. 17, pp. 291-305.
- Finley, P. J., Khoo, C. P. and Chin, J. P. 1966. "Velocity measurements in a thin turbulent water layer," *La Houille Blanche*, Vol. 21, pp. 713-721.
- Grass, A. J. 1971. "Structural features of turbulent flow over smooth and rough boundaries," *Journal of Fluid Mechanics*, Vol. 50, pp 233-255.
- Hoyt, J. W. and Taylor, J. J. 1977a. "Waves on water jets," *Journal of Fluid Mechanics*, Vol. 83, pp. 119-127.
- Hoyt, J. W. and Taylor, J. J. 1977b. "Turbulence Structure in a Water Jet Discharging in Air," *Physics of Fluids*, Vol. 20, Pt. II, No. 10, pp. S253-S257.
- Komori, S., Hiraga, Y., Murakami, Y. and Ueda, H. 1987. "The generation of surface-renewal eddies in an open channel flow," *Proceedings of the Second International Symposium on Transport Phenomena in Turbulent Flows*, Tokyo, pp. 75-85.
- Lin, S. P. and Reitz, R. D. 1998. "Drop and spray formation from a liquid jet," *Annual Review of Fluid Mechanics*, Vol. 30, pp. 85-105.
- Merrill, C. F. 1998. "Spray Generation from liquid wall jets over smooth and rough surfaces," Phd Dissertation, Mechanical Engineering Naval Postgraduate School, Monterey, CA.
- Ranz, W. E. 1958. "Some Experiments on Orifice Sprays," *Canadian Journal of Chemical Engineering*, Vol. 36, p. 175-181.
- Vaidyanathan, R., "Spray Generation from Free and Half-Free Jets", Master's Thesis, Naval Postgraduate School, Monterey, CA, March 1999.



THIS PAGE LEFT INTENTIONALLY BLANK

## INITIAL DISTRIBUTION LIST

1. Defense Technical Information Center ..... 2  
8725 John J. Kingman Rd., STE 0944  
Ft. Belvoir, VA 22060-6218
2. Dudley Knox Library ..... 2  
Naval Postgraduate School  
411 Dyer Rd.  
Monterey, CA 93943-5101
3. Department Chairman, Code ME..... 2  
Department of Mechanical Engineering  
Naval Postgraduate School  
Monterey, CA 93943-5000
4. Professor T. Sarpkaya, Code ME-SL ..... 4  
Department of Mechanical Engineering  
Naval Postgraduate School  
Monterey, CA 93943-5000
5. Curricular Officer, Code 34 ..... 1  
Naval Engineering Department  
Naval Postgraduate School  
Monterey, CA 93943-5000
6. Commanding Officer..... 2  
Supervisor of Shipbuilding, Conversion & Repair, USN  
PO Box 215  
Portsmouth, Virginia 23705-0215  
ATTN: LT Angel G Salinas
7. Dr Victor L Lechtenberg ..... 1  
Dean of Agriculture  
Purdue University  
1140 Agricultural  
Administration Building  
West Lafayette, IN 47907-1140
8. Professor Thomas N. Farris..... 1  
School of Aeronautics and Astronautics  
Purdue University  
1282 Grissom Hall  
West Lafayette, IN 47907-1282





63 290NPG 2522  
6/02 TH 22527-200 NIE













DUDLEY KNOX LIBRARY



3 2768 00405538 4